Circuits and Systems
Mekelweg 4,
2628 CD Delft
The Netherlands
http://ens.ewi.tudelft.nl/

CAS-2020-4893077

M.Sc. Thesis

Optimal Sensor Placement for Calibration-Involved Radio Astronomy Imaging Applications

Kaiwen Zhang

Abstract

In radio astronomy (RA), one of the key tasks is the estimation of the celestial source powers, i.e. imaging. To maximize the performance, it is crucial to optimize the receiver locations before the construction of a telescope array. However, although system calibration is an integral and crucial process of imaging, it has rarely been addressed for RA sensor placement problems previously. This motivates us to investigate whether incorporating calibration can result in better array designs. In this thesis, we focus on the calibration of the sensors' complex-scalar gains in particular, which are treated as nuisance parameters for the image estimation. The associated Cramer-Rao bound (CRB) is derived and employed as the design criterion. The nonlinear CRB-based sensor placement problem is cast as an NP-hard combinatorial optimization problem, and we adopt two approaches to solve such by approximation: (i) greedy algorithm and (ii) convex optimization with semidefinite relaxation. The former is chosen for simulations due to its good performance and lower computational complexity. Extensive simulations shows that compared to the calibration-excluded design, the proposed one only provides slight improvements to the imaging quality. However, the proposed array demonstrates the potential of accelerating the convergence of the gain estimation procedures. Through further investigation, we conclude that the lack of imaging quality improvident can be a consequence of the gain and image being near-orthogonal parameters.

Optimal Sensor Placement for Calibration-Involved Radio Astronomy Imaging Applications

Thesis

submitted in partial fulfillment of the
requirements for the degree of

Master of Science

in

Electrical Engineering

by

Kaiwen Zhang
born in Hefei, China

This work was performed in:

Circuits and Systems Group
Department of Microelectronics & Computer Engineering
Faculty of Electrical Engineering, Mathematics and Computer Science
Delft University of Technology

Delft University of Technology

Delft University of Technology
Department of
Microelectronics & Computer Engineering

The undersigned hereby certify that they have read and recommend to the Faculty of Electrical Engineering, Mathematics and Computer Science for acceptance a thesis entitled **"Optimal Sensor Placement for Calibration-Involved Radio Astronomy Imaging Applications"** by **Kaiwen Zhang** in partial fulfillment of the requirements for the degree of **Master of Science**.

Dated: 27th August 2020

Chairman: _____
prof.dr.ir. Geert Leus

Advisors: _____
prof.dr.ir. Geert Leus

_____
dr.ir. Stefan Wijnholds

Committee Members: _____
dr. Faruk Uysal

_____

Abstract

In radio astronomy (RA), one of the key tasks is the estimation of the celestial source powers, i.e. imaging. To maximize the performance, it is crucial to optimize the receiver locations before the construction of a telescope array. However, although system calibration is an integral and crucial process of imaging, it has rarely been addressed for RA sensor placement problems previously. This motivates us to investigate whether incorporating calibration can result in better array designs. In this thesis, we focus on the calibration of the sensors' complex-scalar gains in particular, which are treated as nuisance parameters for the image estimation. The associated Cramer-Rao bound (CRB) is derived and employed as the design criterion. The nonlinear CRB-based sensor placement problem is cast as an NP-hard combinatorial optimization problem, and we adopt two approaches to solve such by approximation: (i) greedy algorithm and (ii) convex optimization with semidefinite relaxation. The former is chosen for simulations due to its good performance and lower computational complexity. Extensive simulations shows that compared to the calibration-excluded design, the proposed one only provides slight improvements to the imaging quality. However, the proposed array demonstrates the potential of accelerating the convergence of the gain estimation procedures. Through further investigation, we conclude that the lack of imaging quality improvident can be a consequence of the gain and image being near-orthogonal parameters.

Acknowledgments

I would like to take the chance to express my sincere gratitude to all the people who have helped and supported me during this work.

First, I would like to thank my supervisor, Geert, for his time and efforts spent on guiding me throughout the thesis. He was always available to me, even during the most chaotic periods of this year. His feedback was detailed and constructive. Every conversation with him has led to new findings and insights for the work. Indeed, not all research efforts can always end up with exciting outcomes, but Geert has constantly encouraged me throughout the past months. The extraordinary support and advice I received from him were not only confined to the research, but also extended to other aspects of my life, including making choices related to my future career. So here, I would like to express my appreciation to him once again.

Second, I would like to thank Stefan, my secondary thesis advisor. Last November, he kindly gave me a very nice tour of ASTRON and that has provided me great insights into the research theme. Although being distant from Delft, he has been making every single effort to give me timely feedback and detailed suggestions for my research. His rich experience in radio astronomy was critical for this project, and the thesis could not have been made possible without his valuable inputs.

I also would like to thank Dr. Faruk Uysal for being one of my committee members and allowing me to fit my defense in such a tight schedule. The advice and comments he provided were very helpful.

It has been a great experience to work in the CAS group, so a big thank you to all of the members! In particular, I would like to mention two people - Mario and Tarik - who have been exceptionally kind. They have assisted me on various issues and shared their experience to help me make important decisions in life.

Last but not the least, I would like to thank my parents for their immense and unconditional love. They have always encouraged and supported me no matter what the circumstance is. Without them, I could never become who I am today.

Kaiwen Zhang
Delft, The Netherlands
27th August 2020

Contents

List of Figures

List of Tables

Nomenclature

Basics

x	Scalar
$\mathbf{x}$	Vector
$\mathbf{X}$	Matrix
$\mathbf{X}_{i,j}$	The (i, j)-th element of a matrix
$\mathbf{X}_{i,:}$	The i-th row of a matrix
$\mathbf{X}_{:,j}$	The j-th column of a matrix
$\mathcal{X}$	Set

Linear Algebra

$\mathbf{I}$	Identity matrix
$\mathbf{1}$	All-ones vector
$\mathbf{0}$	All-zeros vector
$\mathbf{O}$	All-zeros Matrix
$\otimes$	Kronecker product
$\circ$	Khatri-Rao product (element-wise Kronecker product)
$\odot$	Hadamard product
$(\cdot)^{-1}$	Matrix inverse
$(\cdot)^{T}$	Matrix transpose
$(\cdot)^{H}$	Matrix Hermitian
$(\cdot)^{\dagger}$	Moore-Penrose pseudoinverse
$\mathrm{diag}(\mathbf{x})$	Stretching the vector $\mathbf{x}$ to form a diagonal matrix
$\mathrm{vec}(\cdot)$	Vectorization of a matrix
$\mathrm{tr}(\cdot)$	Trace of a matrix
$\det(\cdot)$	Determinant
$\|\cdot\|_1$	l_1-norm
$\|\cdot\|_2$	l_2-norm
$\|\cdot\|_F$	Frobenius norm

Other Symbols

$\circledast$	Convolution
$\overline{(\cdot)}$	Convex conjugate
$\mathbb{E}[\cdot]$	Expectation

1 Background

1.1 Introduction to radio interferometry

During the recent century, the advancement in radio astronomy (RA) has greatly extended our knowledge of the universe. Starting from Jansky in the 1930s [3], radio telescopes have enabled the scientific community to explore the universe beyond the visible spectrum. As single telescopes are limited by their apertures, the concept of interferometry [4] was proposed, which allows a group of smaller receiver elements to combine their data, leading to an array of telescopes with a much larger synthesized aperture.

One of the key tasks in RA is imaging. The purpose of imaging is to infer the astronomical source powers, or the brightness, from the noisy data received at each receiver. The sources on different directions of arrival (DOAs) in the sky emit signals arriving at the receivers with different geometric delays, which is exploited by radio interferometers to achieve directional selectivity. This is done by correlating the received signals. The correlation, in statistical expectation, is essentially a Fourier transform of the image, thus the basic imaging problem can be regarded as retrieving the source powers from its Fourier transformed data. [1]

In reality, such a process also requires the accurate knowledge of the system conditions, which is often not known to the interferometer and has to be jointly estimated along with the celestial source powers, the image. Examples of such conditions are the thermal noise levels, the gain response of the receiver elements, and the disturbance due to the signal propagation through the ionosphere layer [1]. Apart from some experimental trials of using artificial test sources, e.g. [5] [6] [7], the state-of-the art calibration methods usually regard the celestial sources themselves as the calibrators, whose power is exactly the parameter-of-interest. Therefore, standard RA imaging pipelines often involve iterative schemes to achieve the joint acquisition of the image and the calibration parameters.

A simplified iterative imaging scheme is shown in figure 1.1 (see e.g. Figure 13 of [1] for the detailed structure). The process is started by the initial calibration process, which provides an estimation of some critical system conditions based on an assumed initial sky model. After that, the system executes source extraction and self-calibration iteratively. New astronomical sources are identified, subtracted from the residual image and added to the existing sky model which is then used to update the calibration parameters. The refined calibration parameters, in turn, assist the imaging algorithm to detect more new sources. This is referred to as the major cycle. Such a loop is executed until the system converges and the residual image becomes noise-like.

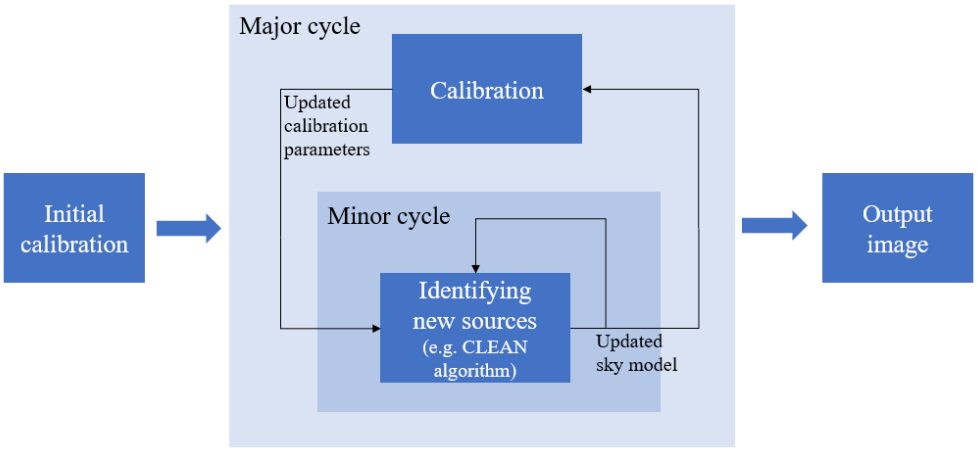

Figure 1.1: An illustration of the bacis structure of the radio astronomy imaging pipeline (the image is a simplified version of Figure 13 in [1]).

As the major cycle is computationally expensive to run, the practical solution is to identify a large number of sources rather than a single one after the calibration parameters are updated. This is usually regarded as the minor cycle of imaging [1].

1.2 Radio astronomy station calibration

As mentioned, in the ideal case, the interferometer only needs to take the geometric phase delay into consideration. In reality, a number of additional system dynamics also play their roles, which have to be estimated and compensated during the station calibration: [8]

(1) the complex gain per signal path

(2) the system noise power

(3) the beam pattern per receiver

(4) the position and orientation of each receiver

While the electronic gain and system noise is required to be estimated with the image, the rest can be treated as known. The receiver element beam pattern can be accurately obtained via electro-magnetic modeling in lab conditions [1]. And it is shown that the position and orientation of the receivers should better be directly measured in the field, as practical testing in the field can achieve much higher precision than estimation from the received data [8]. Therefore, in this project, we only consider the calibration of effect (1) and (2).

The fluctuation of the complex gain is caused by two types of effects and they can be modelled separately: [1]

1. **Instrumental effects,** which results in a direction-dependent response and a direction-independent complex gain per receiver element. Since we assume the direction-dependent response can be measured in lab conditions, it is assumed to be factored into the sources themselves.

2. **Propagation effects**, which are caused by ionospheric and tropospheric irregularity. This results in shifts of apparent source locations.

In particular, the propagation effect acts differently on the radio interferometer depending on the system architecture, which can be grouped into four distinct categories (figure 1.2) [2]. These four cases differ in the relative size of the field-of-view (FOV) and/or the relative length of the maximum baseline, compared to the scale of the ionospheric irregularity. The project is confined to study the first case, i.e. small FOV and short aperture, but can be easily extended to the third category.

Therefore, in this project, we only consider the direction-independent scalar complex gain for effect (1).

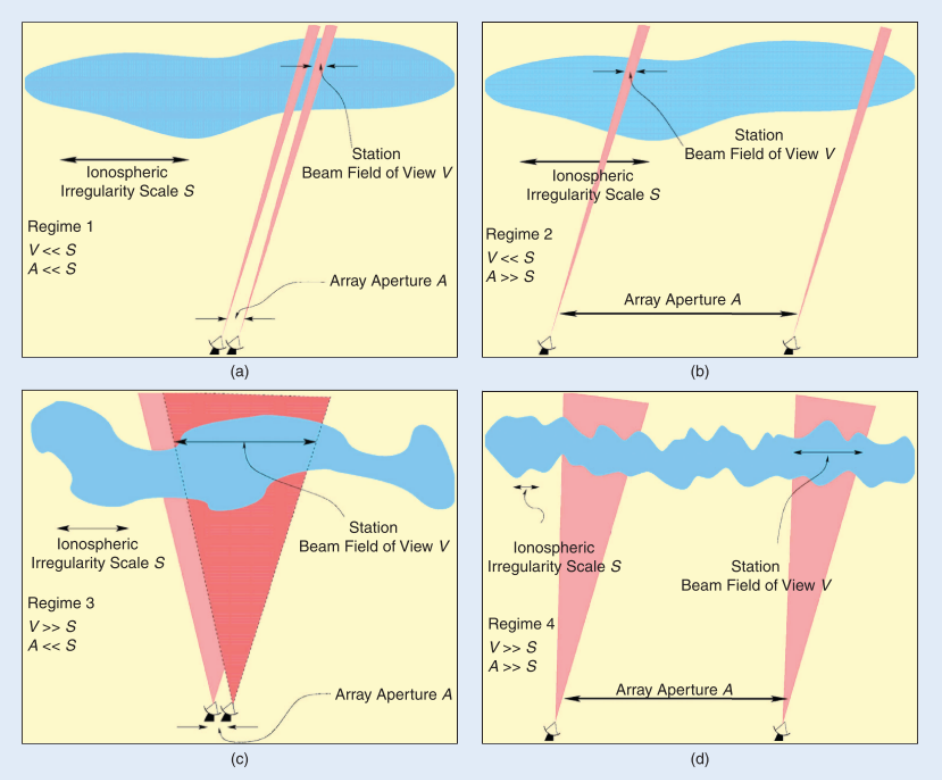

Figure 1.2: Station calibration scenarios. Image is taken from [2].

1.3 Data model

For radio interferometry, the signals emitted by the celestial sources, which usually spread across a wide frequency range, are delayed and physically summed together at the receiving antennas. To process such a wide-band data, the analog signals are divided into multiple narrow sub-bands so that a time delay of a sub-band signal can be approximated by a phase shift of its complex envelope (i.e. narrowband condition) [1]. To be explicit, suppose that for the k-th narrow sub-band centered at frequency f_k, there is a bandpass signal

$$\tilde{s}(t,k) = s(t,k)\, e^{\mathrm{j}2\pi f_k t} \tag{1.1}$$

which is continuous on time t. If such a signal is delayed by τ, i.e $\tilde{s}_\tau(t,k) = \tilde{s}(t-\tau,k)$, its complex envelope $s_\tau(t,k)$ can be approximated by

$$s_\tau(t,k) \approx s(t,k)\, e^{-\mathrm{j}2\pi f_k \tau}. \tag{1.2}$$

Since the astronomical sources are far away, the emitted electromagnetic waves can be assumed as plane waves when they impinge on the array. As such, the phase shift caused by the geometric time delay $\tau(t,k)$ is only dependent on the inner product of the source and receiver locations, i.e.

$$a_{j,q}(t,k) = e^{-\mathrm{j}2\pi f_k \tau(t,k)} = e^{-\mathrm{j}\frac{2\pi f_k}{c}\mathbf{z}_j^T \mathbf{l}_q(t)} \tag{1.3}$$

where c is the wave speed, and $\mathbf{z}_j$ and $\mathbf{l}_q(t)$ are the coordinates of the j-th antenna and the q-th source. The source locations vary over time due to the earth rotation. Assuming there are M receivers and N celestial sources, by stacking all the phase delays, we obtain the array response matrix [1]

$$\mathbf{A}(t,k) = \begin{bmatrix} a_{1,1}(t,k) & a_{1,2}(t,k) & \cdots & a_{1,N}(t,k) \\ a_{2,1}(t,k) & a_{2,2}(t,k) & \cdots & a_{1,N}(t,k) \\ \vdots & \vdots & \ddots & \vdots \\ a_{M,1}(t,k) & a_{M,2}(t,k) & \cdots & a_{M,N}(t,k) \end{bmatrix}. \tag{1.4}$$

In this project, we only consider one narrow frequency band, therefore the frequency index k is omitted for brevity. The basic data model is then given by [1],

$$\mathbf{x}(t) = \mathbf{G}(t)\, \mathbf{A}(t)\, \mathbf{s}(t) + \mathbf{n}(t), \tag{1.5}$$

where

- $\mathbf{s}(t) = [s_1(t), ..., s_N(t)]^T$ stacks all the source signals
- $\mathbf{n}(t) = [n_1(t), ..., n_N(t)]^T$ stacks all the noises
- $\mathbf{x}(t) = [x_1(t), ..., x_M(t)]^T$ is the received array data vector
- $\mathbf{G}(t) = \mathrm{diag}(\mathbf{g})$ and $\mathbf{g} = [g_1(t), ..., g_M(t)]^T$ represents the direction-independent complex gains.

For simplicity, first we only consider one time instance, hence the time index t can also be dropped for the following analysis. Assuming the source signals and noise are both *spatially* white Gaussian processes, the data covariance can be computed as

$$\begin{aligned}\mathbf{R} &= \mathbb{E}[\mathbf{x}\mathbf{x}^H] \\ &= \mathbf{G}\mathbf{A}\boldsymbol{\Sigma}_s\mathbf{A}^H\mathbf{G}^H + \boldsymbol{\Sigma}_n. \end{aligned} \tag{1.6}$$

where $\boldsymbol{\Sigma}_s = \text{diag}(\boldsymbol{\sigma}_s)$ and $\boldsymbol{\Sigma}_n = \text{diag}(\boldsymbol{\sigma}_n)$ are the signal and noise covariance matrices. Vectorization through the property [1, (4)] gives a covariance data model that is linear in $\boldsymbol{\sigma}_s$,

$$\begin{aligned}\mathbf{r} &= \text{vec}(\mathbf{R}) \\ &= (\overline{\mathbf{G}\mathbf{A}} \circ \mathbf{G}\mathbf{A})\,\boldsymbol{\sigma}_s + (\mathbf{I} \circ \mathbf{I})\,\boldsymbol{\sigma}_n. \end{aligned} \tag{1.7}$$

In reality, the expectation in (1.6) is approximated by averaging sample covariances over short periods of time, which are referred to as the short-term integration (STI) intervals. The short time period ensures that the system dynamics such as gains and signal powers remain stationary, and the effects of the earth rotation is negligible.

In this project, we only consider a single STI period, whereas the complete model involving multiple STI periods can be found in [8]. Suppose within one STI interval, there are P samples of the received data $\mathbf{X} = [\mathbf{x}(1), \mathbf{x}(2), ..., \mathbf{x}(P)]$. The sample covariance is then given as

$$\hat{\mathbf{R}} = \frac{1}{P}\mathbf{X}\mathbf{X}^H. \tag{1.8}$$

This would introduce an additional error term $\mathbf{e}$ in the covariance data model,

$$\hat{\mathbf{r}} = \mathbf{r} + \mathbf{e} \tag{1.9}$$

which follows a Wishart distribution. The covariance of $\mathbf{e}$ can be calculated as [8]

$$\boldsymbol{\Sigma} = P\,\overline{\left(\frac{1}{P}\mathbf{R}\right)} \otimes \left(\frac{1}{P}\mathbf{R}\right) \tag{1.10}$$

$$= \frac{1}{P}\,\overline{\mathbf{R}} \otimes \mathbf{R}. \tag{1.11}$$

1.4 Problem statement

In the recent decades, radio telescope arrays tend to have much larger sizes, with significantly increased numbers of receiver elements as well as unprecedented spatial spreads. Such a rapid change is due to several reasons. First, this helps to increase the resolution and sensitivity of the interferometer [4]. Second, recent interest from the RA community in the low-frequency domain requires a telescope array with an effective collecting area of around one square kilometer [9], which has become a driving force for a series of current and future large-scale implementations such as LOFAR [10], LWA [11] and SKA [12]. This of course makes the calibration and imaging much more challenging. But before that, a more fundamental question is how to distribute such a large amount of receivers in an optimal way, which is essentially the motivation of this thesis work.

Based on the introduced data model, we regard the astronomical imaging as an estimation process which aims to retrieve the signal powers of the celestial sources from the covariance data $\hat{\mathbf{r}}$ corrupted by the Wishart noise $\mathbf{e}$. The model involves a number of estimation parameters:

$\boldsymbol{\gamma}$	magnitudes of $\mathbf{g}$
$\boldsymbol{\phi}$	phases of $\mathbf{g}$
$\boldsymbol{\sigma}_s$	imaging source powers
$\boldsymbol{\sigma}_n$	imaging noise powers
$\boldsymbol{\sigma}'_s$	calibration source powers
$\boldsymbol{\sigma}'_n$	calibration noise powers

among which the parameter-of-interest is $\boldsymbol{\sigma}_s$, whereas the rest are nuisance parameters. $\boldsymbol{\sigma}'_s$ and $\boldsymbol{\sigma}'_n$ are the parameters associated with the calibration observations which are related through a data model that is the same to (1.7) and (1.9) but is specifically constructed for the calibration sources. We will come back to this in later chapters. The estimation parameters are stacked to form a vector $\boldsymbol{\theta} = [\boldsymbol{\gamma}^T, \boldsymbol{\phi}^T, \boldsymbol{\sigma}_s^T, \boldsymbol{\sigma}_n^T, \boldsymbol{\sigma}_s'^T, \boldsymbol{\sigma}_n'^T]^T$.

The problem of sensor location optimization can be formulated as finding the optimal set of sensor coordinates $\mathcal{Z}$ such that the imaging performance is maximized, while keeping the number of sensors below a certain budget K, i.e.

$$\begin{aligned} \max_{\mathcal{Z}} \quad & \text{image quality} \\ \text{s.t.} \quad & \text{number of sensors} \leq K \end{aligned} \tag{1.12}$$

The quality of the image is strongly related to the actual imaging algorithms being used. There exist multiple efficient algorithms, for instance, the CLEAN algorithm [13] and the weighted least squares (WLS) algorithm [14]. However, the positions of the receiver elements are usually fixed once upon construction, thus it is inappropriate to optimize the sensor placement for a particular algorithm while completely ignoring the others. Moreover, the array design must accommodate potential future improvements of the imaging algorithm in the extent of system lifetime.

For such a consideration, we propose to use the CRB of the estimation problem as the optimization objective, since being a lower bound it reflects the best achievable performance of an unbiased estimator.

1.5 Thesis outline

The remainder of the thesis is structured as follows:

- **Chapter 2**: We derive the CRB for the introduced imaging problem and provide some identifiability analyses for the model.
- **Chapter 3**: We formulate a combinatorial scheme which transforms the CRB-based continuous sensor placement problem into an NP-hard discrete sensor selection problem. We further adopt two approaches to solve such a problem in approximation.
- **Chapter 4**: We introduce three RA imaging scenarios and subsequently perform sensor selection tests for each one of them. This mainly intends to compare the two employed optimization methods.
- **Chapter 5**: We conduct simulations to assess the statistical (i.e. asymptotic) and general performances of the selected arrays. We also assess their respective gain estimation convergence speeds. We observe that incorporating gain calibration in sensor selection does not provide promising improvement in imaging quality, but is able to accelerate the iterative gain calibration.
- **Chapter 6**: We provide further analysis to explain the lack of improvement in terms of the imaging quality.
- **Chapter 7**: We conclude the thesis and summarize the key findings. Directions for possible future works are also suggested.

Cramér–Rao Bound

2

In this chapter, we derive the CRB for the considered RA image estimation process. Section 2.1 introduces the closed-form FIM (i.e. the Bangs' formula) that works generally for parameter estimations under Gaussian covariance models. Section 2.2 provides the Jacobian matrices associated with the parameter vector $\boldsymbol{\theta}$ so that we can configure the Bangs' formula specifically for the considered estimation task. Section 2.3 explains how nuisance parameters can be dealt with so that the derived CRB only describes the imaging error instead of the error for all the parameters in $\boldsymbol{\theta}$.

2.1 Basic theory

For multiple parameter estimation, the CRB matrix defines the lower bound of the expected output covariance from an unbiased estimator. The CRB can be calculated by

$$\mathbf{C} = \mathbf{F}^{-1} \tag{2.1}$$

where $\mathbf{F}$ is the Fisher information matrix (FIM) [15].

For the covariance model (1.7), the input data $\mathbf{x}$ is zero-mean Gaussian, so the covariance data $\mathbf{r}$ is corrupted by a Wishart distributed noise $\mathbf{e}$ as previously mentioned. In this particular case, a closed-form expression has already been derived in previous works, which is referred to as the Bangs' formula [16]

$$\mathbf{F} = P\,\mathbf{J}^H\,(\overline{\mathbf{R}}^{-1} \otimes \mathbf{R}^{-1})\,\mathbf{J} \tag{2.2}$$

$$= P\,\mathbf{J}^H\,\boldsymbol{\Sigma}^{-1}\,\mathbf{J} \tag{2.3}$$

where the Wishart covariance $\boldsymbol{\Sigma} = \overline{\mathbf{R}} \otimes \mathbf{R}$ and the Jacobian matrix $\mathbf{J}$ is obtained by evaluating the gradient of the covariance data $\mathbf{r}$ w.r.t. $\boldsymbol{\theta}^T$, that is

$$\mathbf{J} = \frac{\partial\,\mathbf{r}(\boldsymbol{\theta})}{\partial\,\boldsymbol{\theta}^T}. \tag{2.4}$$

Since the number of samples P only leads to a scaling of the CRB, setting it to any positive integer value will result in the same array design based upon it. For simplicity we fix P to 1 during the sensor selection process (which will be introduced in later chapters), whereas for computing the performance in simulations P is set to other desired values.

2.2 Jacobians

Up to this point, the estimation problem aims to retrieve the full parameter vector $\boldsymbol{\theta}$. However, it will be shown that there exist system ambiguities in the model, as a result some variables are not simultaneously identifiable: [17]

1. **The magnitude ambiguity**
   $\boldsymbol{\gamma}$ and $\boldsymbol{\sigma}_s$ cannot be jointly estimated since an arbitrary factor can be extracted from one and being multiplied with the other. To resolve this magnitude ambiguity, whenever $\boldsymbol{\gamma}$ and $\boldsymbol{\sigma}_s$ are both present in the parameter vector $\boldsymbol{\theta}$, we normalize the first receiver's gain magnitude to unity, i.e. $\gamma_1 = 1$. The same treatment is done when $\boldsymbol{\gamma}$ and $\boldsymbol{\sigma}'_s$ are simultaneously present. Since the exclusion of γ_1 depends on the presence of $\boldsymbol{\sigma}_s$ and $\boldsymbol{\sigma}'_s$, we assume $\gamma_1 = 1$ is automatically applied when necessary. And, with some violation of the notation, we continue to use $\boldsymbol{\gamma}$ to denote $[\gamma_2, ..., \gamma_M]^T$ whenever applicable.

2. **The phase ambiguity**
   The phases of the complex gains are also not jointly identifiable, because only the phase differences can be inferred from the covariance data. Therefore, we fix the phase of the first receiver element $\phi_1 = 0$ as a reference. Similarly, we continue to use $\boldsymbol{\phi}$ to denote $[\phi_2, ..., \phi_M]^T$.

Upon resolving the system ambiguities, the derivation can continue. We first partition the Jacobian according to the parameter ordering in $\boldsymbol{\theta}$, i.e.

$$\mathbf{J} = [\mathbf{J}_\gamma, \mathbf{J}_\phi, \mathbf{J}_{\sigma_s}, \mathbf{J}_{\sigma_n}, \mathbf{J}_{\sigma'_s}, \mathbf{J}_{\sigma'_n}]. \tag{2.5}$$

It is shown in [17, (12)-(15), (17)] that those Jacobian submatrices can be expressed in closed-form as

$$\mathbf{J}_\gamma = \left[(\overline{\mathbf{G}\mathbf{A}\boldsymbol{\Sigma}_s\mathbf{A}^H}\,\boldsymbol{\Phi}) \circ \mathbf{I} + \mathbf{I} \circ (\mathbf{G}\mathbf{A}\boldsymbol{\Sigma}_s\mathbf{A}^H\,\overline{\boldsymbol{\Phi}})\right] \boldsymbol{\Psi}_s^T \tag{2.6}$$

$$\mathbf{J}_\phi = \mathrm{j}\left[(\overline{\mathbf{G}\mathbf{A}\boldsymbol{\Sigma}_s\mathbf{A}^H}\,\mathbf{G}) \circ \mathbf{I} - \mathbf{I} \circ (\mathbf{G}\mathbf{A}\boldsymbol{\Sigma}_s\mathbf{A}^H\,\overline{\mathbf{G}})\right] \boldsymbol{\Psi}_s^T \tag{2.7}$$

$$\mathbf{J}_{\sigma_s} = \overline{\mathbf{G}\mathbf{A}} \circ \mathbf{G}\mathbf{A} \tag{2.8}$$

$$\mathbf{J}_{\sigma_n} = \mathbf{I} \circ \mathbf{I}. \tag{2.9}$$

$$\mathbf{J}_{\sigma'_s} = \overline{\mathbf{G}\mathbf{A}'} \circ \mathbf{G}\mathbf{A}' \tag{2.10}$$

$$\mathbf{J}_{\sigma'_n} = \mathbf{I} \circ \mathbf{I}. \tag{2.11}$$

where the $\boldsymbol{\Psi}_s^T$ is a column selection matrix (i.e. transpose of a row selection matrix) used to exclude the first column of its left operand, eliminating the ambiguities in magnitude and phase. The closed-from solution of the FIM can then be calculated by the Bangs' formula as previously introduced.

2.3 Nuisance parameters

By collecting the nuisance parameters in a vector $\boldsymbol{\nu} = [\boldsymbol{\gamma}^T, \boldsymbol{\phi}^T, \boldsymbol{\sigma}_n^T, \boldsymbol{\sigma}_s'^T, \boldsymbol{\sigma}_n'^T]^T$, the FIM and CRB matrix can be split into 4 submatrices,

$$\mathbf{F} = \begin{bmatrix} \mathbf{F}_{\boldsymbol{\sigma}_s\boldsymbol{\sigma}_s} & \mathbf{F}_{\boldsymbol{\sigma}_s\boldsymbol{\nu}} \\ \mathbf{F}_{\boldsymbol{\nu}\boldsymbol{\sigma}_s} & \mathbf{F}_{\boldsymbol{\nu}\boldsymbol{\nu}} \end{bmatrix}, \qquad \mathbf{C} = \begin{bmatrix} \mathbf{C}_{\boldsymbol{\sigma}_s\boldsymbol{\sigma}_s} & \mathbf{C}_{\boldsymbol{\sigma}_s\boldsymbol{\nu}} \\ \mathbf{C}_{\boldsymbol{\nu}\boldsymbol{\sigma}_s} & \mathbf{C}_{\boldsymbol{\nu}\boldsymbol{\nu}} \end{bmatrix}. \tag{2.12}$$

As will be demonstrated in Chapter 4, in some scenarios we assume a subset of the nuisance parameters to be known. Those known parameters should be left out of $\boldsymbol{\nu}$ since there is no need to estimate them anymore.

For image estimation, we are only interested in $\mathbf{C}_{\sigma_s\sigma_s}$. The closed-form solution of $\mathbf{C}_{\sigma_s\sigma_s}$ involves a block matrix inversion which can be obtained through the Schur complement. Depending on the invertibility of the FIM submatrices, two equivalent forms are available [18]:

- if $\mathbf{F}_{\sigma_s\sigma_s}$ is invertible

$$\mathbf{C}_{\sigma_s\sigma_s} = \mathbf{F}_{\sigma_s\sigma_s}^{-1} + \mathbf{F}_{\sigma_s\sigma_s}^{-1}\mathbf{F}_{\sigma_s\nu}(\mathbf{F}_{\nu\nu} - \mathbf{F}_{\nu\sigma_s}\mathbf{F}_{\sigma_s\sigma_s}^{-1}\mathbf{F}_{\sigma_s\nu})^{-1}\mathbf{F}_{\nu\sigma_s}\mathbf{F}_{\sigma_s\sigma_s}^{-1} \tag{2.13}$$

- if $\mathbf{F}_{\nu\nu}$ is invertible

$$\mathbf{C}_{\sigma_s\sigma_s} = (\mathbf{F}_{\sigma_s\sigma_s} - \mathbf{F}_{\sigma_s\nu}\mathbf{F}_{\nu\nu}^{-1}\mathbf{F}_{\nu\sigma_s})^{-1}. \tag{2.14}$$

It is clear from (2.14) that if there are no nuisance parameters, the CRB matrix would just be a direct inversion of $\mathbf{F}_{\sigma_s\sigma_s}$. Incorporating the nuisance parameters causes a reduction in the Fisher information, and hence raises the resulting CRB.

It is obvious that a necessary condition for (2.13) and (2.14) to be valid is the invertibility of $\mathbf{F}_{\sigma_s\sigma_s}$ and $\mathbf{F}_{\nu\nu}$ respectively. The next subsections will discuss such conditions in detail.

2.3.1 Invertibility of $\mathbf{F}_{\sigma_s\sigma_s}$

As demonstrated in [19], the identifiability of the sources (and therefore the invertibility of $\mathbf{F}_{\sigma_s\sigma_s}$) depends on the degrees of freedom (DOF) provided by the difference co-array. The source power $\boldsymbol{\sigma}_s$ is only fully identifiable when the criterion "DOF $\geq$ number of sources" is fulfilled. To calculate the DOF of a difference co-array residing on a regular grid, we employ the concept of the weight function introduced in [19]. The weight function weight($\mathbf{d}$) shows the multiplicity of a specific baseline $\mathbf{d}$ provided by a difference co-array. Thus, this co-array's DOF can be computed by the l_0-norm of its weight function.

For a 1D array on an evenly spaced receiver domain, it can be described by a binary sequence $w(n)$, which indicates whether the k-th position has an array element or not by having $w(k) = 1$ or 0. The weight function for its co-array is therefore given by [19, (6)]

$$\text{weight}(n) = w(n) \circledast w(-n) \tag{2.15}$$

where $\circledast$ denotes the convolution operation. Such a result has important implications that will be demonstrated in Section 4.2.2. But for now, it is clear that (2.13) is not always valid.

2.3.2 Invertibility of nuisance-related FIMs

It is sometimes convenient to consider the gain-related parts together. Therefore, we aggregate the magnitudes and phases of the gains into a single vector $[\boldsymbol{\gamma}^T, \boldsymbol{\phi}^T]^T$, and denote the FIM and CRB matrix for the corresponding indices as

$$\mathbf{F}_{gg} = \begin{bmatrix} \mathbf{F}_{\gamma\gamma} & \mathbf{F}_{\gamma\phi} \\ \mathbf{F}_{\phi\gamma} & \mathbf{F}_{\phi\phi} \end{bmatrix}, \qquad \mathbf{C}_{gg} = \begin{bmatrix} \mathbf{C}_{\gamma\gamma} & \mathbf{C}_{\gamma\phi} \\ \mathbf{C}_{\phi\gamma} & \mathbf{C}_{\phi\phi} \end{bmatrix}. \tag{2.16}$$

Note that $\mathbf{F}_{gg}$ is part of $\mathbf{F}_{\boldsymbol{\nu}\boldsymbol{\nu}}$, and likewise for $\mathbf{C}_{gg}$.

Among the nuisance parameters $\boldsymbol{\nu} = [\boldsymbol{\gamma}^T, \boldsymbol{\phi}^T, \boldsymbol{\sigma}_n^T, \boldsymbol{\sigma}_s'^T, \boldsymbol{\sigma}_n'^T]^T$, it is trivial to prove that the invertibility of the noise-related FIM $\mathbf{F}_{\sigma_n\sigma_n}$ is guaranteed (same applies to $\mathbf{F}_{\sigma_n'\sigma_n'}$). Also, in most imaging scenarios, the number of calibration sources is small compared to the DOF provided by the array, so $\boldsymbol{\sigma}_s'$ are unusually fully identifiable. Thus, we only consider the invertibility analysis of the complex gain-related term $\mathbf{F}_{gg}$.

Proposition: For the sensor system described by the model (1.7), if a phase reference is chosen to eliminate the phase ambiguity, the complex gains are always identifiable, i.e. $\mathbf{F}_{gg}$ is always full-rank.

Proof: *see Appendix 1.*

The immediate consequence is that in the usual imaging scenarios (i.e. when the mentioned conditions hold), $\mathbf{F}_{\nu\nu}$ is invertible, and thus we are allowed to express the apparent FIM (the direct inversion of $\mathbf{C}_{\sigma_s\sigma_s}$) via (2.14). This is attractive since as will be shown in the next chapter, the apparent FIM is extensively used as the optimization objective.

3 Optimization

This chapter poses the optimization problem for which we solve to obtain the optimal sensor locations. As the CRB-based objective functions can be highly nonlinear, in Section 3.1 we first discretize the problem and adopt a combinatorial optimization framework. Then the closed-form FIM derived in Chapter 2 is augmented to account for the sensor selection as well as to eliminate the dependency on the true parameter value $\boldsymbol{\theta}$, such that it can be used for the adopted framework. Since the combinatorial problem is NP-hard, in Section 3.2 we introduce two approaches to solve it by approximation.

3.1 Problem formulation

3.1.1 Combinatorial optimization problem

First, we re-iterate the problem statement

$$\begin{aligned} \max_{\mathcal{Z}} \quad & \text{image quality} \\ \text{s.t.} \quad & \text{number of sensors} \leq K. \end{aligned} \tag{3.1}$$

Optimization objective. As mentioned previously, in this project we choose to use the CRB as the optimization objective since it represents the best achievable performance an array design can provide without regarding the actual estimation method being used. However, since the estimation parameter is multi-variable, the CRB becomes a matrix. The estimation objective needs to be a scalar function of the CRB matrix, i.e. $f(\mathbf{C}) = f(\mathbf{F}^{-1})$.

Different choices of f have been proposed in the past:

1. E-optimality - $f = \lambda_{\min}(\mathbf{F})$ [20]
2. A-optimality - $f = \operatorname{tr}(\mathbf{F}^{-1})$ [21]
3. D-optimality - $f = \log\det(\mathbf{F})$ [22]

Among those optimality conditions, we choose to adopt the A-optimality criterion, i.e. $f = \operatorname{tr}(\mathbf{F}^{-1})$, to assess the imaging quality since it represents the total estimation variance [15].

Optimization variable. The objective $f = \operatorname{tr}(\mathbf{F}^{-1})$ is a non-linear function of the receiver locations $\mathcal{Z}$, thus can be hard to solve directly. Extensive researches, e.g. [20], have suggested transferring the problem into a combinatorial optimization problem through discretization of the receiver domain. This allows us to pre-compute the contribution to the objective function at each location separately, and then to search for a scheme that combines those individual contributions optimally. In such a way, the

search space can be greatly reduced (from a continuous domain down to M discretized candidates). Moreover, a number of combinatorial optimization frameworks can be adopted, such as convex relaxations [20] and greedy algorithms [21].

The formulation is made possible by assigning each candidate position with a binary variable w_i to indicate whether the position is selected or not. The binary variables are stacked together to form a selection vector $\mathbf{w}$. The optimization problem can therefore be stated as

$$\begin{aligned} \min_{\mathbf{w}} \quad & \operatorname{tr}\Big(\mathbf{C}_{\sigma_s\sigma_s}(\mathbf{w};\,\boldsymbol{\theta})\Big) = \operatorname{tr}\Big(\tilde{\mathbf{F}}(\mathbf{w};\,\boldsymbol{\theta})\Big)^{-1} \\ \text{s.t.} \quad & \mathbf{w} \in \{0,1\}^M \\ & ||\mathbf{w}||_0 \leq K. \end{aligned} \tag{3.2}$$

where the apparent FIM $\tilde{\mathbf{F}}$ (the direct inversion of $\mathbf{C}_{\sigma_s\sigma_s}$) is

$$\tilde{\mathbf{F}} = \mathbf{C}_{\sigma_s\sigma_s}^{-1} = \mathbf{F}_{\sigma_s\sigma_s} - \mathbf{F}_{\sigma_s\nu}\,\mathbf{F}_{\nu\nu}^{-1}\,\mathbf{F}_{\nu\sigma_s}. \tag{3.3}$$

Note that it is the CRB sub-block $\mathbf{C}_{\sigma_s\sigma_s}$ rather than the full CRB that is used in the objective function, as we are only interested in the estimation performance of $\boldsymbol{\sigma}_s$. Also, note that the matrix $\tilde{\mathbf{F}}$ is a function of the selection vector $\mathbf{w}$ and parameterized by $\boldsymbol{\theta}$.

3.1.2 Effect of sensor selection

Before introducing the selection methods, it is helpful to review how to split out the contribution from each position to the overall FIM, such that a closed-form calculation of the FIM is still possible after incorporating $\mathbf{w}$.

Selecting a subset of sensors according to a certain $\mathbf{w}$ can be realized by applying a selection matrix $\boldsymbol{\Psi}_w$ on the original array processing data model, i.e.

$$\mathbf{x}_w = \boldsymbol{\Psi}_w\big(\mathbf{G}\mathbf{A}\,\mathbf{s} + \mathbf{n}\big) \tag{3.4}$$

where $\boldsymbol{\Psi}_w$ is essentially $\operatorname{diag}(\mathbf{w})$ but with its all-zero rows removed. Therefore for the data covariance, we obtain

$$\mathbf{R}_w = \boldsymbol{\Psi}_w\,\mathbf{R}\,\boldsymbol{\Psi}_w^T \tag{3.5}$$

$$\begin{aligned} \mathbf{r}_w &= \operatorname{vec}(\boldsymbol{\Psi}_w\,\mathbf{R}\,\boldsymbol{\Psi}_w^T) \\ &= \big[(\boldsymbol{\Psi}_w^H)^T \otimes \boldsymbol{\Psi}_w\big]\,\mathbf{r} \qquad [1, (2)] \qquad (3.6) \\ &= (\boldsymbol{\Psi}_w \otimes \boldsymbol{\Psi}_w)\,\mathbf{r}. \qquad (3.7) \end{aligned}$$

Denoting $\mathbf{v} = \mathbf{w} \otimes \mathbf{w}$ and $\boldsymbol{\Psi}_v = \boldsymbol{\Psi}_w \otimes \boldsymbol{\Psi}_w$, we have

$$\mathbf{r}_w = \boldsymbol{\Psi}_v\,\mathbf{r} \tag{3.8}$$

This would change the FIM computation $\mathbf{F} = \mathbf{J}^H\,(\overline{\mathbf{R}}^{-1} \otimes \mathbf{R}^{-1})\,\mathbf{J}$ from two aspects:

1. The Wishart covariance $\boldsymbol{\Sigma} = \overline{\mathbf{R}} \otimes \mathbf{R}$ now becomes

$$\begin{aligned}
\boldsymbol{\Sigma}_w &= \overline{\mathbf{R}_w} \otimes \mathbf{R}_w && (3.9)\\
&= (\boldsymbol{\Psi}_w \, \overline{\mathbf{R}_w} \, \boldsymbol{\Psi}_w^T) \otimes (\boldsymbol{\Psi}_w \, \mathbf{R}_w \, \boldsymbol{\Psi}_w^T) && (3.10)\\
&= (\boldsymbol{\Psi}_w \otimes \boldsymbol{\Psi}_w)\,(\overline{\mathbf{R}_w} \otimes \mathbf{R}_w)\,(\boldsymbol{\Psi}_w^T \otimes \boldsymbol{\Psi}_w^T) \qquad [1, (2)] && (3.11)\\
&= \boldsymbol{\Psi}_v \, \boldsymbol{\Sigma} \, \boldsymbol{\Psi}_v^T && (3.12)
\end{aligned}$$

   which is the original $\boldsymbol{\Sigma}$ being pre- and post-multiplied by $\boldsymbol{\Psi}_v$ to exclude the covariance data associated with the candidate sensors not being selected.

2. The Jacobian sub-blocks are modified.

   (a) For the source-related parameters $\boldsymbol{\sigma}_s$ and $\boldsymbol{\sigma}'_s$, we only need to exclude the rows of the Jacobians corresponding to the invalid covariance data, i.e.

$$\begin{aligned}
\mathbf{J}_{\sigma_s;w} &= \boldsymbol{\Psi}_v \, \mathbf{J}_{\sigma_s} && (3.13)\\
\mathbf{J}_{\sigma'_s;w} &= \boldsymbol{\Psi}_v \, \mathbf{J}_{\sigma_s}. && (3.14)
\end{aligned}$$

   (b) For the sensor-related parameters $\boldsymbol{\gamma}, \boldsymbol{\phi}^T, \boldsymbol{\sigma}_n$ and $\boldsymbol{\sigma}'_n$, an additional post-multiplication by $\boldsymbol{\Psi}_w^T$ is required. This is to exclude the columns associated with the sensors that are not selected. More specifically, if a sensor is not selected, we do not need to estimate its gain or noise power. This gives us

$$\begin{aligned}
\mathbf{J}_{\gamma;w} &= \boldsymbol{\Psi}_v \, \mathbf{J}_{\gamma} \, \boldsymbol{\Psi}_w^T \, \boldsymbol{\Psi}_s^T && (3.15)\\
\mathbf{J}_{\phi;w} &= \boldsymbol{\Psi}_v \, \mathbf{J}_{\phi} \, \boldsymbol{\Psi}_w^T \, \boldsymbol{\Psi}_s^T && (3.16)\\
\mathbf{J}_{\sigma_n;w} &= \boldsymbol{\Psi}_v \, \mathbf{J}_{\sigma_n} \, \boldsymbol{\Psi}_w^T && (3.17)\\
\mathbf{J}_{\sigma'_n;w} &= \boldsymbol{\Psi}_v \, \mathbf{J}_{\sigma_n} \, \boldsymbol{\Psi}_w^T. && (3.18)
\end{aligned}$$

   Note that $\mathbf{J}_\gamma$ and $\mathbf{J}_\phi$ above are actually slight violations of the notations defined in (2.6) and (2.7). The selection matrices $\boldsymbol{\Psi}_s^T$ for ambiguity elimination are moved to the end since this has to happen after sensor selection.

The FIM sub-blocks can be computed through the procedure above, and then the apparent Fisher $\tilde{\mathbf{F}}$ can be assembled via (3.3).

3.1.3 Eliminating the dependency on true parameter values

Due to the non-linearity of the model, the objective function $\text{tr}\left[\tilde{\mathbf{F}}(\mathbf{w};\boldsymbol{\theta})\right]^{-1}$ and subsequently the optimal solution $\mathbf{w}^*(\boldsymbol{\theta})$ are dependent on the true parameter values $\boldsymbol{\theta}$. But the selection must be made without the knowledge of the exact $\boldsymbol{\theta}$.

In [20], it is suggested to substitute the worst-case parameter $\boldsymbol{\theta}_{\text{worst}}$ in the FIM during selection to break the dependency. In this project, we proposed to decouple the true $\boldsymbol{\theta}$ and the objective function by taking the expectation over an assumed distribution of $\boldsymbol{\theta}$, i.e. $\mathbb{E}_{\boldsymbol{\theta}}\Big[\,\text{tr}\left\{\tilde{\mathbf{F}}(\mathbf{w};\,\boldsymbol{\theta})^{-1}\right\}\Big]$, so that we can account for the general performance of the array under different parameter settings.

However, direct computation of the expectation is almost impossible due to the complexity of the objective function. It was also attempted to approximate the expectation by sampling or Taylor expansion, but the non-linearity and the high dimensionality prevented further progress to be made. So the proposed solution is to plug in $\mathbb{E}_{\boldsymbol{\theta}}[\boldsymbol{\theta}]$ instead. Hence the optimization problem becomes

$$\begin{aligned} \min_{\mathbf{w}} \quad & \operatorname{tr}\left(\tilde{\mathbf{F}}(\mathbf{w};\, \mathbb{E}[\boldsymbol{\theta}])^{-1}\right) \\ \text{s.t.} \quad & \mathbf{w} \in \{0,1\}^M \\ & ||\mathbf{w}||_0 \leq K. \end{aligned} \tag{3.19}$$

Clearly this introduces an additional error since the trace-inverse is convex and by Jensen's inequality [23] we have

$$\mathbb{E}\Big[\operatorname{tr}\left\{\tilde{\mathbf{F}}(\mathbf{w};\, \boldsymbol{\theta})^{-1}\right\}\Big] \geq \operatorname{tr}\Big\{\mathbb{E}\big[\tilde{\mathbf{F}}(\mathbf{w};\, \boldsymbol{\theta})^{-1}\big]\Big\} \geq \operatorname{tr}\left\{\mathbb{E}\big[\tilde{\mathbf{F}}(\mathbf{w};\, \boldsymbol{\theta})\big]\right\}^{-1} \geq \operatorname{tr}\left\{\tilde{\mathbf{F}}(\mathbf{w};\, \mathbb{E}[\boldsymbol{\theta}])\right\}^{-1}. \tag{3.20}$$

Among those choices, the current objective $\operatorname{tr}\left\{\tilde{\mathbf{F}}(\mathbf{w};\, \mathbb{E}[\boldsymbol{\theta}])\right\}^{-1}$ is the loosest lower bound of the desired objective function $\mathbb{E}\Big[\operatorname{tr}\left\{\tilde{\mathbf{F}}(\mathbf{w};\, \boldsymbol{\theta})^{-1}\right\}\Big]$, which is undesirable. However, the other objectives are too complicated to be expressed in closed-form. Numerical methods, Monte-Carlo simulation for example, might not be a viable choice due to the high dimensionality of the parameters space and the extremely large number of samples required to stabilize the output. Therefore, we believe our choice of the objective is the best compromise.

3.2 Selection methods

In this project we consider two optimization frameworks to efficiently solve the problem stated in (3.19), which are a greedy algorithm for the log-determinant (log-det) surrogate [24] and convex optimization with semidefinite relaxation (SDR) [21].

3.2.1 Greedy algorithm

In the past years, the greedy algorithm has been proven to be effective to solve the NP-hard combinatorial optimization problem by approximation. The sub-optimal solution is found by sequentially selecting the candidate that gives the maximum improvement in terms of the objective function. The exact algorithm can be found in [24].

Instead of using the original trace-inverse objective function, we implement the D-optimality log-det

$$f(\mathbf{w};\, \mathbb{E}[\boldsymbol{\theta}]) = \log\det\left\{\tilde{\mathbf{F}}(\mathbf{w};\, \mathbb{E}[\boldsymbol{\theta}])\right\}. \tag{3.21}$$

The main consideration is that the log-det has proven to be a submodular function for many similar sensor selection problems and has a performance lower bound guaranteed [25]. In contrat, the trace-inverse objective function is not submodular.

To ensure the inversion of $\tilde{\mathbf{F}}$ is valid, a diagonal matrix $\epsilon\mathbf{I}$ is added to raise the floor of eigenvalues of the FIM where ϵ is sufficiently small. Furthermore, an $N \log \epsilon$ term is subtracted from the objective function such that the the log-det is normalized (i.e. $f(\emptyset) = 0$) [24]. The final objective function used in the greedy algorithm is

$$f(\mathbf{w};\, \mathbb{E}[\boldsymbol{\theta}]) = \log\det\left\{\tilde{\mathbf{F}}(\mathbf{w};\, \mathbb{E}[\boldsymbol{\theta}]) + \epsilon\mathbf{I}\right\} - M\log\epsilon. \tag{3.22}$$

3.2.2 Convex optimization

For the problem (3.19), while the trace-inverse objective is convex on $\mathbf{w}$, both the Boolean and the l_0-norm constraints are nonconvex. Different approaches have been proposed to resolve this issue.

- In [20], the Boolean constraint $\mathbf{w} \in \{0,1\}^M$ is relaxed to a convex box constraint $\mathbf{w} \in [0,1]^M$, whereas the l_0-norm was approximated by the convex l_1-norm.
- In [21], the conversion to a convex problem was realized by using semidefinite relaxation [26]. Particularly, [21] considers the cases when the noise is white as well as when the noise is weakly correlated. The latter fits our project's context since the Wishart covariance $\boldsymbol{\Sigma}$ is not completely but almost diagonal because of the low SNR.

In this project, to make the problem simple, we approximate the finite-snapshot noise $\mathbf{e}$ as being white, hence the off-diagonal entries of $\boldsymbol{\Sigma}$ are assumed negligible. The rationale behind is that for radio astronomy the SNR is usually low, therefore the diagonal noise variance matrix $\boldsymbol{\Sigma}_n$ becomes dominant in $\mathbf{R}$. Since $\boldsymbol{\Sigma} = \overline{\mathbf{R}} \otimes \mathbf{R}$, the Wishart covariance $\boldsymbol{\Sigma}$ can also be approximated as diagonal.

As a consequence, for a linear model, the overall FIM is just a summation of the individual rank-one FIMs provided at each sensor location [20] [21]. However, our problem (3.19) has three intrinsic difficulties compared to the convex formulation in [21]:

- **Nuisance parameters are involved.**
  This implies that we are only interested in a sub-block of the full CRB matrix, and (3.3) needs to be applied to obtain the apparent FIM $\tilde{\mathbf{F}}$. Unfortunately, this makes a convex problem much harder to formulate, since the apparent FIM is no longer a simple summation of the rank-one matrices.

  The proposed solution is to first construct the full FIM $\mathbf{F}$, and then extracting the corresponding rows and columns from $\mathbf{F}^{-1}$ to obtain the sub-block of interest $\mathbf{C}_{\sigma_s\sigma_s}$.

- **Post multiplication of selection matrices.**
  To illustrate the issue, we first express the combinatorial optimization problem (3.2) explicitly in terms of the selection vector $\mathbf{w}$. Substituting the post-selection Jacobians and Wishart covariance into Bang's formula gives

$$\mathbf{F}(\mathbf{w}) = \boldsymbol{\Psi}_\theta\, \mathbf{J}^H\, \boldsymbol{\Psi}_v^T\, (\boldsymbol{\Psi}_v\, \boldsymbol{\Sigma}\, \boldsymbol{\Psi}_v)^{-1} \boldsymbol{\Psi}_v\, \mathbf{J}\, \boldsymbol{\Psi}_\theta^T \tag{3.23}$$

where $\mathbf{\Psi}_\theta = [\mathbf{\Psi}_w^T\mathbf{\Psi}_s^T, \mathbf{\Psi}_w^T\mathbf{\Psi}_s^T, \mathbf{I}, \mathbf{\Psi}_w^T, \mathbf{I}, \mathbf{\Psi}_w^T]^T$ aggregates all the post-multiplications in (3.15)-(3.18). The $\mathbf{\Psi}_\theta$ terms apparently introduce additional complications in the formulation established in [21], and it would be a challenge to find a feasible way to include these terms while maintaining the convexity of the formulation. Therefore, we omit the $\mathbf{\Psi}_\theta$ terms (which makes sense since Chapter 6 demonstrates that those entries' influence on the overall FIM is negligible) and the problem reduces to

$$\check{\mathbf{F}}(\mathbf{w}) = \mathbf{J}^H \mathbf{\Psi}_v^T (\mathbf{\Psi}_v \mathbf{\Sigma} \mathbf{\Psi}_v^T)^{-1} \mathbf{\Psi}_v \mathbf{J} \tag{3.24}$$

However, since the modified FIM $\check{\mathbf{F}}(\mathbf{w})$ now includes the entries for non-existing parameters, it is no longer invertible due to the lack of identifiability. Therefore, we employ the $\epsilon\mathbf{I}$ term again to make sure restore invertibility,

$$\check{\mathbf{F}}(\mathbf{w}) = \mathbf{J}^H \mathbf{\Psi}_v^T (\mathbf{\Psi}_v \mathbf{\Sigma} \mathbf{\Psi}_v^T)^{-1} \mathbf{\Psi}_v \mathbf{J} + \epsilon\mathbf{I}. \tag{3.25}$$

As $\mathbf{\Sigma}$ is approximated as being diagonal, the inversion can be applied on $\mathbf{\Sigma}$ only [21], i.e.

$$\begin{aligned}
\check{\mathbf{F}}(\mathbf{w}) &= \mathbf{J}^H \mathbf{\Psi}_v^T \mathbf{\Psi}_v \mathbf{\Sigma}^{-1} \mathbf{\Psi}_v^T \mathbf{\Psi}_v \mathbf{J} + \epsilon\mathbf{I} && (3.26)\\
&= \mathbf{J}^H \operatorname{diag}(\mathbf{w} \otimes \mathbf{w}) \mathbf{\Sigma}^{-1} \operatorname{diag}(\mathbf{w} \otimes \mathbf{w}) \mathbf{J} + \epsilon\mathbf{I} && (3.27)\\
&= \mathbf{J}^H \left[\operatorname{diag}(\mathbf{w} \otimes \mathbf{w}) \odot \mathbf{\Sigma}^{-1}\right] \mathbf{J} + \epsilon\mathbf{I} && (3.28)
\end{aligned}$$

- **Covariance data is used.**
  The sensor selection is made on the received data $\mathbf{x}$, but it is the covariance model that is actually used in the FIM derivation. Such a mismatch results in the $\operatorname{diag}(\mathbf{w} \otimes \mathbf{w})$ in (3.28) rather than a $\operatorname{diag}(\mathbf{w})$ term. To resolve this issue, we exploit the relationship $\operatorname{vec}(\mathbf{W}) = \mathbf{w} \otimes \mathbf{w}$ and arrive at an optimization problem that is linear in $\mathbf{W}$,

$$\begin{aligned}
\min_{\mathbf{W},\mathbf{w}} \quad & \operatorname{tr}\left(\mathbf{J}^H \left[\operatorname{diag}\left(\operatorname{vec}(\mathbf{W})\right) \odot \mathbf{\Sigma}^{-1}\right] \mathbf{J} + \epsilon\mathbf{I}\right)^{-1} \\
\text{s.t.} \quad & \mathbf{W} = \mathbf{w}\mathbf{w}^T \\
& \mathbf{w} \in \{0,1\}^M \\
& ||\mathbf{w}||_0 \leq K.
\end{aligned} \tag{3.29}$$

  Note that although the formulation is similar to the one in [21], the function of the auxiliary variable $\mathbf{W}$ is different. In [21], $\mathbf{W}$ is employed to relax the rank-one constraint in the problem. But in our formulation, $\mathbf{W}$ is used to replace the diagonalized Kronecker product.

  Finally, we extract $\mathbf{C}_{\sigma_s\sigma_s}$ from $\mathbf{C}$ by using the selection matrices $\mathbf{\Psi}_{\sigma_s}$ and $\mathbf{\Psi}_{\sigma_s}^T$. The Schur complement is applied to achieve a convex relaxation as in [21], which

gives

$$
\begin{aligned}
\min_{\mathbf{W},\mathbf{w},\check{\mathbf{F}},\mathbf{C}} \quad & \operatorname{tr}(\boldsymbol{\Psi}_{\sigma_s}\,\mathbf{C}\,\boldsymbol{\Psi}_{\sigma_s}^{T}) \\
\text{s.t.} \quad & \begin{bmatrix} \mathbf{C} & \mathbf{I} \\ \mathbf{I} & \check{\mathbf{F}} \end{bmatrix} \succeq 0 \\
& \check{\mathbf{F}} = \mathbf{J}^{H}\left[\operatorname{diag}\left(\operatorname{vec}(\mathbf{W})\right) \odot \boldsymbol{\Sigma}^{-1}\right]\mathbf{J} + \epsilon\mathbf{I} \\
& \operatorname{tr}(\mathbf{W}) \leq K \\
& \operatorname{diag}(\mathbf{W}) = \mathbf{w} \\
& \begin{bmatrix} \mathbf{W} & \mathbf{w} \\ \mathbf{w}^{T} & 1 \end{bmatrix} \succeq 0.
\end{aligned} \tag{3.30}
$$

The solution $\mathbf{W}^*$ of the SDR problem (3.30) is usually not exactly rank-one, therefore not being feasible and cannot be directly used. To get back a valid binary selection vector, a subsequent randomization scheme is commonly applied [26]. The randomization process treats the convex solution $\mathbf{W}^*$ as a probability distribution, and draws realizations from it. The realizations are subsequently rounded to satisfy the Boolean constraint. The final output is the best performing candidate Boolean solutions. The exact formulation of the randomization scheme is problem-dependent. However, for the derived convex optimization problem (3.30), a suitable randomization algorithm has already been proposed in [21], and it is employed in this project.

4 Sensor Selection

This chapter details the sensor selection results for three main estimation scenarios. Section 4.1 introduces all the considered scenarios, in which the associated FIMs are constructed for different subsets of the parameters in $\boldsymbol{\theta}$, and we focus on different parameters-of-interest. Section 4.2 to 4.4 show the sensor selection results for the three estimation scenarios and provide related analysis.

4.1 Estimation scenarios

As mentioned, in radio astronomy interferometry systems, imaging usually involves an iterative procedure. There exist a group of strong astronomical sources that are being constantly tracked, and their positions in the sky are usually well-known. Those sources can help with the initial system calibration to set up the iterative procedure until the system conditions are well estimated and sufficient weaker sources are identified. To abstract this complicated process, we split the observation data into two categories:

- Imaging observation $\mathbf{x} = \mathbf{GAs} + \mathbf{n}$
- Calibration observation $\mathbf{x}' = \mathbf{GA}'\mathbf{s}' + \mathbf{n}'$

The calibration observations are obtained in the same way as in (1.5) but with the calibration sources.

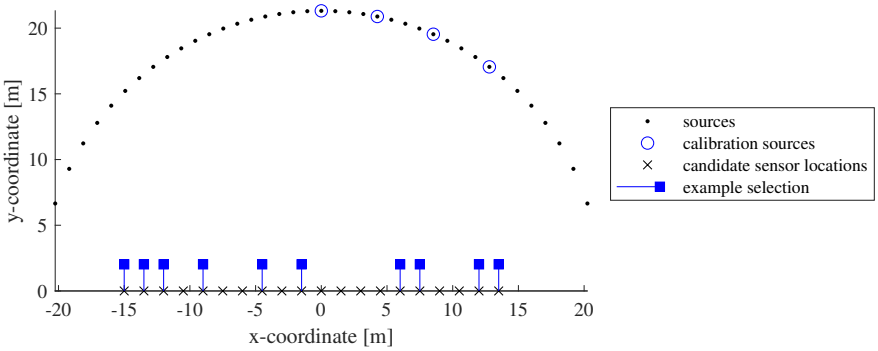

Figure 4.1: Example 1D geometry of the estimation problem

An example problem geometry is shown in figure 4.1. The candidate sensor locations form a regular grid with a spacing of $\frac{\lambda}{2}$, where $\lambda = \frac{c}{f_c}$ is the wavelength determined by the ratio of the speed of light c and the narrowband centre frequency f_c. The sky is segmented in a way that the discretized source locations have a uniform x-projection. This geometry is assumed for the remainder this chapter.

To simplify the analysis, we consider the following three different estimation scenarios.

1. **Pure imaging**, with weak-source self-calibration
   (only the imaging observations are used)
2. **Pure calibration**, with strong calibrators
   (only the calibration observations are used)
3. **Imaging with enhanced calibration**, i.e. the complete scenario
   (both the imaging and calibration observations are used)

The first two scenarios only describe the problem partially, which paves the way towards the final one, the complete estimation problem. The details of the three scenarios are given in the next subsections.

4.1.1 Scenario 1 – Pure imaging, with weak source self-calibration

In the first scenario, we consider the pure imaging case (the parameter-of-interest is the imaging source power $\boldsymbol{\sigma}_s$), assuming only the imaging observation $\mathbf{X}$ is available.

There are two sets of nuisance parameters in this setup. The first one is the complex gain $\mathbf{g}$. Even though no calibration observation $\mathbf{X}'$ is used, the complex gain still needs to be estimated from the imaging data $\mathbf{X}$, i.e. self-calibration by the weak imaging sources themselves. The other set of nuisance parameters is the noise power $\boldsymbol{\sigma}_n$.

Since both sets of nuisance parameters can affect the selection, we first study their joint estimation with $\boldsymbol{\sigma}_s$ separately, and then consider them together in the same scene. This is made possible by treating each set as either being known parameters or being unknown, nuisance, and hence to be estimated. This gives four different combinations:

- Scenario 1.1a - $\boldsymbol{\gamma}, \boldsymbol{\phi}$ are known; $\boldsymbol{\sigma}_n$ is known. Without loss of generality, $\mathbf{g}$ is assumed to be $\mathbf{1}$.
- Scenario 1.2a - $\boldsymbol{\gamma}, \boldsymbol{\phi}$ are nuisance; $\boldsymbol{\sigma}_n$ is known.
- Scenario 1.1b - $\boldsymbol{\gamma}, \boldsymbol{\phi}$ are known; $\boldsymbol{\sigma}_n$ is nuisance.
- Scenario 1.2b - $\boldsymbol{\gamma}, \boldsymbol{\phi}$ are nuisance; $\boldsymbol{\sigma}_n$ is nuisance.

The constitutions of the FIMs for those sub-scenarios are shown in figure 4.2 below.

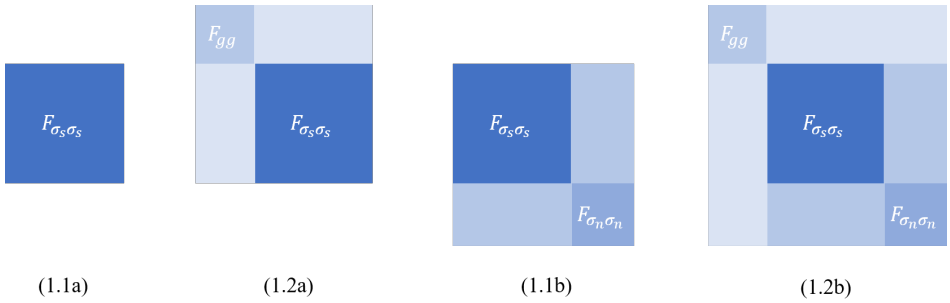

Figure 4.2: The structures of the FIMs for scenario 1 (The color scale does not strictly correspond to the actual magnitudes of the matrix entries.)

4.1.2 Scenario 2 – Pure calibration, with strong calibrator

In scenario 2, we momentarily shift our attention onto the calibration process - the parameter-of-interest is now the instrumental gain $\mathbf{g}$. The objective function is therefore changed to

$$f(\mathbf{w};\, \mathbb{E}[\boldsymbol{\theta}]) = \mathrm{tr}\left(\mathbf{C}_{gg}(\mathbf{w};\, \mathbb{E}[\boldsymbol{\theta}])\right) \tag{4.1}$$

$$= \mathrm{tr}\left(\tilde{\mathbf{F}}'(\mathbf{w};\, \mathbb{E}[\boldsymbol{\theta}])\right)^{-1} \tag{4.2}$$

where $\tilde{\mathbf{F}}'$ is inversion of $\mathbf{C}_{gg}$ (i.e. the apparent FIM for gain estimation). In practice, the $\epsilon\mathbf{I}$ term is brought in whenever necessary to ensure invertibility as already mentioned in Section 3.2.

In this scenario, only the calibration observation $\mathbf{X}'$ is assumed available. Furthermore, we assume the positions of the strong calibration sources are known, which makes sense since they can be tracked from past observations. But the powers of those calibrators, $\boldsymbol{\sigma}'_s$, are assumed to be unknown, even for the most famous astronomical calibrators that have been constantly monitored. The rationale is that the ionospheric scintillation can heavily alter the apparent calibration source powers in practical imaging scenarios [8, p.38]. If we ignore such an effect and keep assuming the apparent source power can be derived from past observations, the instrumental gain should be modelled as significantly unstable (i.e. large variance).

Similarly, four sub-scenarios are considered:

- Scenario 2.1a - $\boldsymbol{\sigma}'_s$ is known; $\boldsymbol{\sigma}'_n$ is known.
- Scenario 2.2a - $\boldsymbol{\sigma}'_s$ is nuisance; $\boldsymbol{\sigma}'_n$ is known.
- Scenario 2.1b - $\boldsymbol{\sigma}'_s$ is known; $\boldsymbol{\sigma}'_n$ is nuisance.
- Scenario 2.2b - $\boldsymbol{\sigma}'_s$ is nuisance; $\boldsymbol{\sigma}'_n$ is nuisance.

The structures of the FIMs are shown in figure 4.3 below.

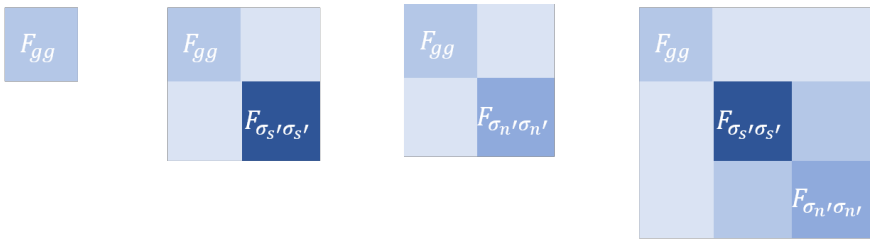

(2.1a) (2.2a) (2.1b) (2.2b)

Figure 4.3: The structures of the FIMs for scenario 2 (The color scale does not strictly correspond to the actual magnitudes of the matrix entries.)

4.1.3 Scenario 3 – Imaging with enhanced calibration

In the final case, we consider the most complete scenario which combines the imaging and separate calibration processes. The observations are stacked to form up a new data vector

$$\mathbf{x}'' = \begin{bmatrix} \mathbf{x}' \\ \mathbf{x} \end{bmatrix} = \begin{bmatrix} \mathbf{G} & \mathbf{0} \\ \mathbf{0} & \mathbf{G} \end{bmatrix} \begin{bmatrix} \mathbf{A}' & \mathbf{0} \\ \mathbf{0} & \mathbf{A} \end{bmatrix} \begin{bmatrix} \mathbf{s}' \\ \mathbf{s} \end{bmatrix} + \begin{bmatrix} \mathbf{n}' \\ \mathbf{n} \end{bmatrix} \tag{4.3}$$

and the covariance becomes

$$\mathbf{R}'' = \begin{bmatrix} \mathbf{R}_{x'x'} & \mathbf{R}_{x'x} \\ \mathbf{R}_{xx'} & \mathbf{R}_{xx} \end{bmatrix} = \begin{bmatrix} \mathbf{R}_{x'x'} & \mathbf{0} \\ \mathbf{0} & \mathbf{R}_{xx} \end{bmatrix} \tag{4.4}$$

which apparently makes the calculation of the FIM more challenging. Fortunately, the new Jacobian matrix can be easily obtained by inserting some all-zero rows into the original Jacobians $\mathbf{J}$ and $\mathbf{J}'$ derived in (2.6)-(2.11), and then stack them together. To see this, we start from the new covariance data

$$\mathbf{r}'' = \mathrm{vec}(\mathbf{R}'') = \begin{bmatrix} \mathrm{vec}\left(\begin{bmatrix} \mathbf{R}_{x'x'} \\ \mathbf{0} \end{bmatrix} \right) \\ \hline \mathrm{vec}\left(\begin{bmatrix} \mathbf{0} \\ \mathbf{R}_{xx} \end{bmatrix} \right) \end{bmatrix} = \begin{bmatrix} \boldsymbol{\Psi}_{r'} \cdot \mathbf{r}' \\ \hline \boldsymbol{\Psi}_{r} \cdot \mathbf{r} \end{bmatrix}, \tag{4.5}$$

where the selection matrices $\boldsymbol{\Psi}_{r'}$ and $\boldsymbol{\Psi}_{r}$ are defined as

$$\boldsymbol{\Psi}_{r'} = \mathbf{I}_M \otimes \begin{bmatrix} 1 \\ 0 \end{bmatrix} \otimes \mathbf{I}_M \tag{4.6}$$

$$\boldsymbol{\Psi}_{r} = \mathbf{I}_M \otimes \begin{bmatrix} 0 \\ 1 \end{bmatrix} \otimes \mathbf{I}_M, \tag{4.7}$$

which effectively add all-zero rows to their right operands. Therefore the new Jacobian is given by

$$\mathbf{J}'' = \begin{bmatrix} \boldsymbol{\Psi}_{r'} \cdot \mathbf{J}' \\ \hline \boldsymbol{\Psi}_{r} \cdot \mathbf{J} \end{bmatrix}. \tag{4.8}$$

And the Fisher can be calculated from $\mathbf{R}''$ and $\mathbf{J}''$ through Bangs' formula,

$$\mathbf{F} = \mathbf{J}''^{H} \left(\overline{\mathbf{R}''}^{-1} \otimes \mathbf{R}''^{-1}\right) \mathbf{J}''. \tag{4.9}$$

Likewise, two sub-scenarios are considered:

- Scenario 3a - $\boldsymbol{\sigma}_n$ is known
- Scenario 3b - $\boldsymbol{\sigma}_n$ is nuisance

The structures of the FIMs are shown in figure 4.4 below.

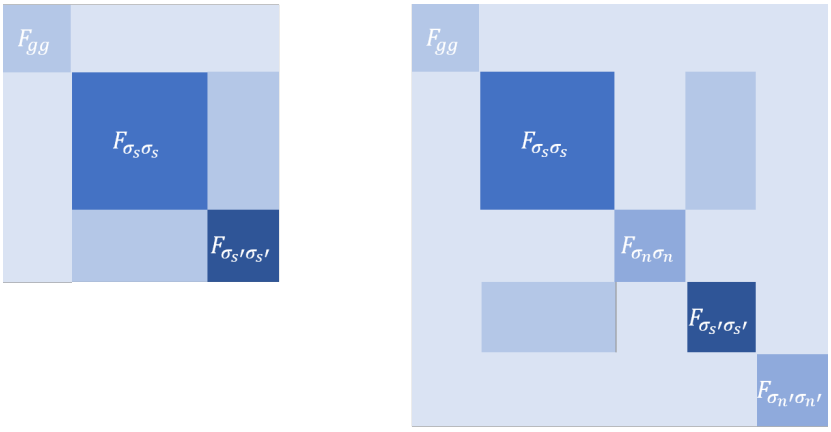

(3a) (3b)

Figure 4.4: The structures of the FIMs for scenario 3 (The color scale does not strictly correspond to the actual magnitudes of the matrix entries.)

Finally, we summarize all the sub-scenarios in table 4.1.

Scenario	parameters-of-interest	nuisance parameters	known parameters
1.1a	$\boldsymbol{\sigma}_s$	-	$\boldsymbol{\gamma}, \boldsymbol{\phi}, \boldsymbol{\sigma}_n$
1.1b	$\boldsymbol{\sigma}_s$	$\boldsymbol{\sigma}_n$	$\boldsymbol{\gamma}, \boldsymbol{\phi}$
1.2a	$\boldsymbol{\sigma}_s$	$\boldsymbol{\gamma}, \boldsymbol{\phi}$	$\boldsymbol{\sigma}_n$
1.2b	$\boldsymbol{\sigma}_s$	$\boldsymbol{\gamma}, \boldsymbol{\phi}, \boldsymbol{\sigma}_n$	-
2.1a	$\boldsymbol{\gamma}, \boldsymbol{\phi}$	-	$\boldsymbol{\sigma}'_s, \boldsymbol{\sigma}'_n$
2.1b	$\boldsymbol{\gamma}, \boldsymbol{\phi}$	$\boldsymbol{\sigma}'_n$	$\boldsymbol{\sigma}'_s$
2.2a	$\boldsymbol{\gamma}, \boldsymbol{\phi}$	$\boldsymbol{\sigma}'_s$	$\boldsymbol{\sigma}'_n$
2.2b	$\boldsymbol{\gamma}, \boldsymbol{\phi}$	$\boldsymbol{\sigma}'_s, \boldsymbol{\sigma}'_n$	-
3a	$\boldsymbol{\sigma}_s$	$\boldsymbol{\gamma}, \boldsymbol{\phi}, \boldsymbol{\sigma}'_s$	$\boldsymbol{\sigma}_n, \boldsymbol{\sigma}'_n$
3b	$\boldsymbol{\sigma}_s$	$\boldsymbol{\gamma}, \boldsymbol{\phi}, \boldsymbol{\sigma}_n, \boldsymbol{\sigma}'_s, \boldsymbol{\sigma}'_n$	-

Table 4.1: A Full list of considered scenarios in the project. The different scenarios are formed by categorizing the estimation parameters differently.

4.2 Scenario 1

4.2.1 Selection results

Due to the limitation of space, the full selection results are included in Appendix A.2. Figure 4.5 plots the objective function $f(\mathbf{w}; \mathbb{E}[\boldsymbol{\theta}]) = \text{tr}\left[(\tilde{\mathbf{F}}+\epsilon\mathbf{I})^{-1}\right]$ against an increasing number of selected antennas K for each sub-scenario. Five array designs are compared, including

1. ULA, which serves as a comparison since generally, ULA is one of the worst-performing arrays due to its low DOF (for identifiability) and spatial spread (for angular resolution).
2. Greedy algorithm
3. Convex optimization, with randomization [26]
4. Convex optimization, without randomization, but only choosing K sensors corresponding to the K highest magnitudes in the direct optimization result $\mathbf{w}^*$
5. Exhaustive search, which serves as a performance lower bound

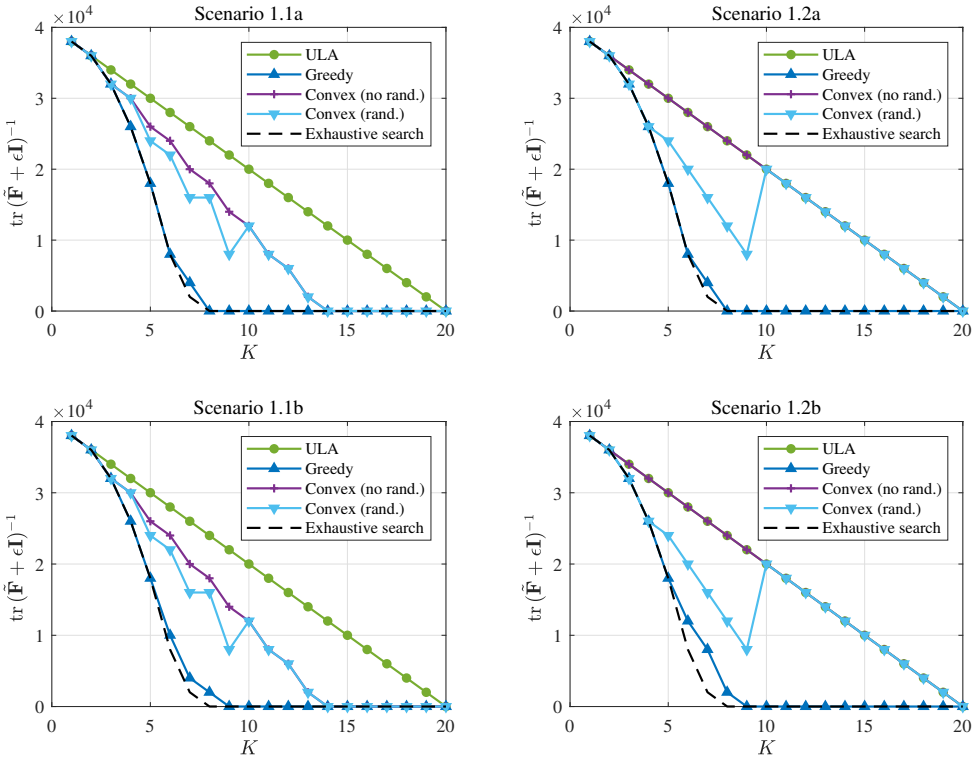

Figure 4.5: Change of CRB with increasing K (Scenario 1)

As shown, the array selected by the greedy algorithm performs the best compared to the other design methods, resulting in a CRB being the closest to the exhaustive search lower bound. The convex optimization, even with the randomization scheme, struggles to obtain reasonable solutions. By inspecting the full selection results in Appendix A.2, we suspect that the poor performance of the convex optimization approach is possibly due to a lack of progress of the randomization scheme for this particular scenario.

Another observation is that the objective function for the exhaustive search decreases monotonically with K in all the sub-scenarios, which matches the intuition that the image estimation error is generally reduced when more receivers are used.

4.2.2 Parameter identifiability

In order to analyze the identifiability of the estimation problem, we focus on scenario 1.2b, and temporarily set $\epsilon \to 0$ such that the objective can blow up to infinity if the FIM is rank-deficient. In the actual experiment, ϵ is set to 10^{-12} rather than 0 to ensure numerical stability of the result (see figure 4.6). The DOF is calculated by using the weight function as introduced in Section 2.3.1.

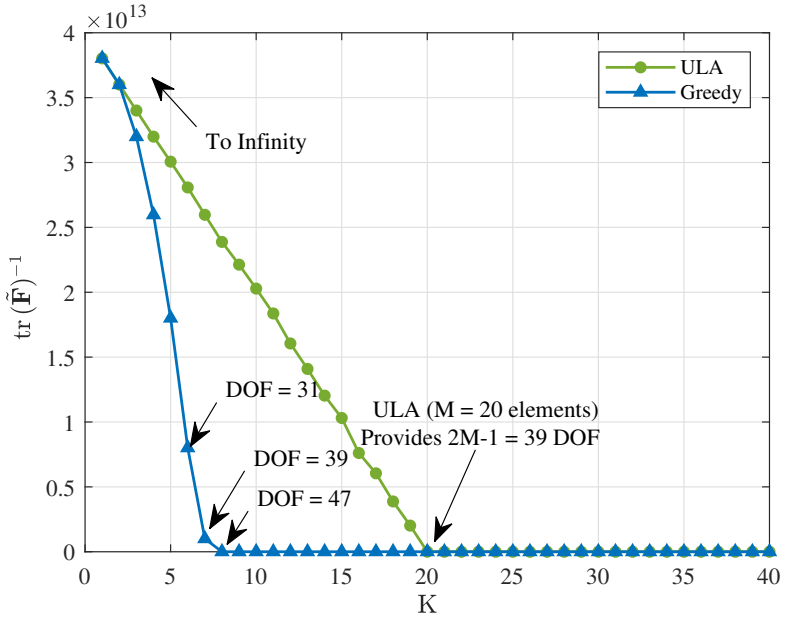

Figure 4.6: Parameter identifiability analysis for the ULA and the Greedy algorithm (under scenario 1.1a).

When the number of selection K is low, the CRBs for both arrays explode to infinity. Each curve meets its turning point when the number of DOF equals the number of sources $N = 39$. When the DOF exceeds N, the CRB immediately becomes finite and considerably small.

As a conclusion, the identifiability of the problem is mainly dictated by the invertibility of $\mathbf{F}_{\sigma_s\sigma_s}$, essentially being determined by the difference co-array' DOF vs. the number of sources. The influence of $\mathbf{F}_{gg}$ on the identifiability is not clearly visible,

since it is always full-rank. All of these results agree with the theory demonstrated previously.

4.2.3 Optimal array geometry for imaging

The recovery of the signal's second-order statistics - the celestial source powers $\boldsymbol{\sigma}_s$ in our case - from the observed data is frequently termed as covariance sensing. A study [27] introduces the utilization of the sparse rulers as optimal sparse samplers (or array designs) for retrieving the second-order statistics. This motivates us to compare our selection results with such array designs.

It is found that the array selected by exhaustive search in scenario 1.1a is identical to the minimal sparse ruler. Figure 4.7 compares those two selection schemes under some particular settings of $\binom{M}{K}$ combinations when minimal sparse rulers are available. This confirmed that sparse rulers are optimal array geometries for pure image estimations (i.e. with no nuisance parameters).

As mentioned in [27], earlier works of minimal sparse ruler designs are mostly based on criteria related to identifiability and the associated compression rates. So this result may help to prove the optimality of sparse rulers from a CRB perspective.

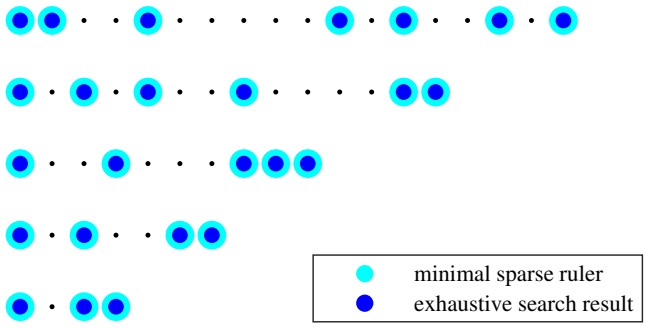

Figure 4.7: The scenario 1.1a exhaustive search result compared to minimal sparse ruler arrays.

4.3 Scenario 2

4.3.1 Selection results

The scenario 2 selection results are shown in figure 4.8. We emphasize again that in this scenario we are interested in $\mathbf{C}_{gg}$, hence the objective is

$$f(\mathbf{w}; \mathbb{E}[\boldsymbol{\theta}]) = \text{tr}\left[\mathbf{C}_{gg}(\mathbf{w}; \mathbb{E}[\boldsymbol{\theta}])\right] \approx \text{tr}\left[(\tilde{\mathbf{F}}'(\mathbf{w}; \mathbb{E}[\boldsymbol{\theta}]) + \epsilon\mathbf{I})^{-1}\right]. \tag{4.10}$$

Overall, the greedy and convex (rand.) arrays provide the best performances in most cases, staying close to or even attaining the exhaustive search lower bound. Although there are some exception, e.g. when $K = 3$ in scenario 2.2a and 2.2b, in which they perform worse than the ULA, their associated objective values soon fall back rapidly with the increase of K and become better than the ULA results again. The greedy algorithm slightly outperforms the convex-based approach in almost all the cases.

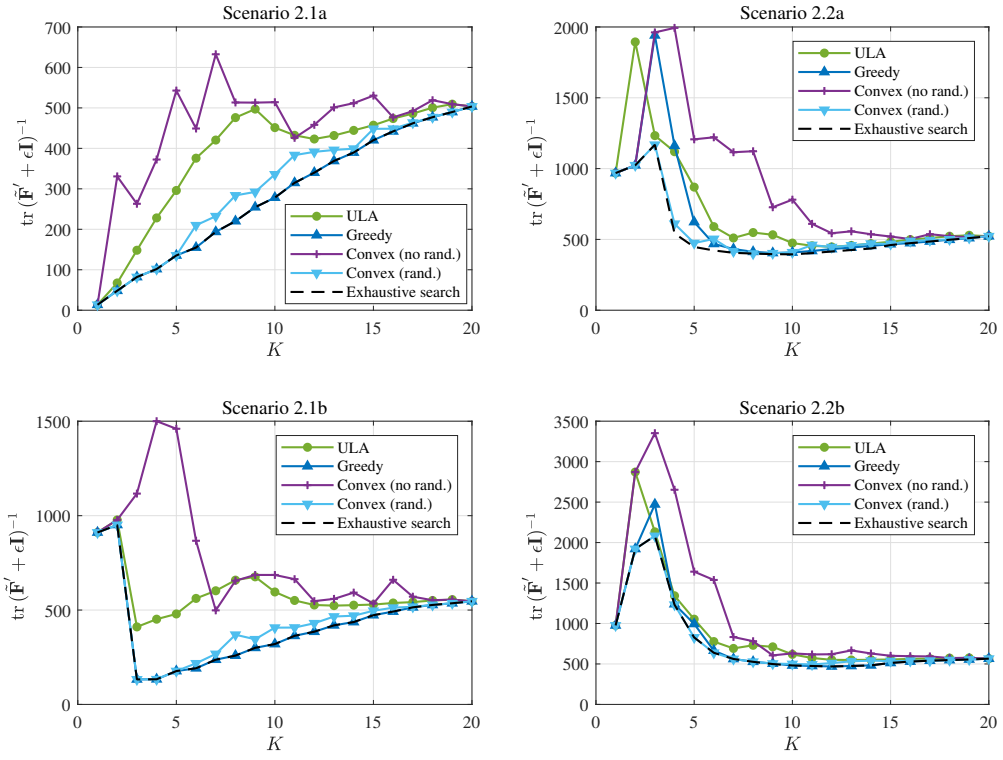

Figure 4.8: Change of CRB with increasing K (Scenario 2)

In scenario 2.1a, the exhaustive search provides a monotonically increased objective function w.r.t. K, which fits the intuition that the more sensors get selected, the more gain estimation errors are summed up. In the other sub-scenarios, the exhaustive search's optimization costs first surge to high magnitudes, then fall back and increase monotonically as well. The initial surges might be consequences of the lack of identifi-

ability. For example in scenario 2.1b, when K is small (say $K = 1$), the arrays cannot provide sufficient DOF to identify all the 4 calibration sources' powers.

4.3.2 Optimal array geometry for gain estimation

Figure 4.9 shows the scenario 2.1a greedy selection result, as well as the geometric phase delays of the signals from each calibration source to all the candidate locations, i.e. the angle of the array manifold vector $\angle \mathbf{a}'(\alpha_i')$, $i = 2, 3, 4$, where α_i' is the DOA of the i-th calibration source. The phases are wrapped into the $[-\pi, \pi]$ interval. The reason not to plot $\angle \mathbf{a}'(\alpha_1')$ is that the first source is located at the zenith (see figure 4.1), thus all the geometric delays are zero.

By comparison, it is clear that the selected positions are the common zero-crossing points of the geometric delays. To be more precise, the optimal array to estimate the gain is an array with receiver elements that experience coherent phase delays from all the sources.

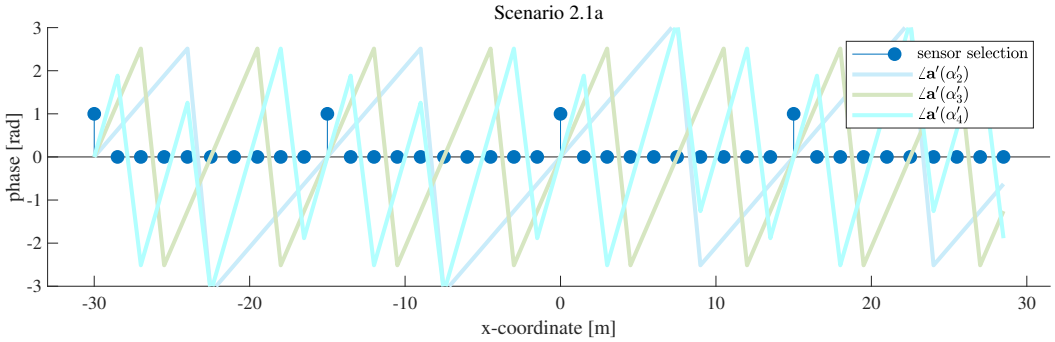

Figure 4.9: Optimal array for gain estimation.

Such a phenomenon coincides with physical intuitions:

- For magnitude estimation: At those locations, signals are added coherently due to the same phase delay, which results in the highest SNR and hence better magnitude estimation.
- For phase estimation, at each sensor, phase deviations in the received data all come from the fluctuating complex gain. There is no contribution from the geometric delay, and therefore the phase estimation can be easier.

Therefore, no matter from a magnitude's or a phase's point of view, it is desirable to distribute the sensors at those locations.

4.4 Scenario 3

The scenario 3 selection results are shown in figure 4.10, which is similar to the results in scenario 1. This makes sense as they both focus on imaging. It is observed that the greedy selection gives the best results, being the closest to the exhaustive search lower bound. The convex SDR with randomization also provides good sub-optimal outcomes, which does not happen in scenario 1.

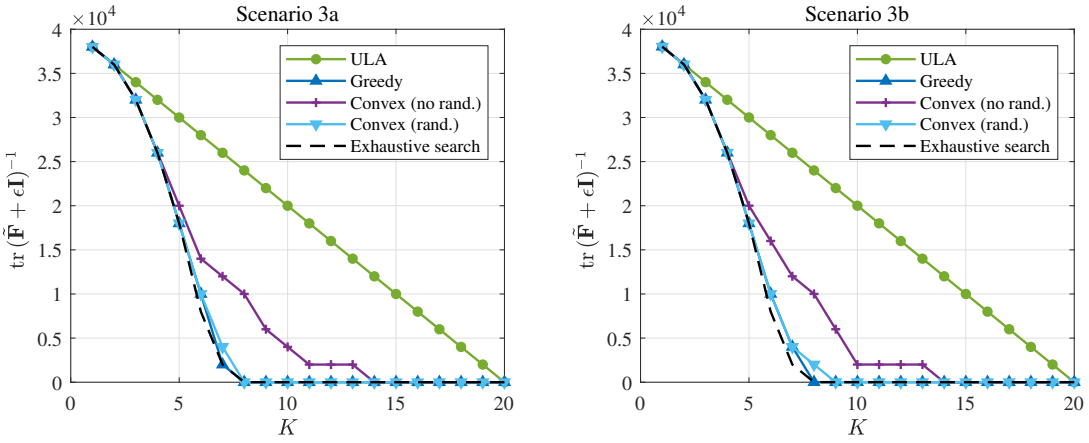

Figure 4.10: Change of CRB with increasing K (Scenario 3)

In order to demonstrate the effect of taking nuisance parameters into account during the selection process, figure 4.11 compares some exhaustive search outcomes for scenario 1.1a and 3b when $K = 2, 4, 6$ and 8 respectively. It can be seen that the scenario 3b results do differ from that of scenario 1.1a.

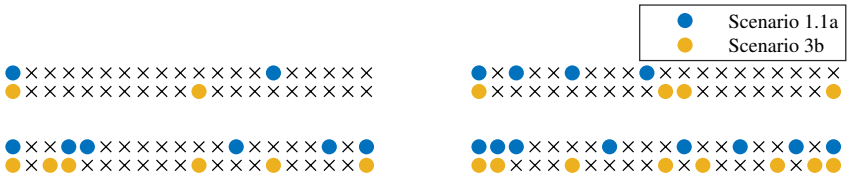

Figure 4.11: Comparison of the exhaustive search results for scenario 1.1a and 3b ($K = 2, 4, 6$ and 8)

.

It is also worth mentioning that both in scenario 1 and 3 when imaging is the main estimation task, the outermost sensors are more likely to be selected. One of the intuition is that the outermost sensors are able to provide larger baselines which can increase angular resolution of the observations.

4.5 Conclusion

In conclusion, the greedy algorithm offers a good sub-optimal solution to this combinatorial optimization problem in almost all the considered cases. Convex optimization

does not perform well in scenario 1, but provides reasonable selection outcomes in scenario 2 and 3 (although they are still sightly worse compared to that of the greedy algorithm). Furthermore, the convex approach has a relatively high computational complexity, which results in a dramatically increased execution time as the problem size scales up. Therefore, we conclude that the greedy algorithm is more suitable for the derived optimization problem, and it is chosen for the simulations in the next chapter.

5 Simulation

In order to test the performance of the resulting array designs, in this section, two types of simulations are conducted, which are designed to fulfill different purposes:

- **The statistical behavior tests**
  The standard CRB for the coavriance model - the Bangs' formula - has already been derived rigorously. However in our case, a number of modifications was introduced. We incorporated the sensor selection and nuisance parameters into the closed-form expression. And for scenario 3, the CRB expression is even more complex as the data vectors are stacked. Therefore, it is critical to verify if the derived CRBs are reliable.

  A straightforward way to check the CRBs is through Monte-Carlo simulations. Ideally, this should be accomplished by MVU estimators since their outputs attain the CRB [15]. In practice, as MVUs are apparently not available, asymptotically efficient algorithms are used instead, and we verify if the overall variance converges to the theoretical CRBs on a large-sample basis.

  Moreover, as will be demonstrated soon, the estimators employ some approximations/simplifications, e.g. assuming the covariance $\mathbf{R} \approx \mathbf{I}$. Therefore, it is also beneficial to see how much error would those modifications introduce.

- **The general performances tests**
  Once the CRBs and the estimators are verified, we proceed to some general testing in which the setups are more realistic. For example, the amount of data are moderate, and the imaging system is underdetermined (i.e. the number of sources $N >$ the number of selected sensors K). This should give us an idea of whether the CRB-based array designs can generally lead to good performance as well.

The remainder of the chapter is organized as follows. Section 5.1 provides various aspects of the simulation setup. Section 5.2 introduces the estimation methods used throughout the tests. Section 5.3 presents the statistical behavior tests. Section 5.4 demonstrates the general performances of the selected arrays. Section 5.5 shows the gain calibration convergence speed for the considered array designs.

5.1 Simulation setup

The arrangement of the simulations is shown in figure 5.1. In the selection phase, the algorithms utilize the given scenario setup information to compute the optimal selection vector $\mathbf{w}^*$. As already mentioned, $\mathbb{E}[\boldsymbol{\theta}]$ is substituted to decouple the objective function and the true $\boldsymbol{\theta}$.

In the simulation phase, the imaging observations $\mathbf{X}$ and the calibration observations $\mathbf{X}'$ are generated according to the realizations (i.e. the true values) of $\boldsymbol{\theta}$ rather than the expectation $\mathbb{E}[\boldsymbol{\theta}]$. It is worth to highlight that the imaging system has no knowledge of the selection process apart from the selection vector $\mathbf{w}^*$. The algorithms only use the data that is associated with the *selected* sensors and perform estimations accordingly.

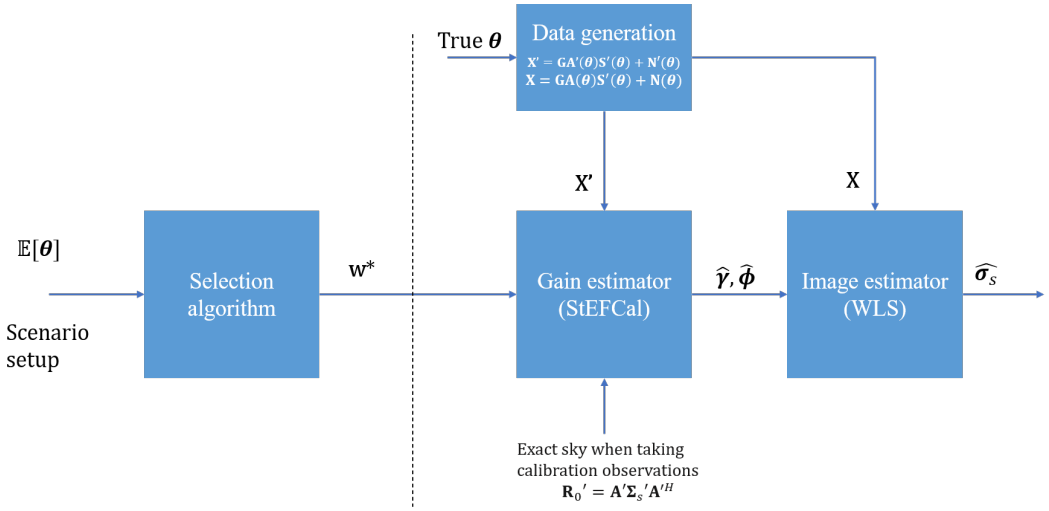

Figure 5.1: Illustration of the simulation procedure

The estimation is performed in a sequential manner, in contrast to the standard iterative procedure adopted by most real-world RA imaging systems. This is due to the consideration that for the statistical behavior tests the Monte-Carlo simulations have to be executed extensively (for 10^4 or even 10^5 times), which cannot be accomplished by the iterative scheme within limited time. As demonstrated in figure 1.1, in an iterative procedure the gain estimation relies on a repeatedly updated sky model to refine the gain estimates. In order to implement a sequential procedure, we break such an iterative process by supplying the gain estimator with the true sky model $\mathbf{R}_0$. Apparently such a simplification will make the results to be over optimistic compared to the CRB, since the $\mathbf{R}_0$ is provided to the estimator as oracle information. However, as will be shown later, the difference is negligible.

The true parameter $\boldsymbol{\theta}$ is drawn from a distribution detailed in table 5.1. The amplitude $\boldsymbol{\gamma}$ and the phase $\boldsymbol{\phi}$ of the gain are assumed to be normally distributed.

For the amplitude, we assume the standard deviation $\sigma_\gamma = \frac{1}{6}$ such that 99.7% of the samples stay within the range $[0.5, 1.5]$. This assumption is inline with the true parameter distribution in LOFAR, which is equipped with a robust fault identification mechanism that rejects data from any receiver having a gain outside $[0.5, 1.5]$ [9]. For

the phase, we assume $\sigma_\phi = \pi/3$ such that nearly all the samples are concentrated within the full $[-\pi, \pi]$ interval.

The noise powers are assumed to be deterministic and normalized to unity, hence the SNRs are controlled by setting the source powers to different levels. The imaging source powers $\boldsymbol{\sigma}_s$ are assumed to be uniformly distributed in dB scale from 10^{-4} to 10^{-2}, whereas the calibration source powers are uniformly distributed in dB scale from 10^{-2} to 10^{-1}. Hence, notice that the source powers are much smaller than the noise power.

Variable	Distribution	Simulation setting
Gain amplitude $\boldsymbol{\gamma}$	$\mathcal{N}(\boldsymbol{\mu}_\gamma, \sigma_\gamma^2\mathbf{I})$	$\boldsymbol{\mu}_\gamma = \mathbf{1}$, $\sigma_\gamma = 1/6$
Gain phase $\boldsymbol{\phi}$	$\mathcal{N}(\boldsymbol{\mu}_\phi, \sigma_\phi^2\mathbf{I})$	$\boldsymbol{\mu}_\phi = \mathbf{0}$, $\sigma_\phi = \pi/3$ [deg]
Imaging source power $\boldsymbol{\sigma}_s$	Uniform in dB scale, $10^{\mathcal{U}[a,b]/10}$	$a = -40, b = -20$ [dB]
Imaging noise power $\boldsymbol{\sigma}_n$	deterministic	$\boldsymbol{\sigma}_n = 1$
Calibration source power $\boldsymbol{\sigma}'_s$	Uniform in dB scale, $10^{\mathcal{U}[a,b]/10}$	$a = -20, b = -10$ [dB]
Calibration noise power $\boldsymbol{\sigma}'_n$	deterministic	$\boldsymbol{\sigma}'_n = 1$
Imaging source signal $\mathbf{s}$	$\mathcal{CN}(\mathbf{0}, \mathrm{diag}(\boldsymbol{\sigma}_s))$	$\boldsymbol{\sigma}_s$ above
Imaging noise $\mathbf{n}$	$\mathcal{CN}(\mathbf{0}, \mathrm{diag}(\boldsymbol{\sigma}_n))$	$\boldsymbol{\sigma}_n$ above
Calibration source signal $\mathbf{s}'$	$\mathcal{CN}(\mathbf{0}, \mathrm{diag}(\boldsymbol{\sigma}'_s))$	$\boldsymbol{\sigma}'_s$ above
Calibration noise $\mathbf{n}'$	$\mathcal{CN}(\mathbf{0}, \mathrm{diag}(\boldsymbol{\sigma}'_n))$	$\boldsymbol{\sigma}'_n$ above

Table 5.1: Default distributions used in simulations

5.2 Estimation methods

To fulfil the simulation purposes, a natural choice of the estimator would be the ML estimator since it is asymptotically efficient. The ML formulation can be obtained by minimizing the associated log likelihood function related to our data model [28], i.e.

$$\hat{\boldsymbol{\theta}} = \underset{\boldsymbol{\theta}}{\operatorname{argmin}} \ \ln|\mathbf{R}(\boldsymbol{\theta})| + \operatorname{tr}\left(\mathbf{R}(\boldsymbol{\theta})^{-1}\hat{\mathbf{R}}\right) \tag{5.1}$$

However, such a problem cannot be in easily solved in closed-form. A previous study [8] proposed an alternative by using the weighted least squares (WLS) covariance matching technique. The merit of such an approach is that the solution it is equivalent to the ML solution on large sample basis hence is also asymptotically efficient. The WLS formulation is given as

$$\hat{\boldsymbol{\theta}} = \underset{\boldsymbol{\theta}}{\operatorname{argmin}} \ \|\boldsymbol{\Sigma}_c^{-1/2}\left(\hat{\mathbf{r}} - \mathbf{r}\right)\|_2^2 \tag{5.2}$$

$$= \underset{\boldsymbol{\theta}}{\operatorname{argmin}} \ \left(\hat{\mathbf{r}} - \mathbf{r}\right)^H \boldsymbol{\Sigma}_c^{-1}\left(\hat{\mathbf{r}} - \mathbf{r}\right) \tag{5.3}$$

where $\boldsymbol{\Sigma}_c$ is the weighting covariance matrix. It is suggested in [28] that by setting $\boldsymbol{\Sigma}_c$ to the covariance of $\hat{\mathbf{r}}$, namely $\boldsymbol{\Sigma} = \overline{\mathbf{R}} \otimes \mathbf{R}$, the estimates will become a large-sample approximation of the ML solution. Hence, the covariance matched solution is given as

$$\hat{\boldsymbol{\theta}} = \underset{\boldsymbol{\theta}}{\operatorname{argmin}} \ \|\mathbf{W}_c\left(\hat{\mathbf{r}} - \mathbf{r}\right)\|_2^2 \tag{5.4}$$

where the optimal weighting matrix $\mathbf{W}_c = \boldsymbol{\Sigma}^{-1/2} = \overline{\mathbf{R}}^{-1/2} \otimes \mathbf{R}^{-1/2}$. By using the property [1, (2)], we arrive at another equivalent formulation which is in $\mathbf{R}$,

$$\hat{\boldsymbol{\theta}} = \underset{\boldsymbol{\theta}}{\operatorname{argmin}} \ \|\mathbf{W}\left(\hat{\mathbf{R}} - \mathbf{R}\right)\mathbf{W}\|_F^2. \tag{5.5}$$

Although by using the WLS approach the formulation has been simplified from (5.3) greatly, it is still too complicated for all the parameters in $\boldsymbol{\theta}$ to be solved as a whole. From the data model (1.7), it is easy to notice that there are two distinct groups of parameters:

- **Complex gain**. which scales the rows of the array manifold $\mathbf{A}$.
- **Source and noise powers**. The model is linear in $\boldsymbol{\sigma}_s$ and $\boldsymbol{\sigma}_n$.

which leads to 2 different WLS sub-problems for which the solutions are well-studied. Therefore, a viable solution is to leverage the alternating direction implicit (ADI) principle which iteratively alternates between these two sub-problems until their solutions converge [8]. In the next two subsections, we will introduce the methods to efficiently solve the sub-problems.

5.2.1 Gain estimation method

In this subsection, we introduce an efficient WLS-based iterative gain calibration algorithm, namely, the StEFCal algorithm [29]. The calibration problem involves the retrieval of the directional-independent gain $\mathbf{g}$ from the calibration sample covariance $\hat{\mathbf{R}}' = \frac{1}{P}\mathbf{X}'\mathbf{X}'^H$, with the uncertainty of the calibration sources and noise powers $\boldsymbol{\sigma}'_s$ and $\boldsymbol{\sigma}'_n$. Therefore, the related WLS minimization problem is given as

$$\{\mathbf{g}, \hat{\boldsymbol{\sigma}'_s}, \hat{\boldsymbol{\sigma}'_n}\} = \underset{\mathbf{g},\boldsymbol{\sigma}'_s,\boldsymbol{\sigma}'_n}{\operatorname{argmin}} \|\mathbf{W}^H(\hat{\mathbf{R}}' - \mathbf{R}')\mathbf{W}\|_F^2 \tag{5.6}$$

$$= \underset{\mathbf{g},\boldsymbol{\sigma}'_s,\boldsymbol{\sigma}'_n}{\operatorname{argmin}} \|\mathbf{W}^H[\hat{\mathbf{R}}' - (\mathbf{G}\mathbf{R}'_0\mathbf{G}^H + \boldsymbol{\Sigma}'_n)]\mathbf{W}\|_F^2 \tag{5.7}$$

where $\mathbf{R}'_0 = \mathbf{A}'\boldsymbol{\Sigma}'_s\mathbf{A}'^H$, and the weighting is configured as $\mathbf{W} = \mathbf{R}'^{-\frac{1}{2}}$ to achiveve the desired statistical performance as mentioned previously.

To make the problem easier to solve, two simplifications were adopted in [29]. First, it is assumed that $\mathbf{R}' \approx \boldsymbol{\Sigma}'_n = \sigma_n\mathbf{I}$, as the astronomical source powers are usually much lower than the noise, and the noise powers are usually homogeneous. Also, the diagonal entries of $\mathbf{R}'$ and $\mathbf{R}'_0$ are set to zero, as only the diagonal entries of the sample covariance $\hat{\mathbf{R}}'$ are largely contaminated by the noise. By doing so, the problem can be reduced to

$$\mathbf{g} = \underset{\mathbf{g}}{\operatorname{argmin}} \|\hat{\mathbf{R}}' - \mathbf{G}\mathbf{R}'_0\mathbf{G}^H\|_F^2. \tag{5.8}$$

Such a simplification might seem to conflict with our data model since we only assume the noise to be white, i.e. $\boldsymbol{\Sigma}'_n = \operatorname{diag}(\boldsymbol{\sigma}_n)$, but not necessarily having the same power. However, it is further demonstrated in [29] that violating the homogeneous noise power assumption only leads to a small increase in estimation MSE. To ensure such an argument still holds under the project's context, extensive tests of the algorithm's statistical performance were conducted and will be presented in the next section.

In order to efficiently solve such a problem, the ADI principle is applied again. It turns out that the update equation of $\mathbf{G}$ and $\mathbf{G}^H$ are identical - for the k-th iteration, the ADI update of the m-th receiver gain g_m is [29]

$$g_m^{[k]} = \frac{\hat{\mathbf{R}}'_{:,m} \cdot \mathbf{Z}^{[k-1]}_{:,m}}{\|\mathbf{Z}^{[k-1]}_{:,m}\|_2^2} \tag{5.9}$$

where $\mathbf{Z}^{[k]} = \mathbf{G}^{[k]}\mathbf{R}_0$. And by averaging every even-iteration solution with its previous odd iteration one, the convergence speed and stability can be improved, which leads to the StEFCal algorithm [29, Algorithm 1].

5.2.2 Source power estimation method

As mentioned in [14], the WLS imaging problem can be posed as

$$\{\hat{\boldsymbol{\sigma}_s}, \hat{\boldsymbol{\sigma}_n}\} = \underset{\boldsymbol{\sigma}_s,\boldsymbol{\sigma}_n}{\operatorname{argmin}} \|\mathbf{W}_c(\hat{\mathbf{r}} - \mathbf{H}_s\boldsymbol{\sigma}_s - \mathbf{H}_n\boldsymbol{\sigma}_n)\|_F^2 \tag{5.10}$$

where $\mathbf{H}_s = \overline{\mathbf{GA}} \circ \mathbf{GA}$ and $\mathbf{H}_n = \mathbf{I} \circ \mathbf{I}$, and $\mathbf{W}_c$ is the weighting matrix as mentioned.

The closed-form solution for (5.10) is given in [14] as

$$\hat{\boldsymbol{\sigma}_s} = (\tilde{\mathbf{W}}_c \mathbf{H}_s)^{\dagger} \tilde{\mathbf{W}}_c \hat{\mathbf{r}} \tag{5.11}$$

where the modified weighting $\tilde{\mathbf{W}}_c = \left[\mathbf{I} - (\mathbf{W}_c \mathbf{H}_n)(\mathbf{W}_c \mathbf{H}_n)^{\dagger}\right] \mathbf{W}_c$ removes the contribution of noise.

5.3 Statistical behaviors

In the section, the statistical performances of the resulting arrays are tested through the aforementioned estimation algorithms. First, the tests are applied to the StEFCal algorithm and the WLS image estimator individually. This is to isolate them such that they are not affected by each other. Then, the joint estimation is evaluated.

The tests are conducted for two arrays designs:

- **ULA**. Similar to the previous chapter, we employ the ULA as a comparison.
- **Greedy**. The sparse arrays obtained by solving the greedy algorithm for the respective scenarios assumed in each experiment.

To give a fair comparison, we keep the number of selected elements the same for both arrays. In fact, throughout the three experiments in this section, we always select $K = 10$ sensors from $M = 100$ half-wavelength spaced uniformly distributed candidate locations. The geometry is the same as in figure 4.1 but with more candidate locations.

Since the Nyquist sampling criterion has to be fulfilled, the ULA design can only be 10 candidates being consecutively selected. Therefore, ULA always has a much smaller aperture (spatial extent) than the arrays sparsely selected by the greedy algorithm.

5.3.1 Gain estimation

5.3.1.1 Experiment design

In this experiment we intend to test the gain calibration part solely. The true sky model is supplied to the StEFCal algorithm for the discussed reason. This implicitly assumes scenario 2.1b. And the greedy algorithm obtains the sparse array by solving the scenario 2.1b problem.

Because a normalization step is invoked for the gain estimates, for the sake of clarity, here we explicitly state the simulation procedure:

- The calibration signal $\mathbf{S}'$ and noise $\mathbf{N}'$ are generated according to the distributions listed in table 5.1, and subsequently the sample covariance $\hat{\mathbf{R}}'$ is generated by $\hat{\mathbf{R}}' = \frac{1}{P}\mathbf{X}'\mathbf{X}'^{H}$.
- The StEFCal algorithm is executed to obtain the gain estimate $\hat{\mathbf{g}}$.
- The phase of $\hat{\mathbf{g}}$ is normalized by makeing sure the gain of the first element has unity magnitude and zero phase.

5.3.1.2 Example estimates

An example gain estimate is shown in figure 5.2, in which $P = 10^4$ samples of $\mathbf{x}'$ are used to calculate the estimated data covariance $\hat{\mathbf{R}}'$ during data generation. It can be seen that the estimates all fall in the close vicinity of the true gains, which indicates the estimations to be successful. Note that the true gains in the ULA and greedy cases are not the same, which is due to the fact that different sensors are selected for each array.

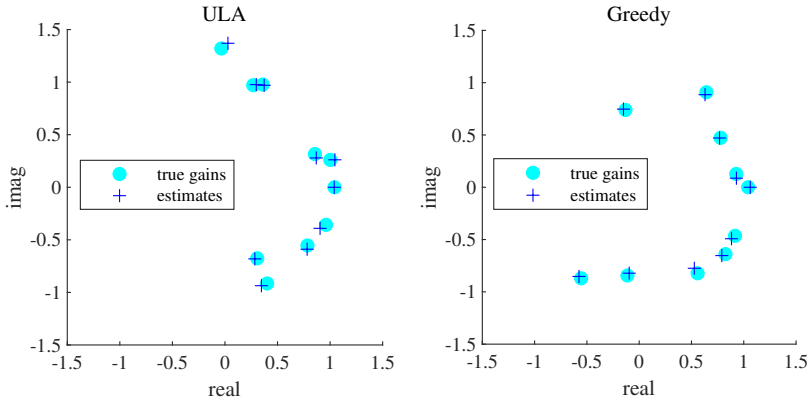

Figure 5.2: Example gain estimates by the StEFCal algorithm

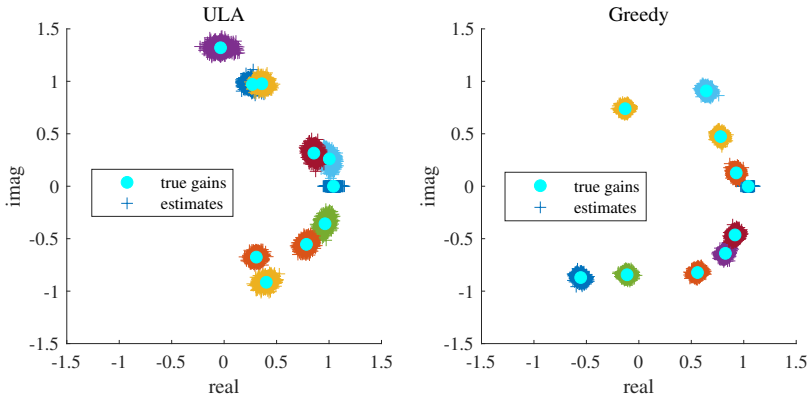

Figure 5.3: The distribution of the gain estimates following 10^4 Monte-Carlo runs

To showcase the statistical performance provided by the two arrays, the above experiment was run for 10^4 times and the resulting estimates are presented in figure 5.3. It can easily be observed that the greedy estimates (the clusters centered around the true gains) are more compact than the ULA ones. Also observe that the estimates located around $(1, 0)$ in the complex plane stay on the real axis. This is due to the phase normalization imposed such that the first element always has zero phase.

5.3.1.3 Statistical performance

The quantitative assessment of the statistical behavior can be done by evaluating the estimation bias and MSE achieved through Monte-Carlo simulation. To show this, an additional 10^5 experiments are performed. The results are shown in figure 5.4, and we have the following observations:

- **Bias**. Compared to the square roots of the CRB and the MSE, the biases are insignificant. This suggests that the estimates are unbiased.
- **MSE**. Since the estimation is more or less unbiased, the MSE approximates the variance. It can be seen that the MSEs are all close to their respective CRBs, and it is clear that greedy selection does yield a better array than a ULA with the same number of sensor elements.

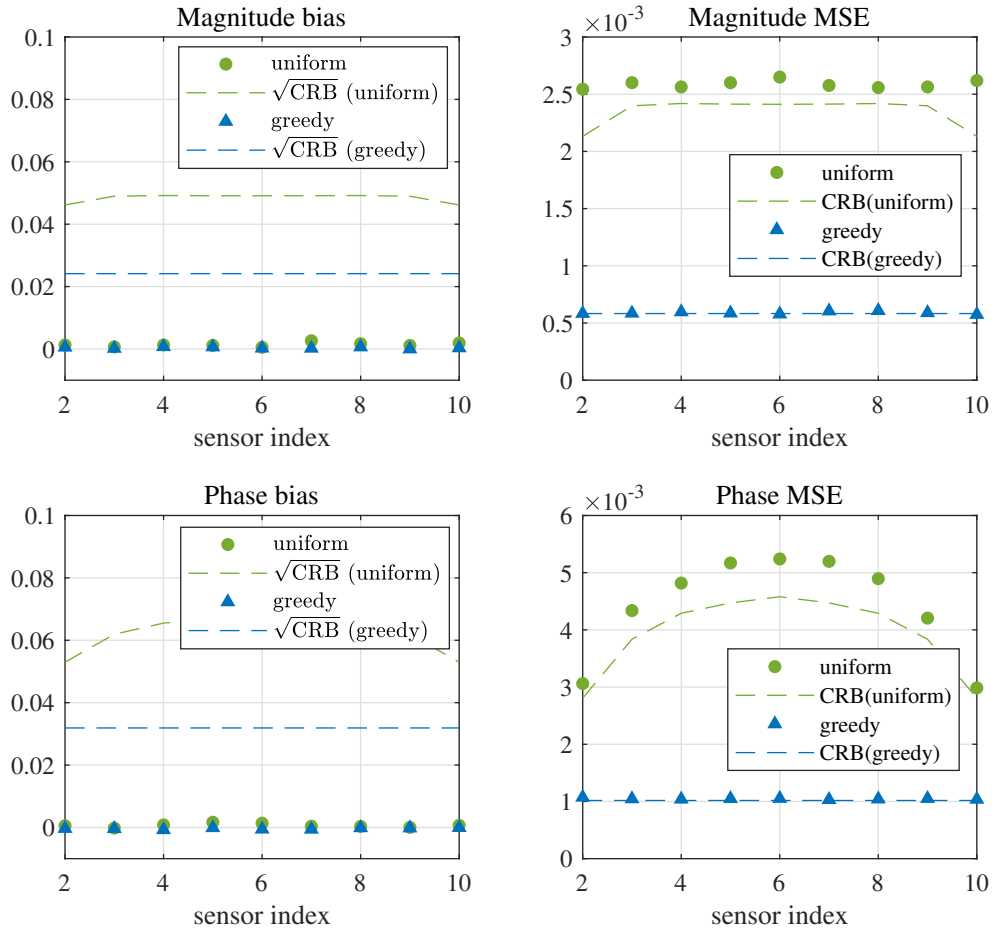

Figure 5.4: Statistical performance of the gain estimation. A total of $N_{mc} = 10^5$ Monte-Carlo simulations are conducted for this experiment.

Finally, we perform a series of Monte-Carlo simulations under an increased P to demonstrate how it influences the statistical performance. Figure 5.5 shows that the MSEs of the estimates converge to their respective CRBs over large samples (when exceeding $P = 10^4$).

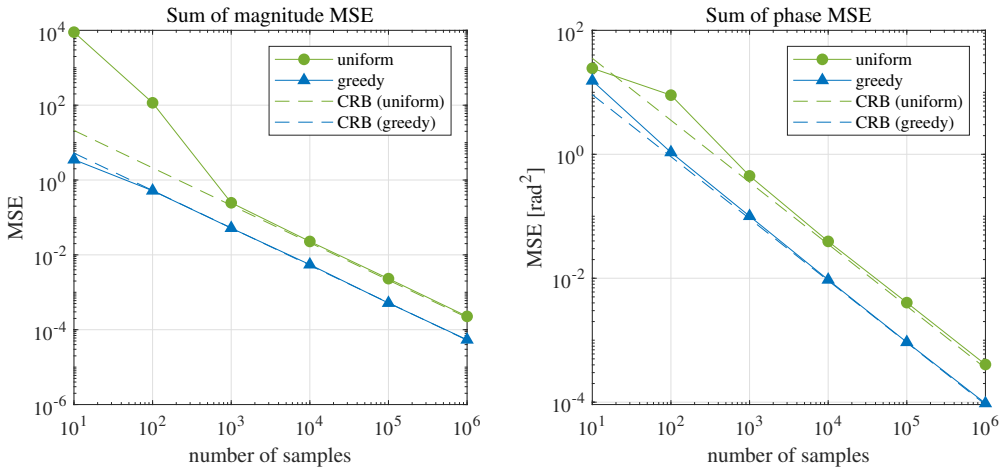

Figure 5.5: The sum of gain estimation MSE as a function of the number of samples P.

5.3.2 Image estimation

5.3.2.1 Experiment design

This time we switch to the imaging part. The true gains are supplied to the WLS algorithm during tests, and scenario 1.1b is assumed throughout the experiment, for which the greedy algorithm is tailored to obtain the sparse array.

Different from the normal imaging scenarios, this experiment is conducted under an overdetermined geometry, in which the number of imaging sources $N = 9$ is less than the number of selected sensors $K = 10$. Such a configuration ensures the identifiability of the parameters so that the noise does not blow up in the WLS solutions. This is important for the statistical performance tests, since if the estimator fails to reconstruct the image, the MSE as well as the bias are not meaningful and hence cannot be compared with the CRB.

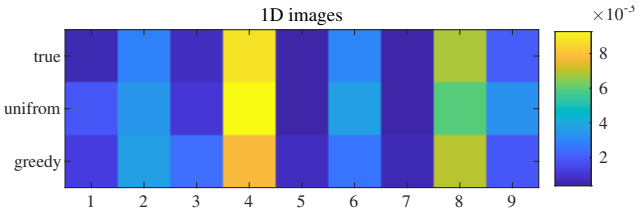

Figure 5.6: Example image estimation results.

5.3.2.2 Example estimates

An example estimate is shown in figure 5.6, for which $P = 10^4$ samples are used. Both arrays provide good reconstructions, and the noise does not blow up.

5.3.2.3 Statistical performances

Figure 5.7 displays the overall statistical imaging performances for 10^5 Monte-Carlo simulations. We observe similar outcomes as the previous simulation. The biases of the source power estimates are considerably small compared to the square root of the CRB, and their MSEs are all above but close to the CRBs. This implies that the estimation is asymptotically consistent. Such an argument is further supported by figure 5.8, which plots the sum of the MSEs as a function of the number of samples P.

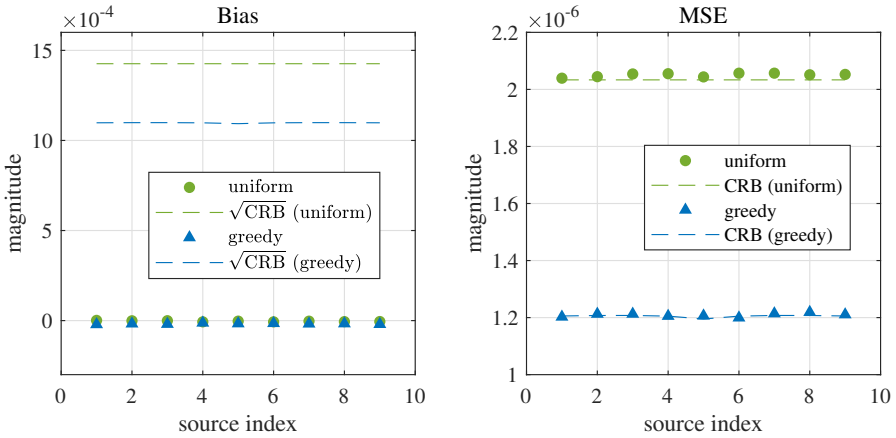

Figure 5.7: Statistical performance of the image estimation. A total of $N_{mc} = 10^5$ Monte-Carlo simulations are conducted for this experiment.

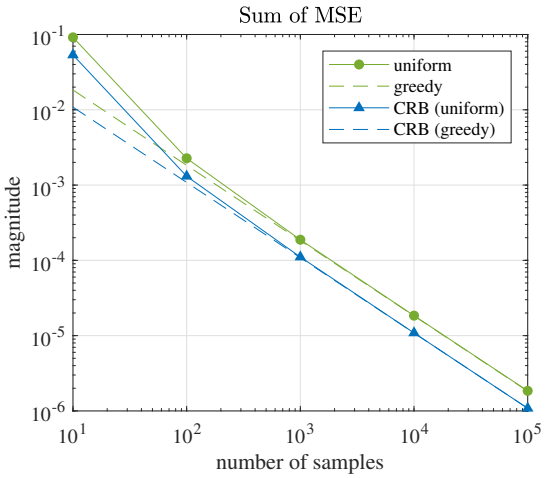

Figure 5.8: The sum of imaging MSE as a function of the number of samples P.

5.3.3 Joint imaging

Finally, we concatenate the gain and image estimators to form a sequential imaging pipeline as demonstrated earlier in Section 5.9. The desired estimation scenario is 3b, but due to the true sky model being supplied as an oracle, the experiment outcome could outperform the CRB. Thus, it is also one of the goals of conducting this test in order to see how large this difference is. As before, the sparse array is obtained by solving the scenario 3b problem in a greedy fashion.

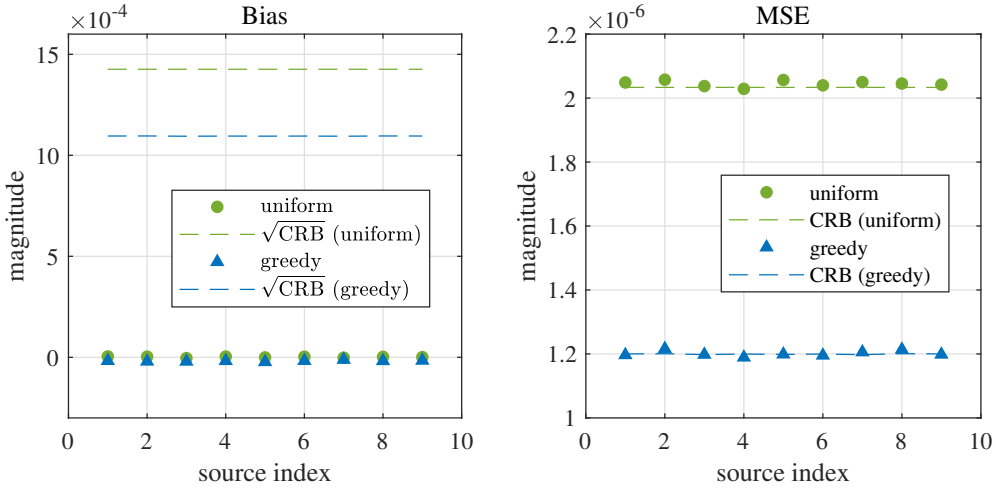

Figure 5.9: Statistical performance of the image estimation while the complex gains are considered as nuisance. A total of $N_{mc} = 10^5$ Monte-Carlo simulations are conducted for this experiment.

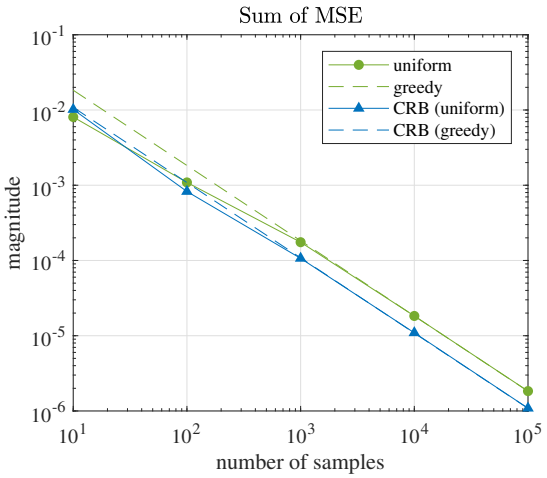

Figure 5.10: The sum of joint imaging MSE as a function of the number of samples P.

Similar tests are performed and the results are shown in figure 5.9 and figure 5.10 respectively. An interesting observation is that in figure 5.9, the MSEs of some of the brightness estimates are less than their corresponding CRBs. Also, notice that in figure

5.10 the sum of the MSEs approach the CBBs from below. This rarely happens for previous experiments where the CRB matches the actually scenario. We suspect that these phenomenons are consequences of utilizing the oracle $\mathbf{R}_0$. Nevertheless, when a large number of samples are used, the MSEs converge to the CRBs with nearly invisible deviations, which suggests that the effect of the oracle $\mathbf{R}_0$ is negligible, and the derived CRBs are reliable.

5.3.4 Conclusion

For all the above experiments, the outcomes are unbiased and the estimation MSEs converge to their respective CRBs over large samples. Recall that the estimator has no knowledge of the CRBs, but just performs estimation based on the selected synthetic data. Therefore, by witnessing the MSE and the CRB are asymptotically inline with each other, it is sufficient to conclude that the CRBs are correctly derived.

We observe that for all the three cases, the threshold for convergence is at $P = 10^4$. This is important for general performance tests in the next section, since it suggests how many samples are required for the imaging system to obtain a good performance.

A final remark is that the sequential procedure can be a good proxy for the iterative pipeline in the simulation. Under large sample conditions, we do not observe the estimation variance to deviate from the CRB, which implies that supplying the true sky model as oracle information only results in a negligible difference.

5.4 General performance

5.4.1 Experiment setup

In this section, as we would like to test the arrays' imaging performances under more realistic conditions, an underdetermined geometry is used, in which the number of imaging sources $N = 39$ is larger than the number of selection $K = 10$. As before, we emphasis that such a K is kept the same for all the tested arrays in order to give a fair comparison.

Since the main goal of the project is to investigate if incorporating the nuisance parameter $\mathbf{g}$ can result in a better array design, an additional array is assessed in the following simulation. The details of the three tested arrays are provided as follows:

- **ULA**, which serves as a comparison
- **G-CAL**, Greedy algorithm tailored for scenario 3b (i.e. the most comprehensive scenario).
- **G-NCAL**, Greedy algorithm with no calibration taken into account. This effectively corresponds to the greedy design for scenario 1.1b.

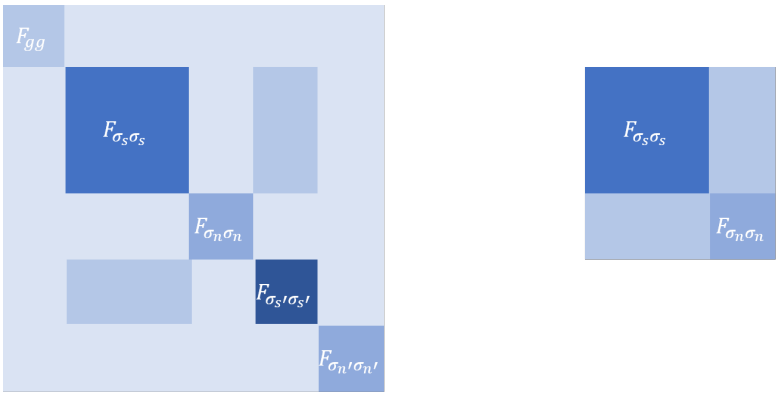

For G-CAL For G-NCAL

Figure 5.11: Constitution of the FIM for the compared greedy algorithms

To clarify the distinction between the two greedy arrays, their corresponding FIM used as the respective selection criterion is depicted in figure 5.11. The FIM for G-CAL comprises all the sub-blocks. In contrast, the FIM for G-NCAL does not contain the gain-related entries, which implies that no calibration-related process is assumed.

We utilize three performance measures to describe the quality of estimation:

- **MSE**.

$$\text{MSE} = \frac{1}{N}\|\hat{\boldsymbol{\sigma}}_s - \boldsymbol{\sigma}_s\|_2^2 \tag{5.12}$$

- **PSNR**. PSNR effectively normalizes the image estimate by its largest brightness value so that the performance measure is no longer affected by the variation of pixel intensities in the realizations. It also displays the results on log-scale, which is easier to interpret.

$$\text{PSNR} = 10 \log_{10} \left(\frac{\max \boldsymbol{\sigma}_s}{\text{MSE}} \right) \tag{5.13}$$

- **Normalized l_1-norm**.The l_1-norm describes how good the source structure is recovered, therefore can be used to detect the failed reconstruction. Likewise, we normalize it to make sure the performance measure is not affected by the magnitudes of particular realizations.

$$\text{Normalized } l_1\text{-norm} = \frac{\|\hat{\boldsymbol{\sigma}}_s - \boldsymbol{\sigma}_s\|_1}{\|\boldsymbol{\sigma}_s\|_1} \tag{5.14}$$

5.4.2 Example estimates

We first present two example estimation outcomes under different true source conditions:

- **Single point source**
  In the first case, we consider the simplest image – a single point source. The results are shown in figure 5.12 and table 5.2. Observe that the noise already blows up in the ULA estimates such that the output does not resemble the true image very well. In contrast, the two arrays selected by greedy algorithms are still able to provide reasonable reconstructions of the true image. Such a result is also reflected by the l_1-norm.

  The poor performance of the ULA can potentially be explained by the following reasons. Firstly, the relatively low DOF makes it hard for the ULA to retrieve the image in this underdetermined case. Also, the ULA has a much smaller spatial extent, thus provides the lowest resolution.

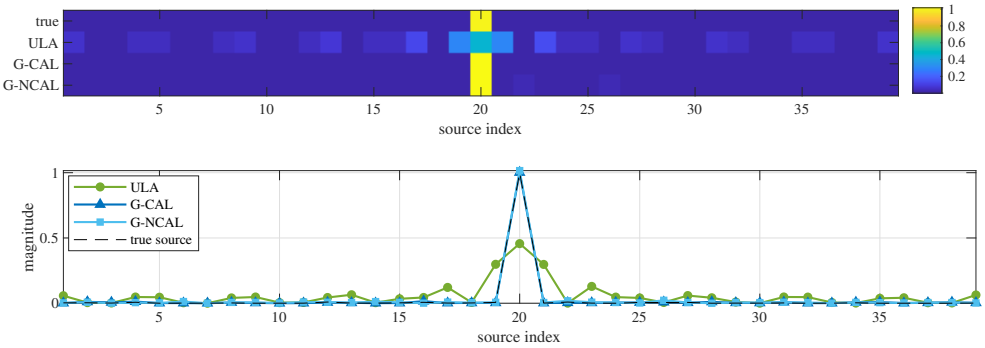

Figure 5.12: Example imaging result for a single point source ($P = 10^5$ samples are used)

Selection Scheme	MSE ($\times 10^{-5}$)	PSNR [dB]	Normalized l_1
ULA	1399.8*	51.584*	2.1387
G-CAL	1.1339	59.454	0.12391
G-NCAL	1.6998	57.696	0.19003

Table 5.2: Example imaging result for a single point source. *Note that since the ULA fails to recover the image, the associated MSE and PSNR is therefore meaningless. Here, they are shown just for qualitative comparison.

- **Random source**
  In the second case, we consider a more general sky condition, in which the true image is generated randomly without any assumed structure. By either inspecting the reconstruction result or comparing the l_1-norm, it is clear to see that the ULA fails to reconstruct the image. In comparison, both greedy arrays facilitate good image estimation. Not only the peaks (distinct point sources) but also the extended structure (e.g. around source index 29) are reconstructed.

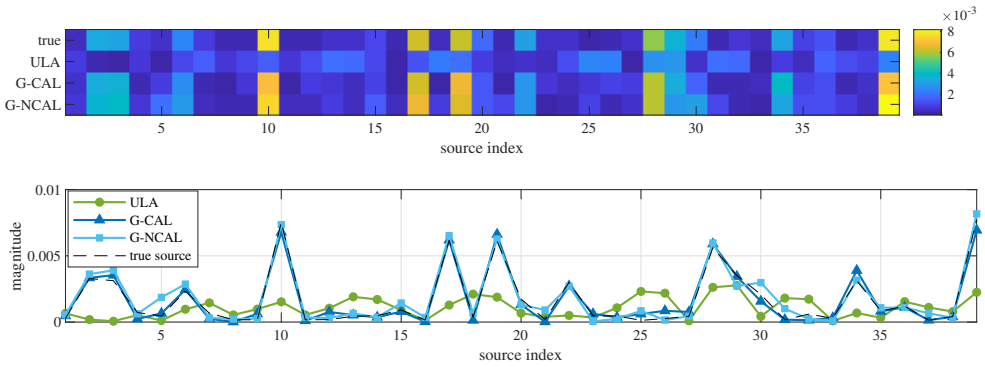

Figure 5.13: Example imaging result for a randomly generated true sky ($P = 10^5$ samples are used)

Selection Scheme	MSE ($\times 10^{-6}$)	PSNR [dB]	Normalized l_1
ULA	59.276*	52.271*	1.1409
G-CAL	1.3205	68.793	0.17136
G-NCAL	2.5433	65.946	0.23198

Table 5.3: Example imaging result for a randomly generated true sky. *The ULA's MSE and PSNR results are not reliable due to the discussed reason.

5.4.3 General performance

Previous examples are only for specific sets of parameters $\boldsymbol{\theta}$. To have a clear view of how the selected arrays behave generally, another 1000 Monte-Carlo runs are executed, each with a different $\boldsymbol{\theta}$ drawn from the distribution.

Since the MSE and PSNR are only meaningful when the estimation is successful, an additional step is applied which identifies the failed image reconstructions based on their l_1-norm. That is, the estimates resulting in an l_1-norm greater than a threshold T_{l1} are flagged as failed estimates. In this particular experiment, the threshold is set to 0.02.

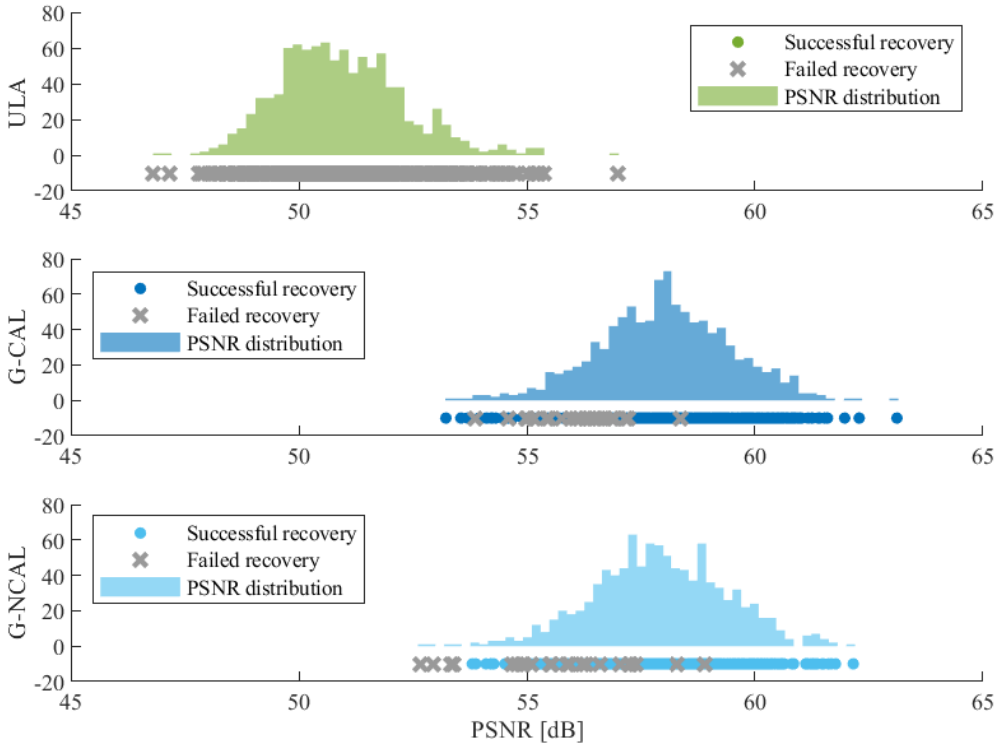

Figure 5.14: Distribution of the PSNR for 1000 Monte-Carlo simulations. For each run, $P = 10^4$ samples are used. The PSNRs of the ULA results are not meaningful. They are displayed here to serve as a qualitative comparison.

Selection Scheme	Optimization objective $f(\mathbf{w}; \mathbb{E}[\boldsymbol{\theta}])$	Number of failed cases	Avg. PSNR [dB] (incl. failed cases)	Avg. PSNR [dB] (excl. failed cases)
ULA	2.0003	1000	-	-
G-CAL	5.842×10^{-5}	27	58.0050	58.0593
G-NCAL	5.906×10^{-5}	22	57.9122	57.9604

Table 5.4: Summary of imaging result for 1000 Monte-Carlo simulations

The result is shown in table 5.4 whereas figure 5.14 presents the distribution of the image PSNRs. Note that since all ULA results are failed reconstructions, their PSNR values are no longer meaningful, hence this is not shown in the table. In comparison, the greedy designs only result in 27 and 22 failed estimations respectively, whereas the

vast majority successfully resembles the sources.

However, we do not observe a significant improvement when the calibration is taken into account. The distribution of PSNR does not show a clear performance difference between the two greedy arrays. And the average PSNR for G-CAL, either including or excluding the failed cases, is just slightly higher than that for G-NCAL.

5.5 Gain estimation convergence speed

As previously mentioned in Section 1.1, the iterative parameter refinement is a computationally-intensive process. Thus it would be a great help if any part of the process can be sped up. In this section, we focus on the gain estimation and compare the convergence speed of the StEFCal algorithm for the three considered array designs in the general performance test, namely the ULA, the G-CAL and the G-NCAL designs.

First, as an example, we show the convergence of the StEFCal algorithm for the synthetic calibration data $\mathbf{X}'$ generated according to $\mathbb{E}[\boldsymbol{\theta}]$. The calibration data covariance $\hat{\mathbf{R}}'$ is obtained by using 10^4 samples. The error for each StEFCal iteration is shown in figure 5.15, and we have the following observations:

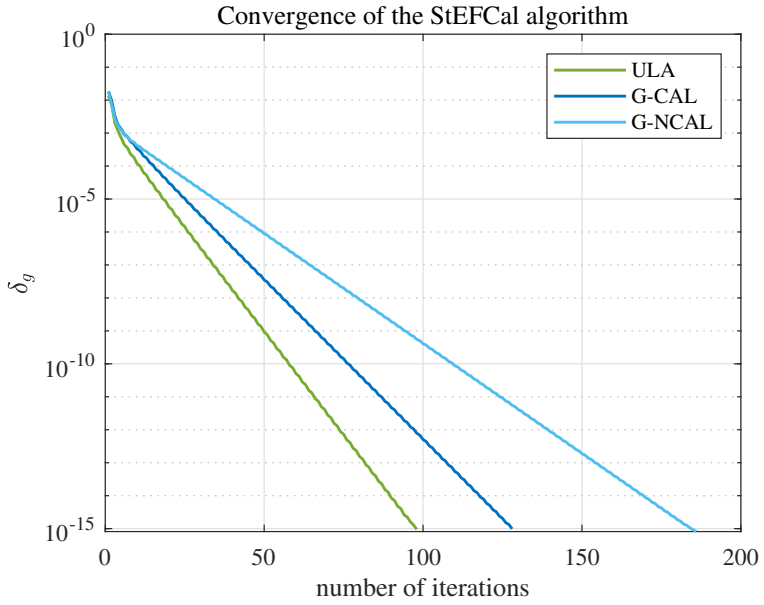

Figure 5.15: Comparison of the StEFCal convergence for ULA, G-CAL and G-NCAL. The expected parameter vector $\mathbb{E}[\boldsymbol{\theta}]$ is substituted as the true parameter vector for data generation. The convergence is assessed by evaluating $\delta_g = \|\mathbf{g}^{[k]} - \mathbf{g}^{[k-1]}\|_2 \,/\, \|\mathbf{g}^{[k]}\|_2$ with k being the iteration index.

- The ULA achieved the fastest convergence among the three compared arrays. A possible explanation is that the greedy arrays are designed specifically for imaging purposes. Therefore, their calibration capability might be sacrificed in exchange for much better imaging performances.

- A more interesting observation is that the G-CAL array facilitates a much faster convergence than the G-NCAL array. It takes 128 iterations for the G-CAL array to reach the StEFCAL stopping criterion, roughly 2/3 of that consumed by the G-NCAL design.

To test if those observations remain the same for difference system conditions, we conduct 1000 Monte-Carlo simulations. In each simulation a different $\boldsymbol{\theta}$ is drawn from the mentioned distribution. The result is displayed in a boxplot in figure 5.16, and similar behaviors are observed.

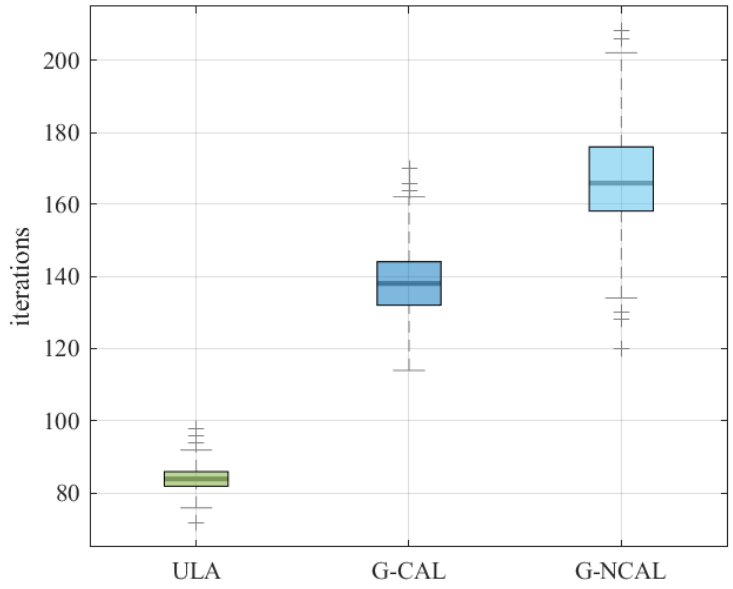

Figure 5.16: Distribution of the StEFCal convergence speed for ULA, G-CAL and G-NCAL. The result is obtained by performing 1000 Monte-Carlo simulations, each with a different $\boldsymbol{\theta}$ generated. The three array designs used 84.6480, 137.9920 and 166.7540 iterations on average to reach their convergence.

As a conclusion, the presented results demonstrate a potential of accelerating the calibration process by considering the calibration during the sensor design (i.e. G-CAL), while not compromising any imaging capability. Such may become useful for the next generation RA telescope array designs, e.g. SKA [12], as the number of sensors will be greatly increased and large-scale joint calibration and imaging can become a great challenge [9].

6 Discussion

From previous chapters, it is found that considering calibration only has a negligible influence on the CRB. This chapter aims to provide a more involved analysis to explain this particular phenomenon.

In order to simplify the analysis, we shift our attention back to scenario 1.2a, where $\boldsymbol{\theta}$ only contains $\boldsymbol{\gamma}, \boldsymbol{\phi}$ and $\boldsymbol{\sigma}_s$. The error in the final image estimate comprises two parts:

1. $\mathbf{C}_{\sigma_s\sigma_s}$ - imaging error due thermal noise, assuming the gain estimates are the true gains.
2. $\mathbf{C}_{gg\rightarrow\sigma_s\sigma_s}$ - gain estimation error due to thermal noise that is propagated to the image.

Both parts are visible in the Fisher information

$$\tilde{\mathbf{F}} = \mathbf{F}_{\sigma_s\sigma_s} - \mathbf{F}_{gg\rightarrow\sigma_s\sigma_s} \tag{6.1}$$

$$= \mathbf{F}_{\sigma_s\sigma_s} - \mathbf{F}_{\sigma_s g}\,\mathbf{F}_{gg}^{-1}\,\mathbf{F}_{g\sigma_s}. \tag{6.2}$$

As stated before, if the true gain is known, then $\mathbf{F}_{gg}$ is effectively all-zero hence the CRB is the direct inversion of $\mathbf{F}_{\sigma_s\sigma_s}$, i.e. $\mathbf{C} = \mathbf{F}_{\sigma_s\sigma_s}^{-1}$. If the gain is treated as nuisance, the uncertainty in the gain estimates manifests itself as a reduction in the Fisher information, effectively being the second term $\mathbf{F}_{gg\rightarrow\sigma_s\sigma_s}$ in (6.1).

An experiment was conducted to examine how each component of the imaging error varies with a changing receiver location $\mathbf{z}$. The tested array is a minimal sparse ruler array with 20 receivers (on position {0,1,2,3,7,14,21,28,43,58,73,88,103,111,119,127,135,136,137,138}), but the third element is re-located and swept through the 1D receiver domain along the x-axis, with a resolution of 0.1 half-wavelength. The array is assumed to estimate a total of 999 sources evenly distributed on the 1D sky.

The result is shown in figure 6.1. We examine three different error components as a function of x_3 (the x-coordinate of the third receiver element):

1. Total imaging error due to thermal noise $f_{\sigma_s} = \mathrm{tr}\left\{\mathbf{F}_{\sigma_s\sigma_s}^{-1}\right\}$ (shown in (a))
2. Total calibration error $f_g = \mathrm{tr}\left\{\mathbf{F}_{gg}^{-1}\right\}$ (shown in (b))
3. Gain estimation error propagated into image $f_{g\rightarrow\sigma_s} = f - f_{\sigma_s}$ (shown in (c)), where

$$f = \mathrm{tr}\left\{\left[\mathbf{F}_{\sigma_s\sigma_s} - \mathbf{F}_{\sigma_s g}^{H}\left(\mathbf{F}_{gg}\right)^{-1}\mathbf{F}_{g\sigma_s}\right]^{-1}\right\}. \tag{6.3}$$

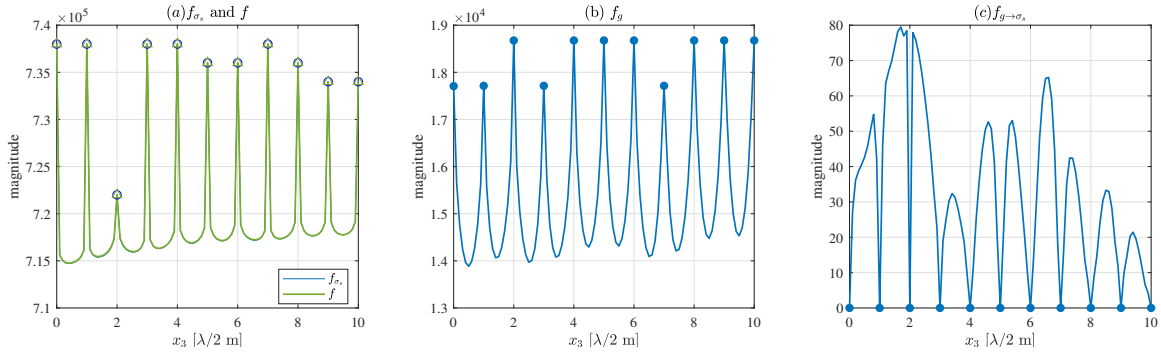

Figure 6.1: Components of imaging error. The half-wavelength locations are highlighted by markers.

As expected, among integer half-wavelength locations, the lowest CRB is achieved when the third receiver is moved to the position $2 \times \frac{\lambda}{2}$ [m], forming an optimal sparse ruler array together with the other 19 antennas.

From (a) it is clear that the difference between f and f_{σ_s} is almost invisible. Although the gain estimation error f_g is at an order of 10^4, it barely gets propagated into the image. As shown in (c), $f_{g\to\sigma_s}$ peaks at merely 80, and even much lower (close to zero) at integer multiples of $\frac{\lambda}{2}$. Compared to the image error due to thermal noise, the propagated gain error is negligible. This suggests that there is no difference between whether to consider gain estimation or not in array designs.

Similar results can be found in [30], in which it was found that for almost all the sources, the image covariance due to calibration errors are 2 orders of magnitude smaller than due to measurement noise. However, the result does not demonstrate if altering the sensor positions makes any difference. So our experiment makes more sense in the context of sensor location optimization.

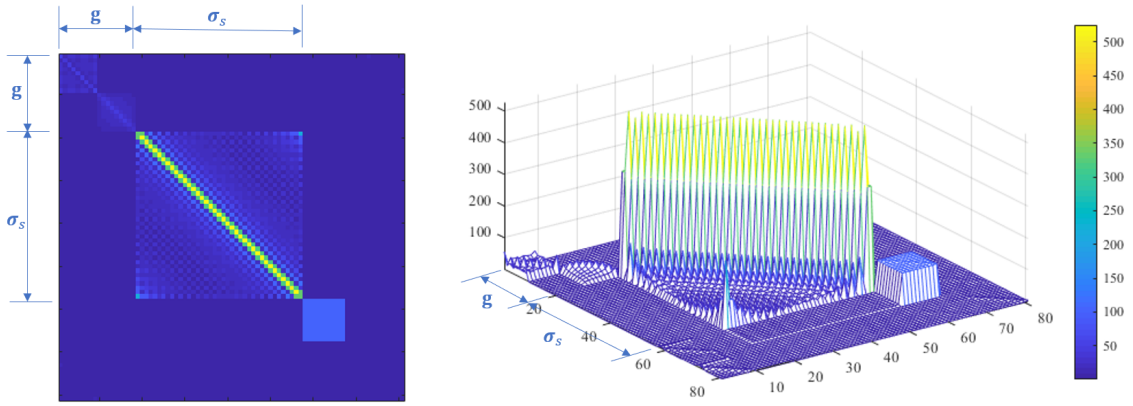

(a) Magnitude of the CRB matrix

(b) Mesh plot of the CRB matrix's magnitude

Figure 6.2: (a) Magnitude plot of an example scenario 3b CRB matrix. (b) The same content of (a) displayed in a mesh plot for the ease of visual interpretation.

Further evidence can be found by inspecting the CRB matrix. Figure 6.2 plots an example CRB matrix under scenario 3b for a 10-element ULA. Observe that the entries of the sub-matrices $\mathbf{C}_{g\sigma_s}$ and $\mathbf{C}_{\sigma_s g}$ have nearly zero magnitudes, which implies that there is almost no cross-correlation between the errors of $\mathbf{g}$ and $\boldsymbol{\sigma}_s$ estimates. The submatrices $\mathbf{C}_{gg}$ and $\mathbf{C}_{\sigma_s\sigma_s}$ form a block diagonal structure in the CRB, and so do $\mathbf{F}_{gg}$ and $\mathbf{F}_{\sigma_s\sigma_s}$ in the FIM. Therefore, by definition, $\mathbf{g}$ and $\boldsymbol{\sigma}_s$ can be more or less considered as orthogonal parameters [31]. To be more explicit, as $\mathbf{F}_{\sigma_s g}$ and $\mathbf{F}_{g\sigma_s}$ have near-zero magnitudes, the second term $\mathbf{F}_{\sigma_s g}\,\mathbf{F}_{gg}^{-1}\,\mathbf{F}_{gs}$ in (6.1) is heavily attenuated. Therefore, the apparent FIM $\tilde{\mathbf{F}}$ is approximately the same to $\mathbf{F}_{\sigma_s\sigma_s}$, which explains the discussed phenomenon.

We suspect that the near-zero magnitudes of $\mathbf{F}_{\sigma_s g}$ and $\mathbf{F}_{g\sigma_s}$ are consequences of the extremely low SNR in the considered RA scenarios. To see this, we express the FIM sub-blocks by the Bangs' formula,

$$\mathbf{F}_{\sigma_s\sigma_s} = \mathbf{J}_{\sigma_s}\,\boldsymbol{\Sigma}^{-1}\,\mathbf{J}_{\sigma_s}, \tag{6.4}$$

$$\mathbf{F}_{\sigma_s g} = \mathbf{J}_{\sigma_s}\,\boldsymbol{\Sigma}^{-1}\,\mathbf{J}_{g}. \tag{6.5}$$

where $\mathbf{J}_g = [\mathbf{J}_\gamma, \mathbf{J}_\phi]$. In (2.6), (2.7) and (2.8), the gain-related Jacobians $\mathbf{J}_\gamma$ and $\mathbf{J}_\phi$ all contain a $\boldsymbol{\Sigma}_s$ factor which is small under low SNR conditions. In contrast, $\mathbf{J}_{\sigma_s}$ is not reduced by any factor at all. Thus, $\mathbf{F}_{gg}$ and $\mathbf{F}_{\sigma_s\sigma_s}$ are heavily attenuated as well.

7 Conclusion and Future Works

7.1 Conclusion

In this thesis, we investigated the optimal sensor placement problem in the context of calibration-involved radio astronomy imaging processes. Three scenarios were considered: (i) pure imaging, (ii) pure calibration, and (iii) imaging with nuisance gains. A CRB analysis was conducted. Starting from the standard Bangs' formula, closed-form CRBs for each scenario are derived, which incorporate sensor selection and nuisance parameters.

Based on the derived CRBs, we discretized the problem and adopted a combinatorial optimization framework. We further employed two approaches to solve such a problem in approximation, which were the greedy algorithm and the convex semi-definite relaxation. A series of sensor selection tests demonstrated that the greedy algorithm suites the research problem better due to its good performance and significantly low computational complexity. As such, it was chosen as the selection algorithm in the simulation.

The simulation was two-fold. First we verified CRBs through the statistical behavior tests of the designed arrays. After that, we performed general behavior tests for the complete imaging scenario (i.e. scenario 3b). We found that considering gain calibration in array design does not provide promising improvements in terms of the resulting estimation MSE. With further investigation, it was found that such a phenomenon can be explained by the estimation error propagation.

The key findings of the thesis work can be listed as follows:

- During the CRB analysis, we have proven that the gain-related FIM $\mathbf{F}_{gg}$ is guaranteed to be full-rank for the considered estimation problems, thus it makes the apparent FIM formulation (2.14) valid. The invertibility of the apparent FIM is however dependent on the rank of $\mathbf{J}_{\sigma_s}$, which is closely related to the DOF of the difference co-array studied in [19].

- The optimal array design for imaging tends to be the minimal sparse ruler if the parameters fit such a ruler. In [27], the utilization of sparse ruler designs was proposed for achieving the maximum compression while preserving the identifiability of the signal covariances. In this thesis, we confirmed such a design for a CRB-based optimality criterion.

- The optimal array configuration for calibration is an array with all elements experiencing coherent phase delays from the calibration sources. Such a result might not be directly useful, but it may become a design reference to provide more insights for other future applications. For example, it suggests that if an array

design would like to accommodate gain calibration, it might need to have a wider spatial extent since the elements have to spread out to take those said locations.

- Regarding scalar gains as nuisance parameters has an insignificant impact on the CRB-based optimal imaging array design. This is mainly caused by the gains to be nearly-orthogonal parameters to the image. One possible reason could be the extreme low SNR that leads to considerably small magnitudes of $\mathbf{J}_\gamma$ and $\mathbf{J}_\phi$.
- The calibration-incorporated design demonstrates the potential to accelerate the gain calibration process. In the experiment, compared to the G-NCAL design, the proposed G-CAL array reduces the required number of StEFCal iterations by roughly 17% on average.

7.2 Future works

The potential improvements and future works are presented as follows:

- **Incorporating more system dynamics**
  The current work only considers one time-frequency bin. In reality, the optimal sensor placement problem must take the full range of operating frequencies into account. The impact of other effects, e.g. earth rotation and ionospheric layer irregularity, also needs to be analyzed. These all bring new challenges into the proposed sensor placement method. And in those scenarios, the gain calibration may have a more pronounced impact on imaging.
- **Data selection for large-scale telescopes**
  - For large-scale telescopes, the data throughput becomes a serious bottleneck of the whole system. For instance, in each LOFAR Netherlands station, only 48 digital receiver units (RCUs) are available at a time, whereas the station can generation 3 times the amount of data (96 LBAs and 48 HBAs) [9]. This illustrates the demand of a reliable data reduction scheme.
  - Sensor *placement* and sensor *selection* are essentially the same under the the combinatorial optimization framework, so the existing materials can be directly used for the additional objective.
  - To switch to the sensor selection problem, we set the receiver domain as the union of existing antenna coordinates. Since the selection can be made on a per time-frequency bin basis, the selection is not required to be fixed, and does not need to take the expectation $\mathbb{E}(\boldsymbol{\theta})$. The selection can be made for the true $\boldsymbol{\theta}$ which can be approximated by the $\boldsymbol{\theta}$ from the previous STI interval assuming appropriate stationarity.
- **Unevenly spaced candidates**
  - In this thesis, the receiver domain is descritized evenly to form a regular grid. However, figure 6.1 (a) clearly shows that when the sensor is positioned between half-wavelength grid points (i.e. x_3 is not an integer multiple of $\frac{\lambda}{2}$),

much lower estimation MSEs can be obtained. This reveals a possibility for utilizing irregular arrays to achieve better imaging performances.

  - One feasible approach is to distribute the candidates in a denser way such that the spaces between half-wavelength grid points are sufficiently sampled. However, this would scale up the computational complexity considerably.
  - Another possible approach would be considering gridless methods, where we optimize the sensor locations $\mathcal{Z}$ directly. A pioneer work has been done by [32].

- **Incorporating source sparsity**
  As the sky is usually filled with point sources and the image $\mathbf{r}$ is sparse, incorporating such an additional constraint may provide a more accurate CRB for the astronomical imaging problem. A detailed study for the CRB with sparse parameters was done in [33].

- **Extension to other fields**
  Although this thesis focuses on radio astronomy applications, as the data model is considerably generic, we believe our work can be extended to various other domains such as radar or acoustic system designs.

Appendix A

A.1 Invertibility of $\mathbf{F}_{gg}$

First, two conditions that are often implicitly assumed in common imaging scenarios to ensure the sky model $\mathbf{R}_0 = \mathbf{A}\boldsymbol{\Sigma}_s\mathbf{A}^H$ is non-singular:

- The number of sources N is greater than the number of receivers M, such that $\mathbf{A}$ is wide.
- There is only one imaging source at single discretized pixel of the sky, i.e. no imaging sources are co-located. This is to ensure that the columns of $\mathbf{A}$ are linearly independent.

Therefore, the data covariance matrix $\mathbf{R} = \mathbf{G}\,\mathbf{R}_0\,\mathbf{G}^H + \boldsymbol{\Sigma}_n$ and the Wishart covariance $\boldsymbol{\Sigma} = \overline{\mathbf{R}} \otimes \mathbf{R}$ are also non-singular.

As derived in Section 2.2, the Jacobians corresponding to gain estimation are given as

$$\mathbf{J}_\gamma = \left[(\overline{\mathbf{G}\mathbf{R}_0}\,\boldsymbol{\Phi}) \circ \mathbf{I} + \mathbf{I} \circ (\mathbf{G}\mathbf{R}_0\,\overline{\boldsymbol{\Phi}})\right]\boldsymbol{\Psi}_s^T \tag{A.1}$$

$$\mathbf{J}_\phi = \mathrm{j}\left[(\overline{\mathbf{G}\mathbf{R}_0}\,\mathbf{G}) \circ \mathbf{I} - \mathbf{I} \circ (\mathbf{G}\mathbf{R}_0\,\overline{\mathbf{G}})\right]\boldsymbol{\Psi}_s^T. \tag{A.2}$$

In the proof, we first ignore the $\boldsymbol{\Psi}_s^T$ matrices and demonstrate that Jacobian $\mathbf{J}_g = [\mathbf{J}_\gamma, \mathbf{J}_\phi]$ becomes rank-deficient.

$$\mathbf{J}_\gamma = \left[(\overline{\mathbf{G}\mathbf{R}_0}\,\boldsymbol{\Phi}) \circ \mathbf{I} + \mathbf{I} \circ (\mathbf{G}\mathbf{R}_0\,\overline{\boldsymbol{\Phi}})\right] \tag{A.3}$$

$$\mathbf{J}_\phi = \mathrm{j}\left[(\overline{\mathbf{G}\mathbf{R}_0}\,\mathbf{G}) \circ \mathbf{I} - \mathbf{I} \circ (\mathbf{G}\mathbf{R}_0\,\overline{\mathbf{G}})\right]. \tag{A.4}$$

This motivates us to apply the selection matrix $\boldsymbol{\Psi}_s^T$ to fix a phase reference. After that, $\mathbf{J}_g$ becomes full rank. The proof is structured as follows:

(A.1.1) Providing some preliminary works.

(A.1.2) Demonstrating that $\mathbf{J}_\gamma$ has a full column-rank.

(A.1.3) Proving that $\mathbf{J}_g$ is rank-deficient, but can become full rank by excluding any single column of $\mathbf{J}_\phi$, and consequently $\mathbf{F}_{gg}$ can become invertible. The proof is done by applying some elementary matrix operations on $\mathbf{J}_g$ and observe the structure of the transformed matrix $\mathbf{T}$.

A.1.1 Proof of $\mathbf{E}_\gamma$, $\mathbf{E}_\phi$, $\mathbf{D}_\gamma$ and $\mathbf{D}_\phi$ to be full-rank

To make the derivation concise, we denote the Jacobians in the Khatri-rao sum structure

$$\mathbf{J}_\gamma = \mathbf{D}_\gamma + \overline{\mathbf{D}_\gamma} = \mathbf{E}_\gamma \circ \mathbf{I} + \mathbf{I} \circ \overline{\mathbf{E}_\gamma} \tag{A.5}$$

$$\mathbf{J}_\phi = \mathbf{D}_\phi + \overline{\mathbf{D}_\phi} = \mathrm{j}\left(\mathbf{E}_\phi \circ \mathbf{I} - \mathbf{I} \circ \overline{\mathbf{E}_\phi}\right). \tag{A.6}$$

Since $\mathbf{R}_0$ is full rank, $\mathbf{E}_\gamma$ and $\mathbf{E}_\phi$ are also full rank because they are essentially $\mathbf{R}_0$ being multiplied by full rank diagonal matrices $\mathbf{G}$ and $\mathbf{\Phi}$.

We further notice that $\mathbf{D}_\gamma$, $\overline{\mathbf{D}_\gamma}$, $\mathbf{D}_\phi$ and $\overline{\mathbf{D}_\phi}$ can be proven to have full column ranks since they are Khatri-rao products with identity matrices:

- **Post-Khatri-rao by an identity matrix** (i.e. $\mathbf{A} \circ \mathbf{I}$) creates a stacked diagonal structure as shown in figure A.1a. The i-th single diagonal sub-matrix are $\mathrm{diag}(\mathbf{A}_{i,:})$ where $\mathbf{A}_{i,:}$ is the i-th row of the matrix $\mathbf{A}$.
- **Pre-Khatri-rao by an identity matrix** (i.e. $\mathbf{I} \circ \mathbf{B}$) creates a block diagonal structure, whose block matrices on the diagonal are the columns of $\mathbf{B}$ as shown in figure A.1b.

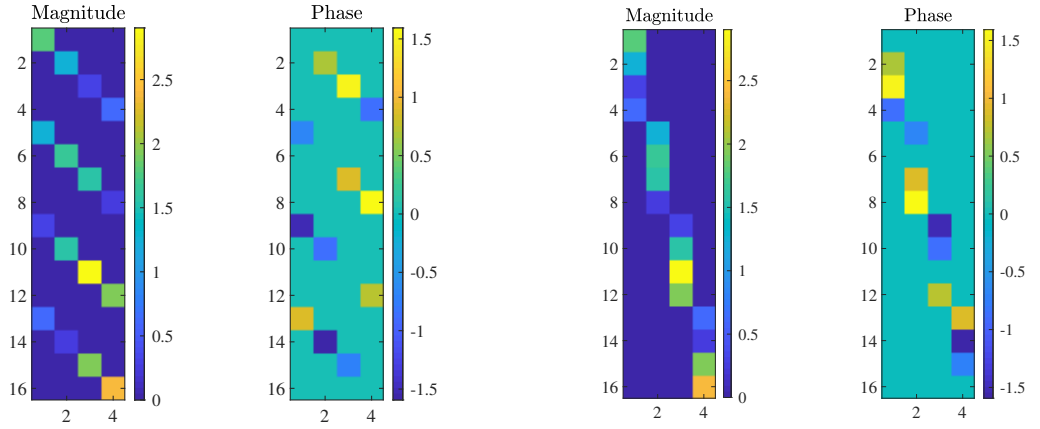

(a) An example of the structure of $\mathbf{A} \circ \mathbf{I}$

(b) An example of the structure of $\mathbf{I} \circ \mathbf{B}$

Figure A.1: Matrix structures of the Khatri-Rao product with identity matrices

As $\mathbf{E}_\gamma$ and $\mathbf{E}_\phi$ are both full rank, the Katri-rao products cannot contain all-zero columns. Considering the block-diagonal structures, $\mathbf{D}_\gamma$, $\overline{\mathbf{D}_\gamma}$, $\mathbf{D}_\phi$ and $\overline{\mathbf{D}_\phi}$ must be full-rank.

A.1.2 Proof of $\mathbf{J}_\gamma$ to be full-rank

As shown in figure A.2a, for the i-th column of $\mathbf{J}_\gamma$ (size M^2-by-M), the $[(i-1)M+i]$-th element (shown in yellow in the magnitude plot) is the only non-zero element of the row where it is located. As a side note, theses entries corresponds to the diagonal entries

of the covariance $\mathbf{R}$. Hence, the columns of $\mathbf{J}_\gamma$ are linearly independent, which ensure it to have a full column-rank.

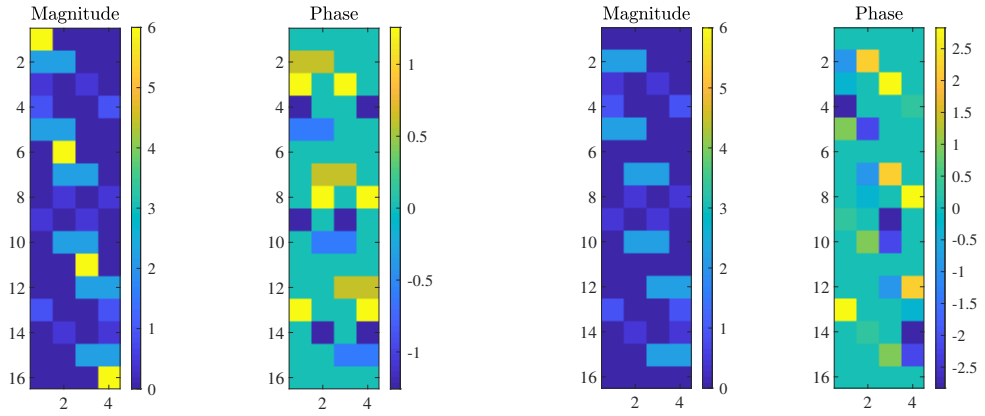

(a) An example of $\mathbf{J}_\gamma$ (b) An example of $\mathbf{J}_\phi$

Figure A.2: Examples of the $\mathbf{J}_\gamma$ and $\mathbf{J}_\phi$ matrices

However, this is not true for $\mathbf{J}_\phi$ since the minus sign in (A.6) cancels the non-zero values, leaving zeros on these entries (see figure A.2b). This also explains why phase estimation of gain is usually harder to achieve compared to magnitude estimation - we cannot infer phase information from the diagonal entries of $\mathbf{R}$ as self-correlation $\mathbb{E}[x_i\overline{x_i}]$, $i = 1, ...M$, cancels out the phase.

A.1.3 Proof of $\mathbf{J}_g = [\mathbf{J}_\gamma, \mathbf{J}_\phi]$ to be full-rank (with the condition of fixing a phase reference)

First we do some elementary matrix operations to simplify the structure of $\mathbf{J}_g$. Note that

$$\mathbf{E}_\phi = \mathbf{E}_\gamma \mathbf{\Gamma} \tag{A.7}$$

where $\mathbf{\Gamma} = \text{diag}(\boldsymbol{\gamma})$. Hence,

$$\mathbf{D}_\phi = \mathbf{D}_\gamma(\text{j}\mathbf{\Gamma}) \tag{A.8}$$

So we scale $\mathbf{J}_\gamma$'s columns by applying $\mathbf{\Gamma}$ and scale $\mathbf{J}_\phi$ by $-\mathrm{j}$, which gives

$$\begin{aligned}
\Big[\mathbf{J}_\gamma\mathbf{\Gamma}, \quad \mathbf{J}_\phi(-\mathrm{j})\Big] &= \Big[\Big(\overline{\mathbf{G}\mathbf{R}_0}\,\mathbf{\Phi}\Big) \circ \mathbf{I} + \mathbf{I} \circ \big(\mathbf{G}\mathbf{R}_0\,\overline{\mathbf{\Phi}}\Big)\mathbf{\Gamma}, \\
&\qquad\qquad \mathrm{j}\Big[\big(\overline{\mathbf{G}\mathbf{R}_0}\,\mathbf{G}\big) \circ \mathbf{I} - \mathbf{I} \circ \big(\mathbf{G}\mathbf{R}_0\,\overline{\mathbf{G}}\big)\Big](-\mathrm{j})\Big] && \text{(A.9)} \\
&= \Big[\big(\overline{\mathbf{G}\mathbf{R}_0}\,\mathbf{\Phi}\mathbf{\Gamma}\big) \circ \mathbf{I} + \mathbf{I} \circ \big(\mathbf{G}\mathbf{R}_0\,\overline{\mathbf{\Phi}\mathbf{\Gamma}}\big), \\
&\qquad\qquad \big(\overline{\mathbf{G}\mathbf{R}_0}\,\mathbf{G}\big) \circ \mathbf{I} - \mathbf{I} \circ \big(\mathbf{G}\mathbf{R}_0\,\overline{\mathbf{G}}\big)\Big] && \text{(A.10)} \\
&= \Big[\big(\overline{\mathbf{G}\mathbf{R}_0}\,\mathbf{G}\big) \circ \mathbf{I} + \mathbf{I} \circ \big(\mathbf{G}\mathbf{R}_0\,\overline{\mathbf{G}}\big), \\
&\qquad\qquad \big(\overline{\mathbf{G}\mathbf{R}_0}\,\mathbf{G}\big) \circ \mathbf{I} - \mathbf{I} \circ \big(\mathbf{G}\mathbf{R}_0\,\overline{\mathbf{G}}\big)\Big] && \text{(A.11)} \\
&= \Big[\tilde{\mathbf{E}} \circ \mathbf{I} + \mathbf{I} \circ \overline{\tilde{\mathbf{E}}}, \quad \tilde{\mathbf{E}} \circ \mathbf{I} - \mathbf{I} \circ \overline{\tilde{\mathbf{E}}}\Big] && \text{(A.12)} \\
&= \Big[\mathbf{J}_1, \quad \mathbf{J}_2\Big] && \text{(A.13)}
\end{aligned}$$

Apply elementary operations $\frac{1}{2}(\mathbf{J}_1 + \mathbf{J}_2)$ and $\frac{1}{2}(\mathbf{J}_1 - \mathbf{J}_2)$ gives the transformed matrix

$$\begin{aligned}
\mathbf{T} &= \Big[\tilde{\mathbf{E}} \circ \mathbf{I}, \quad \mathbf{I} \circ \overline{\tilde{\mathbf{E}}}\Big] && \text{(A.14)} \\
&= \Big[\mathbf{T}_1, \quad \mathbf{T}_2\Big] && \text{(A.15)}
\end{aligned}$$

which has the structure as illustrated in figure A.3. The left half, $\mathbf{T}_1$, is post-Katri-rao multiplied by identity, whereas the right half, $\mathbf{T}_2$, is pre-Katri-rao multiplied by identity.

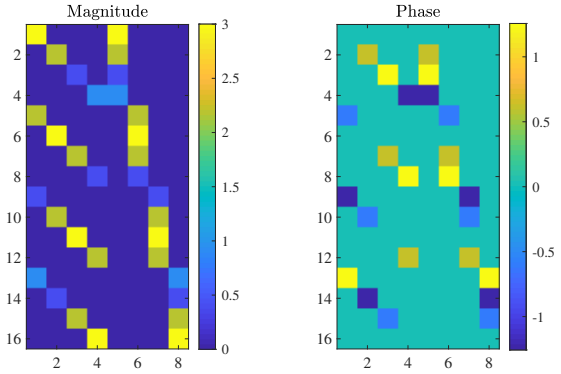

Figure A.3: An example structure of the transformed matrix $\mathbf{T}$.

Since $\tilde{\mathbf{E}}$ is Hermitian, the rows of $\tilde{\mathbf{E}}$ are the transpose of the columns of $\overline{\tilde{\mathbf{E}}}$, which enables us to relate $\mathbf{T}_1$ and $\mathbf{T}_2$,

$$\mathbf{T}_1 = \begin{bmatrix} \operatorname{diag}([\tilde{\mathbf{E}}]_{:,1}) \\ \vdots \\ \operatorname{diag}([\tilde{\mathbf{E}}]_{:,M}) \end{bmatrix} = \begin{bmatrix} \operatorname{diag}(\overline{[\tilde{\mathbf{E}}]_{1,:}}) \\ \vdots \\ \operatorname{diag}(\overline{[\tilde{\mathbf{E}}]_{M,:}}) \end{bmatrix} \tag{A.16}$$

$$\mathbf{T}_2 = \begin{bmatrix} \operatorname{diag}(\overline{[\tilde{\mathbf{E}}]_{1,:}}) & \mathbf{O} & \cdots & \mathbf{O} \\ \mathbf{O} & \operatorname{diag}(\overline{[\tilde{\mathbf{E}}]_{2,:}}) & \cdots & \mathbf{O} \\ \vdots & \vdots & \ddots & \vdots \\ \mathbf{O} & \mathbf{O} & \cdots & \operatorname{diag}(\overline{[\tilde{\mathbf{E}}]_{M,:}}) \end{bmatrix} \tag{A.17}$$

where $[\tilde{\mathbf{E}}]_{i,:}$ and $[\tilde{\mathbf{E}}]_{:,j}$ the i-th row and j-th column of $\tilde{\mathbf{E}}$ respectively.

It is apparent that $\mathbf{T}$ is rank-deficient. The i-th column of $\mathbf{T}_2$ is equal to the linear combination of the rest of $\mathbf{T}$'s columns through

$$[\mathbf{T}_2]_{:,i} = \mathbf{T} \begin{bmatrix} \mathbf{1}_M \\ \mathbf{e}_i - \mathbf{1}_M \end{bmatrix} \tag{A.18}$$

where $[\mathbf{T}_2]_{:,i}$ is the i-th column of $\mathbf{T}_2$, and $\mathbf{e}_i$ is the unit basis vector which is all-zero but with only the i-th entry being 1.

However, if any single column of $\mathbf{T}_2$ is removed (which corresponds to fixing one of the gain's phase as a reference), $\mathbf{T}$ immediately becomes full-rank. For example, if we remove the first column of $\mathbf{T}_2$, then no matter what linear combination we apply, the non-zero components in the first M columns can never be cancelled completely. This argument still holds when we further exclude one of $\mathbf{T}_1$'s column (which corresponds to resolving the magnitude ambiguity), as $\mathbf{T}$ already has a full column-rank and removing one of the column does not harm the full-rankness.

Since $\mathbf{J}_g$ can be obtained through applying elementary matrix operations on $\mathbf{T}$, it also has a full column-rank. Furthermore, notice that $\mathbf{J}_g$ cannot be a wide matrix. This is owing to the fact that as our model involves least two receivers. When no ambiguity is resolved, $\mathbf{J}_g$ has a size of M^2-by-$2M$ ($M^2 \geq 2M$ for $M \geq 2$). If any ambiguity is resolved, $\mathbf{J}_g$ becomes an even taller matrix. Therefore, combined with the assumption that $\mathbf{\Sigma}$ is non-singular, we can immediately see that

$$\mathbf{F}_{gg} = P\mathbf{J}_{gg}^H \mathbf{\Sigma}^{-1} \mathbf{J}_{gg} \tag{A.19}$$

is non-singular as well, and thereby completes the proof.

A.2 Full selection results

This section includes the complete array selection results for all the scenarios introduced in Chapter 4. As the ULA does not change between scenarios (it just selects the candidates one-by-one sequentially), we report it at the beginning of the section for once and omit it in the rest of the results:

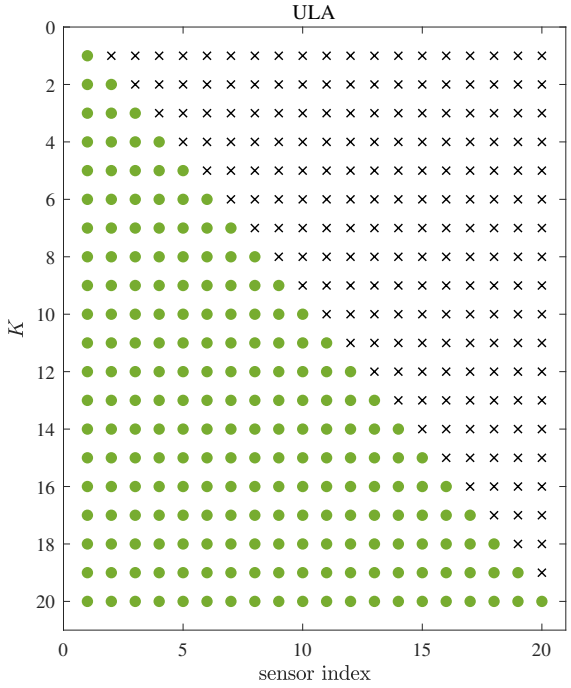

Figure A.4: ULA selection results, which is identical for all the scenarios, and hence only shown for once.

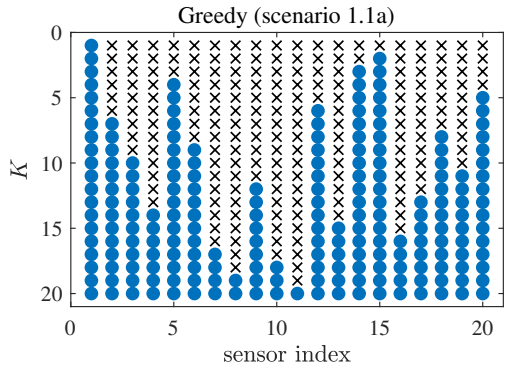
Greedy (scenario 1.1a)
K
sensor index

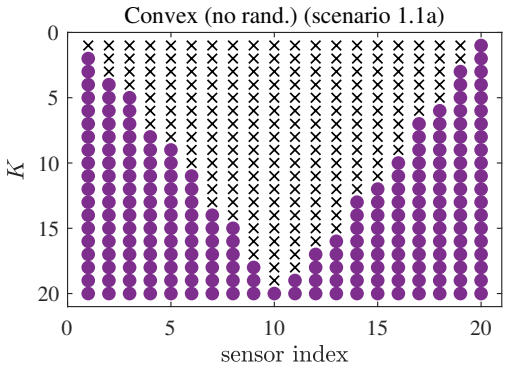
Convex (no rand.) (scenario 1.1a)
K
sensor index

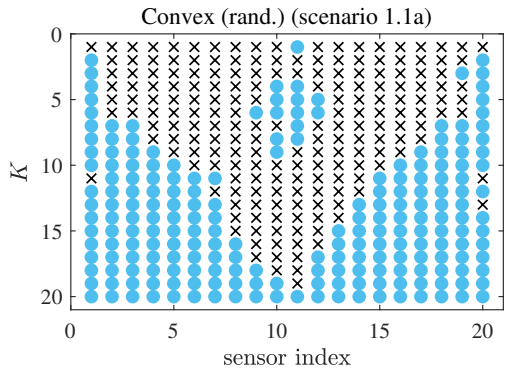
Convex (rand.) (scenario 1.1a)
K
sensor index

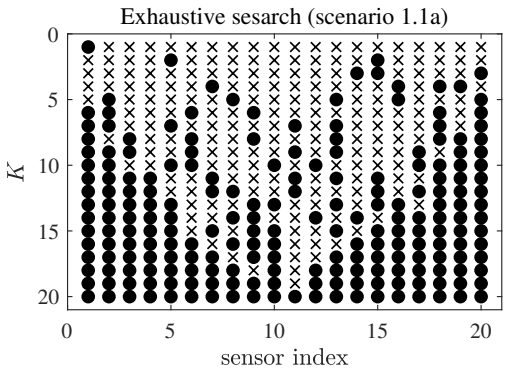
Exhaustive sesarch (scenario 1.1a)
K
sensor index

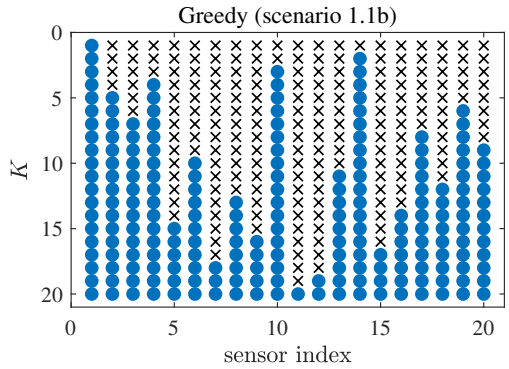
Greedy (scenario 1.1b)
K
sensor index

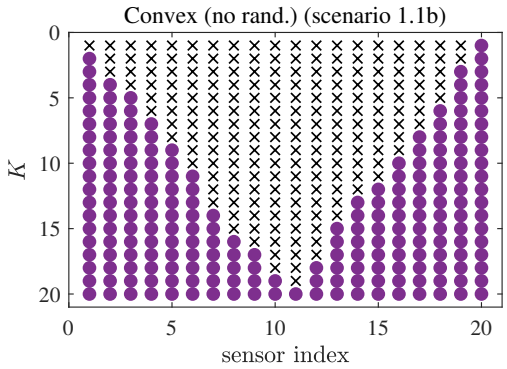
Convex (no rand.) (scenario 1.1b)
K
sensor index

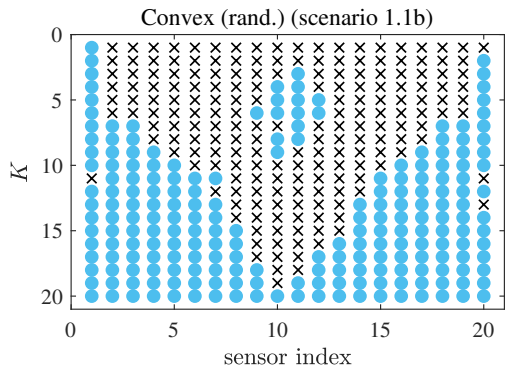
Convex (rand.) (scenario 1.1b)
K
sensor index

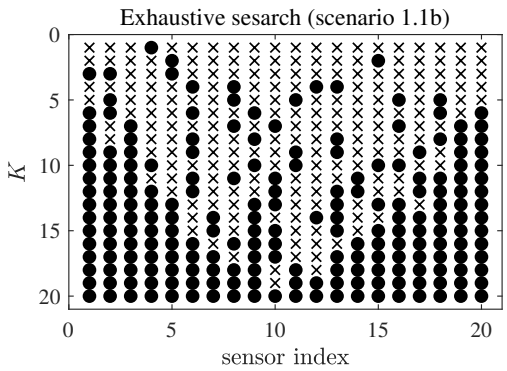
Exhaustive sesarch (scenario 1.1b)
K
sensor index

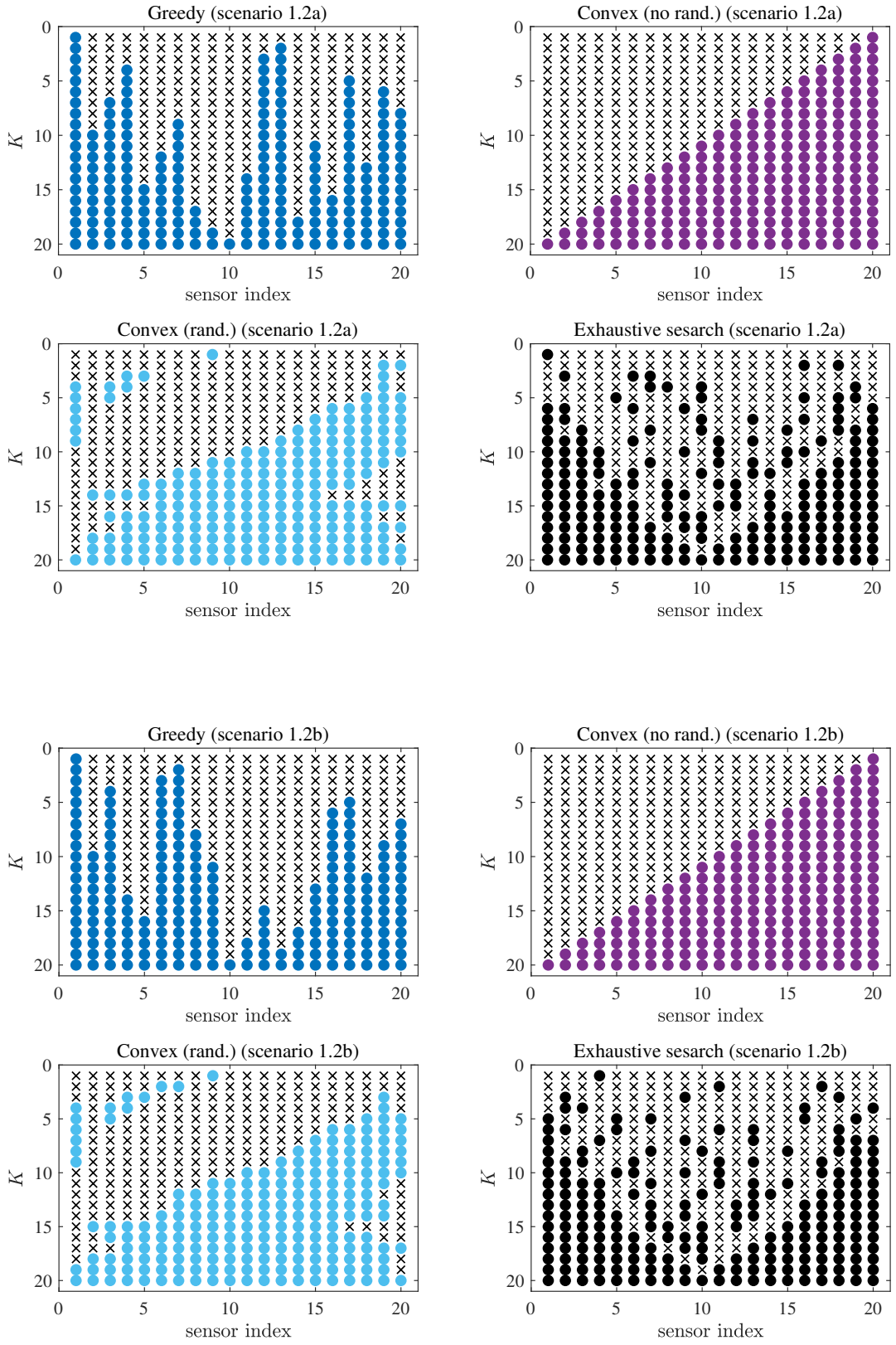
Greedy (scenario 1.2a)
Convex (no rand.) (scenario 1.2a)
Convex (rand.) (scenario 1.2a)
Exhaustive sesarch (scenario 1.2a)
Greedy (scenario 1.2b)
Convex (no rand.) (scenario 1.2b)
Convex (rand.) (scenario 1.2b)
Exhaustive sesarch (scenario 1.2b)
K
sensor index
0
5
10
15
20

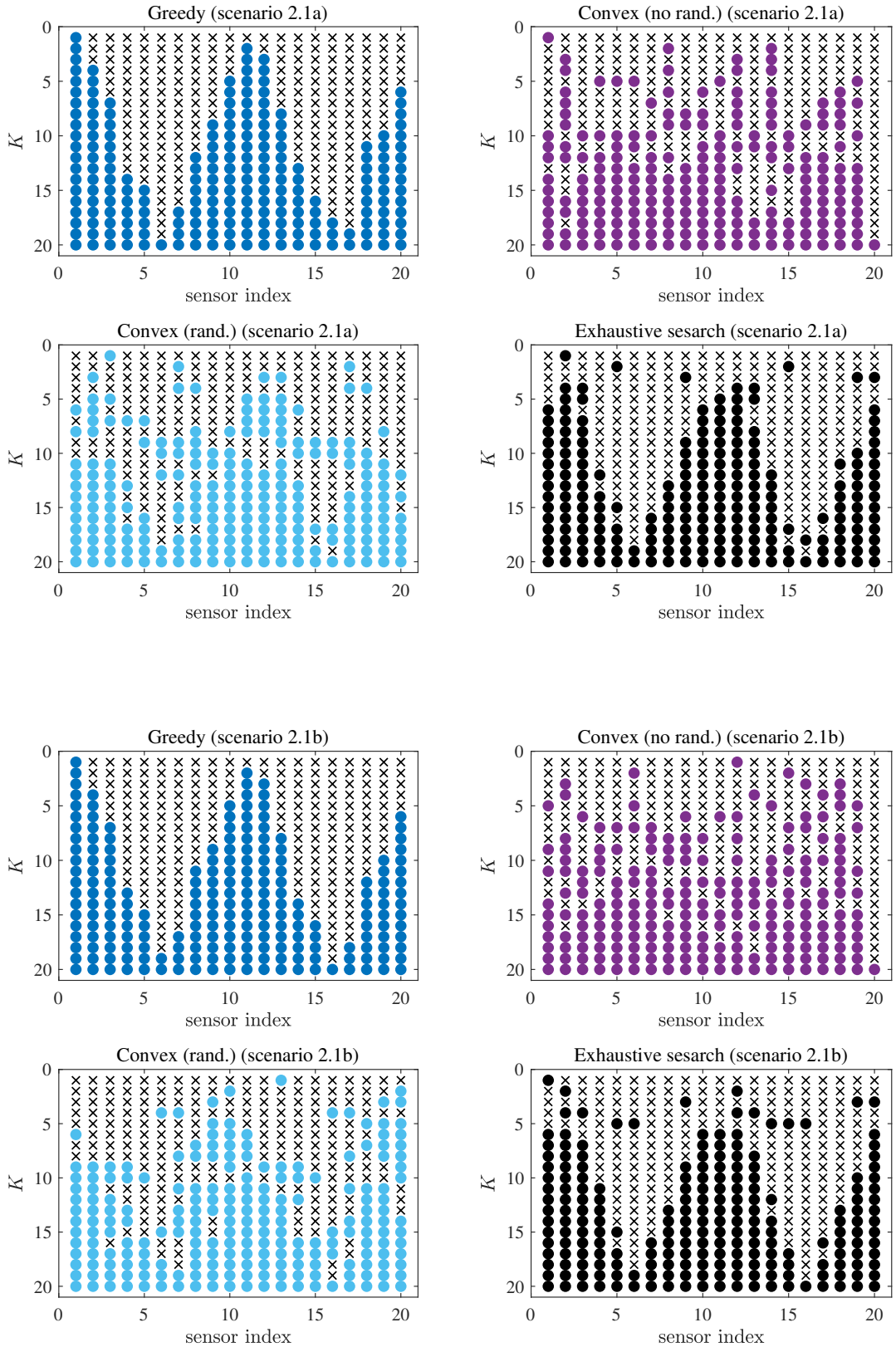
Greedy (scenario 2.1a)
Convex (no rand.) (scenario 2.1a)
Convex (rand.) (scenario 2.1a)
Exhaustive sesarch (scenario 2.1a)
Greedy (scenario 2.1b)
Convex (no rand.) (scenario 2.1b)
Convex (rand.) (scenario 2.1b)
Exhaustive sesarch (scenario 2.1b)
K
sensor index
0
5
10
15
20

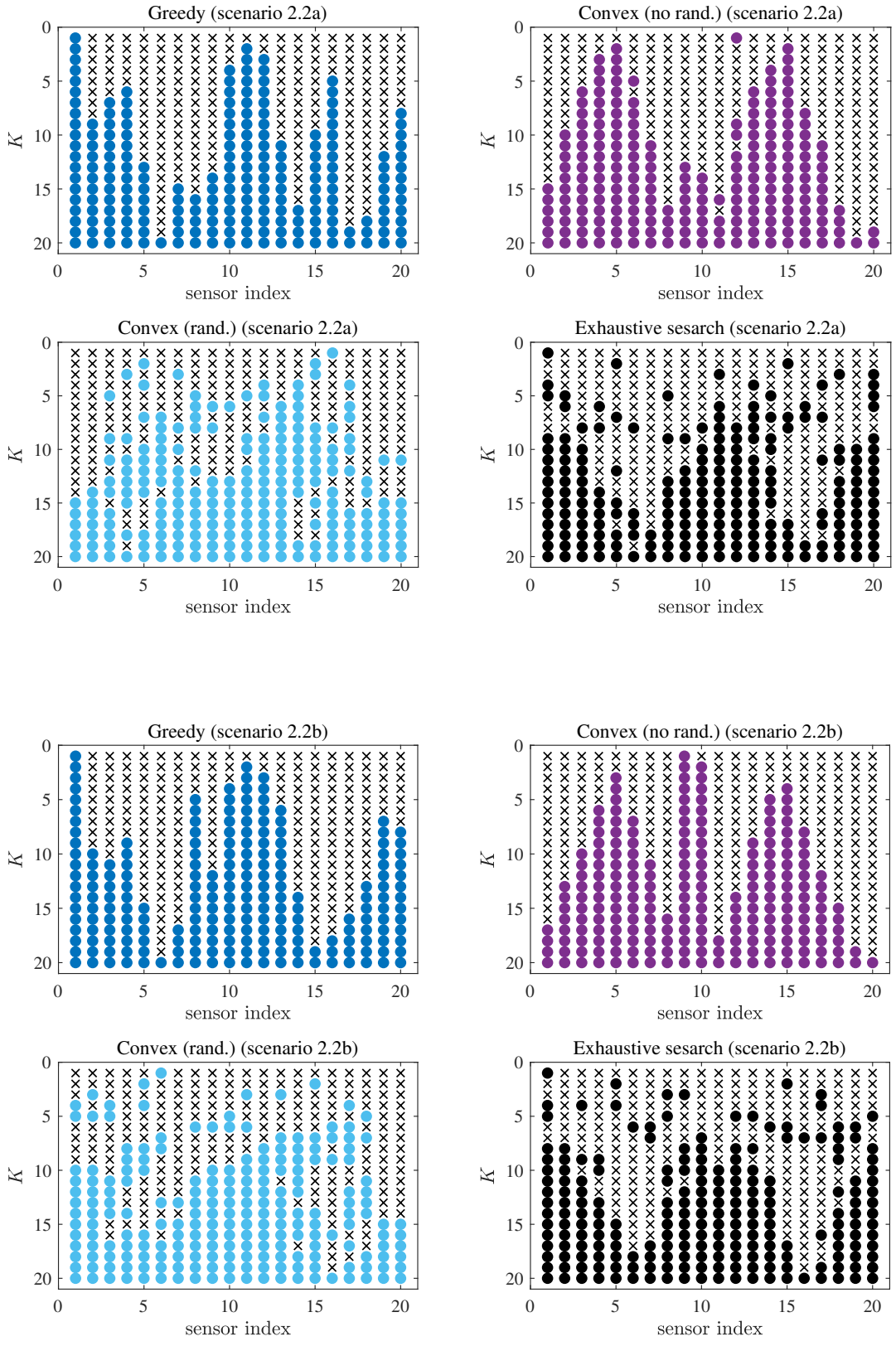
Greedy (scenario 2.2a)
Convex (no rand.) (scenario 2.2a)
Convex (rand.) (scenario 2.2a)
Exhaustive sesarch (scenario 2.2a)
Greedy (scenario 2.2b)
Convex (no rand.) (scenario 2.2b)
Convex (rand.) (scenario 2.2b)
Exhaustive sesarch (scenario 2.2b)
K
sensor index
0
5
10
15
20

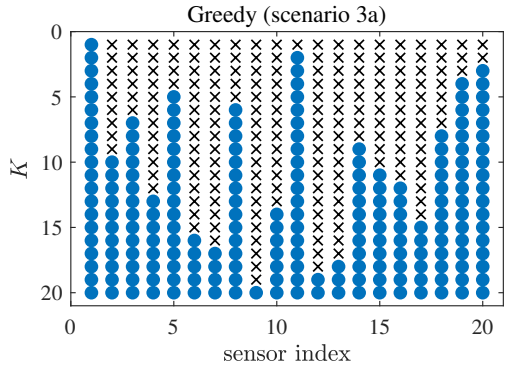
Greedy (scenario 3a)
K
sensor index

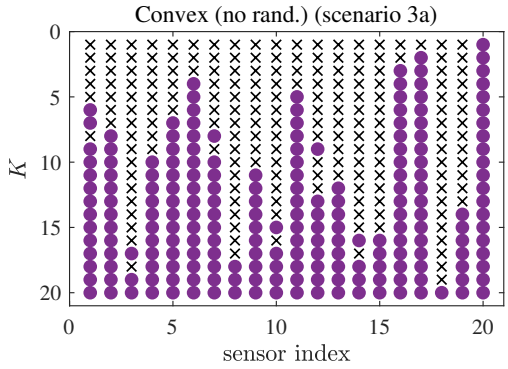
Convex (no rand.) (scenario 3a)
K
sensor index

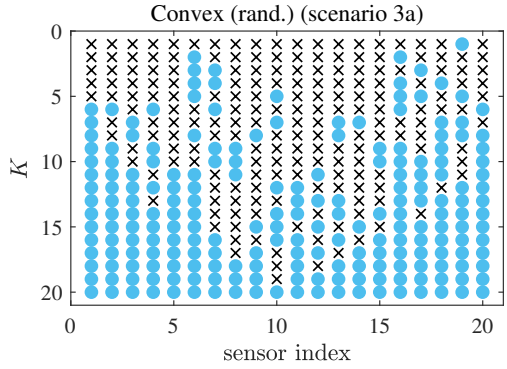
Convex (rand.) (scenario 3a)
K
sensor index

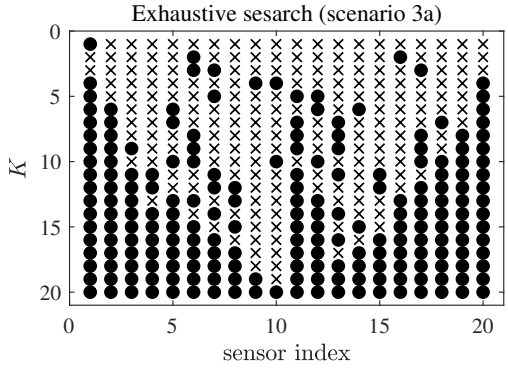
Exhaustive sesarch (scenario 3a)
K
sensor index

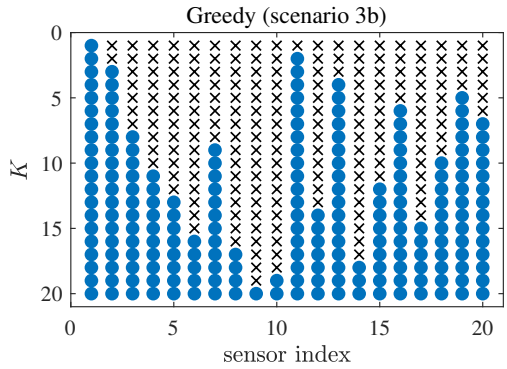
Greedy (scenario 3b)
K
sensor index

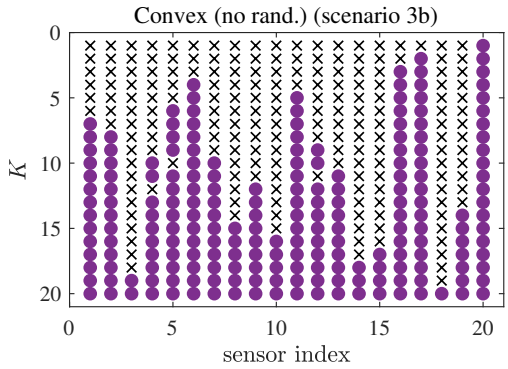
Convex (no rand.) (scenario 3b)
K
sensor index

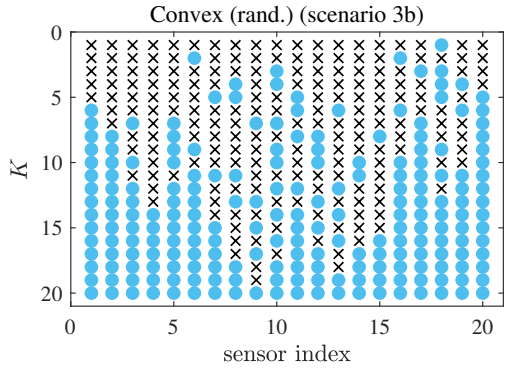
Convex (rand.) (scenario 3b)
K
sensor index

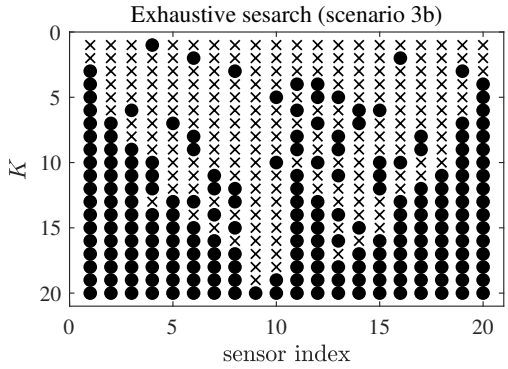
Exhaustive sesarch (scenario 3b)
K
sensor index

Bibliography

[1] A.-J. van der Veen, S. J. Wijnholds, and A. M. Sardarabadi, "Signal processing for radio astronomy," in *Handbook of Signal Processing Systems*. Cham: Springer International Publishing, 2019, pp. 311–360.

[2] S. J. Wijnholds, S. van der Tol, R. Nijboer, and A.-J. van der Veen, "Calibration challenges for future radio telescopes," *IEEE Signal Processing Magazine*, vol. 27, no. 1, pp. 30–42, Jan. 2010.

[3] K. G. Jansky, "Electrical disturbances apparently of extraterrestrial origin," *Proceedings of the Institute of Radio Engineers*, vol. 21, no. 10, pp. 1387–1398, 1933.

[4] R. Levanda and A. Leshem, "Synthetic aperture radio telescopes," *IEEE Signal Processing Magazine*, vol. 27, no. 1, pp. 14–29, Jan. 2010.

[5] G. Virone, A. M. Lingua *et al.*, "Antenna pattern verification system based on a micro unmanned aerial vehicle (uav)," *IEEE Antennas and Wireless Propagation Letters*, vol. 13, pp. 169–172, 2014.

[6] G. Pupillo, G. Naldi *et al.*, "Medicina array demonstrator: calibration and radiation pattern characterization using a uav-mounted radio-frequency source," *Experimental Astronomy*, vol. 39, no. 2, pp. 405–421, Jun. 2015.

[7] C. Raucy, E. de Lera Acedo, N. Razavi-Ghods, D. González-Ovejero, and C. Craeye, "Low-cost near field pattern measurement technique for aperture array characterization," in *2013 7th European Conference on Antennas and Propagation (EuCAP)*, 2013, pp. 661–665.

[8] S. J. Wijnholds, "Fish-eye observing with phased array radio telescopes," Ph.D. dissertation, 2010.

[9] M. P. van Haarlem, M. W. Wise *et al.*, "Lofar: The low-frequency array," *Astronomy & Astrophysics*, vol. 556, p. A2, Aug. 2013.

[10] "Lofar." [Online]. Available: http://www.lofar.org/

[11] "Long wavelength array." [Online]. Available: http://lwa.unm.edu/

[12] "Square kilometre array." [Online]. Available: https://www.skatelescope.org/

[13] J. Högbom, "Aperture synthesis with a non-regular distribution of interferometer baselines," *Astronomy and Astrophysics Supplement*, vol. 15, p. 417, 1974.

[14] S. J. Wijnholds and A.-J. van der Veen, "Data driven model based least squares image reconstruction for radio astronomy," in *2011 IEEE International Conference on Acoustics, Speech and Signal Processing (ICASSP)*. IEEE, May 2011, pp. 2704–2707.

[15] S. M. Kay, *Fundamentals of statistical signal processing. Volume 1, Estimation theory*, ser. Prentice-Hall signal processing series, 1993.

[16] P. Stoica, B. Ottersten, M. Viberg, and R. Moses, "Maximum likelihood array processing for stochastic coherent sources," *IEEE Transactions on Signal Processing*, vol. 44, no. 1, pp. 96–105, 1996.

[17] S. J. Wijnholds and A.-J. van der Veen, "Multisource self-calibration for sensor arrays," *IEEE Transactions on Signal Processing*, vol. 57, no. 9, pp. 3512–3522, Sep. 2009.

[18] T.-T. Lu and S.-H. Shiou, "Inverses of 2×2 block matrices," *Computers & Mathematics with Applications*, vol. 43, no. 1-2, pp. 119–129, Jan. 2002.

[19] P. Pal and P. P. Vaidyanathan, "Nested arrays: A novel approach to array processing with enhanced degrees of freedom," *IEEE Transactions on Signal Processing*, vol. 58, no. 8, pp. 4167–4181, Aug. 2010.

[20] S. P. Chepuri and G. Leus, "Sparsity-promoting sensor selection for non-linear measurement models," *IEEE Transactions on Signal Processing*, vol. 63, no. 3, pp. 684–698, Feb. 2015.

[21] S. Liu, S. P. Chepuri, M. Fardad, E. Masazade, G. Leus, and P. K. Varshney, "Sensor selection for estimation with correlated measurement noise," *IEEE Transactions on Signal Processing*, vol. 64, no. 13, pp. 3509–3522, Jul. 2016.

[22] S. Joshi and S. Boyd, "Sensor selection via convex optimization," *IEEE Transactions on Signal Processing*, vol. 57, no. 2, pp. 451–462, 2009.

[23] S. Boyd and L. Vandenberghe, *Convex Optimization*. Cambridge University Press, Mar. 2004.

[24] S. P. Chepuri and G. Leus, "Graph sampling for covariance estimation," *IEEE Transactions on Signal and Information Processing over Networks*, vol. 3, no. 3, pp. 451–466, Sep. 2017.

[25] G. L. Nemhauser, L. A. Wolsey, and M. L. Fisher, "An analysis of approximations for maximizing submodular set functions—i," *Mathematical Programming*, vol. 14, no. 1, pp. 265–294, Dec. 1978.

[26] Z.-q. Luo, W.-k. Ma, A. So, Y. Ye, and S. Zhang, "Semidefinite relaxation of quadratic optimization problems," *IEEE Signal Processing Magazine*, vol. 27, no. 3, pp. 20–34, May 2010.

[27] D. Romero, D. D. Ariananda, Z. Tian, and G. Leus, "Compressive covariance sensing: Structure-based compressive sensing beyond sparsity," *IEEE Signal Processing Magazine*, vol. 33, no. 1, pp. 78–93, Jan. 2016.

[28] B. Ottersten, P. Stoica, and R. Roy, "Covariance matching estimation techniques for array signal processing applications," *Digital Signal Processing*, vol. 8, no. 3, pp. 185–210, Jul. 1998.

[29] S. Salvini and S. J. Wijnholds, "Fast gain calibration in radio astronomy using alternating direction implicit methods: Analysis and applications," *Astronomy & Astrophysics*, vol. 571, p. A97, Nov. 2014.

[30] S. J. Wijnholds and A.-J. van der Veen, "Fundamental imaging limits of radio telescope arrays," *IEEE Journal of Selected Topics in Signal Processing*, vol. 2, no. 5, pp. 613–623, Oct. 2008.

[31] D. R. Cox and N. Reid, "Parameter orthogonality and approximate conditional inference," *Journal of the Royal Statistical Society. Series B (Methodological)*, vol. 49, no. 1, pp. 1–39, 1987.

[32] S. P. Chepuri and G. Leus, "Continuous sensor placement," *IEEE Signal Processing Letters*, vol. 22, no. 5, pp. 544–548, May 2015.

[33] Z. Ben-Haim and Y. C. Eldar, "The cramér-rao bound for estimating a sparse parameter vector," *IEEE Transactions on Signal Processing*, vol. 58, no. 6, pp. 3384–3389, Jun. 2010.